C00-1198-1247

A LOW TEMPERATURE ULTRASONIC STUDY OF HYDROGEN IN NIOBIUM

BY

DAVID BRIAN POKER

B.S., University of Illinois, 1973
M.S., University of Illinois, 1974

THESIS

Submitted in partial fulfillment of the requirements
for the degree of Doctor of Philosophy in Physics
in the Graduate College of the
University of Illinois at Urbana-Champaign, 1979

Urbana, Illinois

DISTRIBUTION OF THIS DOCUMENT IS UNLIMITED

MASTER

DISCLAIMER

This report was prepared as an account of work sponsored by an agency of the United States Government. Neither the United States Government nor any agency Thereof, nor any of their employees, makes any warranty, express or implied, or assumes any legal liability or responsibility for the accuracy, completeness, or usefulness of any information, apparatus, product, or process disclosed, or represents that its use would not infringe privately owned rights. Reference herein to any specific commercial product, process, or service by trade name, trademark, manufacturer, or otherwise does not necessarily constitute or imply its endorsement, recommendation, or favoring by the United States Government or any agency thereof. The views and opinions of authors expressed herein do not necessarily state or reflect those of the United States Government or any agency thereof.

DISCLAIMER

Portions of this document may be illegible in electronic image products. Images are produced from the best available original document.

A LOW TEMPERATURE ULTRASONIC STUDY OF HYDROGEN IN NIOBIUM

BY

DAVID BRIAN POKER

B.S., University of Illinois, 1973
M.S., University of Illinois, 1974

NOTICE

This report was prepared as an account of work sponsored by the United States Government. Neither the United States nor the United States Department of Energy, nor any of their employees, nor any of their contractors, subcontractors, or their employees, makes any warranty, express or implied, or assumes any legal liability or responsibility for the accuracy, completeness or usefulness of any information, apparatus, product or process disclosed, or represents that its use would not infringe privately owned rights.

THESIS

Submitted in partial fulfillment of the requirements
for the degree of Doctor of Philosophy in Physics
in the Graduate College of the
University of Illinois at Urbana-Champaign, 1979

Urbana, Illinois

DISTRIBUTION OF THIS DOCUMENT IS UNLIMITED

A LOW TEMPERATURE ULTRASONIC STUDY OF HYDROGEN IN NIOBIUM

David Brian Poker, Ph.D.
Department of Physics
University of Illinois at Urbana-Champaign, 1979

Measurements were made of the velocity and attenuation of ultrasonic waves in niobium containing 1000 ppm oxygen with additional concentrations of hydrogen, to determine the properties of a relaxation of the hydrogen which appears below 10 K. Measurements were made as a function of temperature, frequency, polarization of the ultrasonic wave, hydrogen isotope, and concentration of hydrogen and oxygen.

The Birnbaum-Flynn model of hydrogen tunnelling is modified to take into account the trapping of hydrogen by interstitial impurities. An Orbach process is proposed for a relaxation between the degenerate first excited states. Three parameters which are determined by the hydrogen ultrasonic attenuation data are sufficient to describe the properties of this model.

The model correctly predicts the presence of unusual features of the relaxation which are not contained in a classical model of hydrogen motion over a potential barrier; the decrease of the hydrogen relaxation strength at low temperatures, the decrease in velocity below the relaxation temperature without a corresponding effect in the attenuation, and the broadness of the deuterium decrement peak compared to that for hydrogen.

A reasonable fit to the velocity data for low concentration of hydrogen is made by the model with no adjustable parameters. A fit to the heat capacity can be made with the addition of parameters representing the strain effects of the oxygen trapping.

ACKNOWLEDGMENTS

The author would like to thank his advisor, Professor A. V. Granato, for his patience, guidance and encouragement throughout the course of this investigation and during the preparation of this thesis.

He thanks Professor H. K. Birnbaum for assistance in the preparation and charging of the samples, and for the many helpful discussions.

He thanks Dr. G. Gordon Setser for his help in constructing the He^3 cryostat and related equipment and for his contributions to the development of the delocalized bound hydrogen model. He is grateful to Kai Huang for help in the preparation of the thesis.

Finally, the author is deeply grateful to his wife, Leslie, for her support and understanding during this project.

The support of the United States Department of Energy contract EY-76-C-02-1198 is gratefully acknowledged.

TABLE OF CONTENTS

Page

CHAPTER

1. REVIEW OF THEORY AND PREVIOUS EXPERIMENTS..... 1

1.0 Two Gap Superconductivity..... 1
2.0 Effect of Hydrogen Impurities..... 2
3.0 Hydrogen Interstitial Positions..... 6
4.0 The Birnbaum-Flynn Model..... 9
5.0 Effect of Interstitial Trapping..... 19
6.0 Effects Upon Elastic Constants..... 20

2. EXPERIMENTAL TECHNIQUES AND APPARATUS..... 22

1.0 Sample Preparation..... 22
2.0 Hydrogen and Deuterium Charging..... 22
3.0 Ultrasonic Measurement..... 24
4.0 Cryostat..... 30
5.0 Temperature Measurement and Control..... 34

3. ANELASTIC RELAXATION..... 37

1.0 Relaxation as a Function of Frequency..... 37
2.0 Relaxation as a Function of Temperature..... 41

4. EXPERIMENTAL RESULTS..... 45

1.0 Temperature Dependence of Background Velocity..... 47
2.0 Low Concentration Hydrogen Results..... 47
3.0 Low Concentration Deuterium Results..... 56
4.0 High Concentration Hydrogen Results..... 59
5.0 High Concentration Deuterium Results..... 72
6.0 The Effect of Cooling Rate..... 79
7.0 Effect of Bias Stress..... 80
8.0 Effect of Oxygen Concentration..... 83
9.0 Summary of Experimental Results..... 86

5. A DELOCALIZED BOUND HYDROGEN MODEL..... 89

1.0 The Hindered Rotator..... 90
2.0 Trapping Orientations..... 95
3.0 The Orbach Process..... 104
4.0 The Relaxation Strength..... 108

Page

CHAPTER

6. THE DISCUSSION 113

1.0 Model Parameters 113
2.0 The Polarization Dependence 114
3.0 The Determination of Δ, γ and α 115
4.0 The Deuterium Ultrasonic Results 122
5.0 The Deuterium Decrement 128
6.0 The Heat Capacity Fit 131
7.0 Comparison of Theory with Hydrogen Velocity 136

7. SUMMARY AND CONCLUSION 142

REFERENCES 145

APPENDIX 148

VITA 150

LIST OF FIGURES

Page

Figure

1. Excess heat capacity divided by temperature versus temperature due to hydrogen and deuterium interstitials in niobium..... 5

2. Possible interstitial sites of hydrogen in niobium..... 8

3. Interstitial systems considered by Birnbaum and Flynn (1976) to explain heat capacity of hydrogen in niobium..... 11

4. Energy eigenvalues of octahedral centered tunnelling system..... 15

5. Experimental heat capacities as a function of temperature for hydrogen and deuterium in niobium..... 18

6. The pulse superposition velocity system..... 29

7. The He^3 cryostat insert..... 33

8. The decrement, δ, and elastic constant changes, $\delta C/C$, due to an anelastic relaxation as functions of $\omega\tau$..... 40

9. The decrement, δ, and elastic constant change, $\delta C/C$, for an anelastic relaxation as functions of temperature..... 43

10. The frequency change of the C' mode as a function of temperature..... 49

11. The decrement per unit concentration for H/Nb = 200 ppm and frequency change for H/Nb = 160 ppm as functions of temperature for the C' mode..... 53

12. The frequency change of the C_{44} mode as a function of temperature for H/Nb = 0 and 160 ppm..... 55

13. The decrement per unit concentration and the frequency change of the C' mode as functions of temperature for D/Nb = 230 ppm.... 58

14. The C', C_{11} and B mode frequency changes as functions of temperature for D/Nb = 575 ppm..... 61

Page

Figure

15. The decrement of the C' mode per unit concentration as a function of temperature for H/Nb = 2150 ppm at 10, 30, 50, 70, and 150 MHz..... 63

16. The decrement of the C' mode per unit concentration as a function of temperature for H/Nb = 200 and 2150 ppm..... 66

17. The decrement of the C' and C_{44} modes per unit concentration as functions of temperature for H/Nb = 2150 ppm..... 69

18. The frequency change of the C' mode as a function of temperature for H/Nb = 2150 ppm..... 71

19. The decrement of the C' mode per unit concentration as a function of temperature for D/Nb = 1800 ppm at 3 and 9 MHz..... 74

20. The decrement of the C' and C_{44} modes per unit concentration as functions of temperature for D/Nb = 1800 ppm..... 76

21. The frequency change of the C' mode as a function of temperature for D/Nb = 1800 ppm..... 78

22. The decrement of the C' mode per unit concentration as a function of temperature for H/Nb = 2150 ppm after various quenches..... 82

23. The decrement of the C' mode per unit concentration as a function of temperature for two trap concentrations..... 85

24. The energy levels of the hydrogen system as a function of C' strain..... 93

25. The three orientations of the O-H complex..... 97

26. The energy levels of the hydrogen system indicating bias strains of [111], [110] and [100] orientations..... 100

27. The heat capacity of the hydrogen-oxygen complex as a function of temperature for various C' bias strains..... 103

28. The Orbach activation process..... 106

29. The relaxation strength as a function of temperature..... 111

30. The logarithm of relaxation frequency as a function of inverse temperature..... 117

Page

Figure

31. The relaxation strength versus temperature..... 120

32. The hydrogen wavefunctions determined by the hindered rotator calculation..... 125

33. The deuterium wavefunctions determined by the hindered rotator calculation..... 127

34. The fit of the delocalized bound model to the deuterium decrement for D/Nb = 1800 ppm at 3 and 10 MHz..... 130

35. The heat capacity fit of the delocalized bound hydrogen model.... 134

36. The fit of the theoretical models to the frequency change of the C' mode with 160 ppm of hydrogen..... 138

CHAPTER 1.

REVIEW OF THEORY AND PREVIOUS EXPERIMENTS

The investigation of the properties of interstitial hydrogen in metals has produced interesting results in a number of areas. The embrittlement of metals by stress induced precipitation of the metal hydride (Birnbaum 1976; Birnbaum, Grossbeck and Amano 1976; Cotterill 1961) is a very important technical problem. Of a more fundamental nature is the interest in the delocalized nature of the hydrogen point defect (Alefeld et al. 1975; Birnbaum and Flynn 1976; Lankford et al. 1978).

1.0 Two Gap Superconductivity

Some early work of Suhl, Matthias and Walker (1959) suggested the existence of a second superconducting energy gap in transition metals. Heat capacity (Shen, Senozan and Phillips 1965; Sung and Shen 1965), electron tunnelling (Hafstrom and MacVicar 1970), ultrasonic attenuation (Lacy and Daniel 1971), and thermal conductivity (van der Hoeven and Keesom 1964; Carlson and Satterthwaite 1970) measurements supported the existence of a second gap. However, other results (Anderson, Satterthwaite and Smith 1971; Almond, Lea and Dobbs 1972; Forgan and Gough 1973; Frommer et al. 1973) disputed the existence of a second gap. Further work was necessary to explain these contradictory results.

2.0 Effect of Hydrogen Impurities

Sellers, Anderson and Birnbaum (1973, 1974) measured the heat capacities of Nb, V and Ta at temperatures below 1 K. Prompted by an earlier suggestion by Granato (Sellers 1975) that the anomaly might be due to vibrating dislocations, they investigated the effects of strain and dislocations on the heat capacity. However, they discovered that neither the two gap theory nor dislocations could explain their results. Cold working the specimens decreased the size of the anomaly, consistent with the two gap model, since the damage produced by cold work was expected to destroy the second energy gap. However, when the same sample was vacuum annealled, the anomaly did not return. This was inconsistent with the two gap model, as the annealling would have removed the damage which destroyed the second gap. The anomaly was not consistent with dislocation vibrations, since bending the sample, which increased the number of dislocations as indicated by thermal conductivity results, did not increase the anomaly. Rather, the anomaly decreased in size after bending. Hence, some other mechanism must be responsible for producing the effect.

The fact that the size of the anomaly was reduced by vacuum annealling suggested that interstitial impurities might be responsible. Hydrogen, because of its high solubility in niobium, was suspected. By charging their specimens to about 3000 ppm atomic, with hydrogen or deuterium, they were able to reproduce the anomalies seen earlier, indicating that it was dissolved hydrogen which was responsble for the effect. Results of Faber and Schultz (1972) indicated that it was possible for even ultra-high-vacuum annealled samples to contain relatively large amounts of dissolved hydrogen.

Most of the 3000 ppm of hydrogen present in the sample would be expected to precipitate at low temperatures into the beta phase hydride (Westlake

and Ockers 1975; Whitton et al. 1975). Sellers, Anderson and Birnbaum (1974) suspected that the anomaly was due to hydrogen left in the alpha phase, since the anomaly changed in magnitude by only about a factor of two for a factor of 100 variation in hydrogen content. The entropy obtained from the heat capacity curves indicated that only about 50 ppm atomic hydrogen was responsible for the effect. This is consistent with the assumption that only the alpha phase hydrogen contributes to the effect, and that most of the hydrogen is precipitated into the beta phase.

The difference between the excess heat capacity due to hydrogen and deuterium as shown by Figure 1, suggested that the effect may be due to quantum mechanical tunnelling of the interstitial hydrogen inside the niobium lattice. This was consistent with studies of diffusion of hydrogen in niobium which indicated a non-Arrhenius temperature dependence at low temperature (Baker and Birnbaum 1973), and a nonclassical isotope effect (Mattas and Birnbaum 1975; Matusiewicz and Birnbaum 1977). Theoretical treatments had attributed these effects to quantum tunnelling of the interstitial (Flynn and Stoneham 1970; Sussmann and Weissman 1972). Sellers, Anderson and Birnbaum (1974) concluded that the heat capacity anomaly could be caused by a localized mode of the lattice associated with hydrogen tunnelling in the alpha phase.

The effect of hydrogen and deuterium upon the thermal conductivity of niobium was investigated by O'Hara, Sellers and Anderson (1974). If there exist eigenstates which contribute to the heat capacity, their coupling to phonon modes might also be possible. This would produce a minimum in the phonon mean free path at nearly the same temperatures as the heat capacity contributions.

Figure 1. Excess heat capacity divided by temperature versus temperature due to hydrogen and deuterium interstitials in niobium. (From Sellers 1975).

Curve C - 3000 ppm Hydrogen

Curve D - 3000 ppm Deuterium

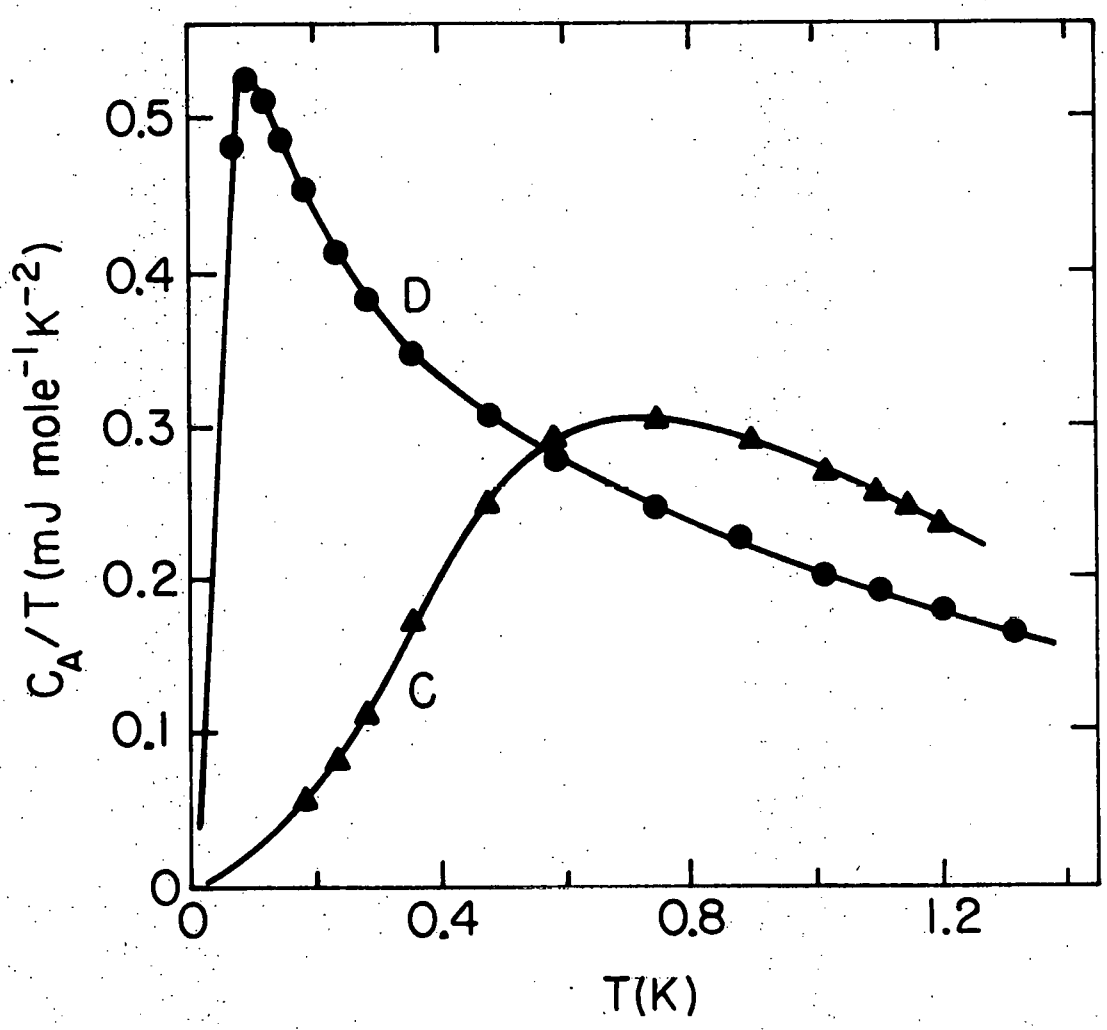
0.5
0.4
0.3
0.2
0.1
0
0
0.4
0.8
1.2
T(K)
C_A/T (mJ mole^{-1}K^{-2})
D
C

Their measurements indicate minima in the phonon mean free path at 0.8 K for hydrogen and 0.1 K for deuterium, where the contributions to the heat capacity occur. Removal of the hydrogen or deuterium eliminates the minima, indicating the connection between phonon scattering and the defects.

The coupling of hydrogen defects to phonons suggests the possibility that the defects may affect the elastic constants and also show relaxation effects. We decided to look for evidence of elastic constant changes and relaxations caused by defect-phonon coupling. While the thermal conductivity results indicated the possibility of a relaxation, there was no detailed model of hydrogen motion available to predict the behavior of the elastic constants.

While this investigation was being pursued, a model was proposed by Birnbaum and Flynn (1976) which described the behavior of a delocalized hydrogen defect which underwent quantum tunnelling between interstitial sites. The splitting of the energy eigenvalues by the tunnelling provided a mechanism which could explain the heat capacity results. The existence of this model made it possible to think more specifically and quantitatively about the types of effects which would occur in the elastic constants. Since their model makes use of several types of interstitial positions, it would be instructive to investigate those positions before attempting to discuss the model.

3.0 Hydrogen Interstitial Positions

Neutron scattering (Somenkov et al. 1968), electron microscopy (Schober et al. 1973) and entropy of solution measurements (Magerl et al. 1973) indicated the occupation of tetrahedral sites by hydrogen at room temperature (Figure 2). Other results in neutron scattering (Stump et al. 1977; Kistner et al. 1971) and Gorsky effect measurements (Gissler and Rother 1970;

Figure 2. Possible interstitial sites of hydrogen in niobium.

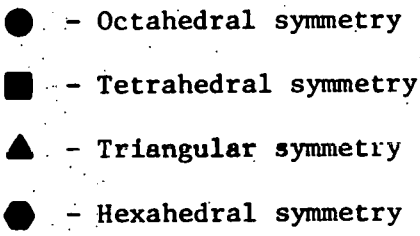

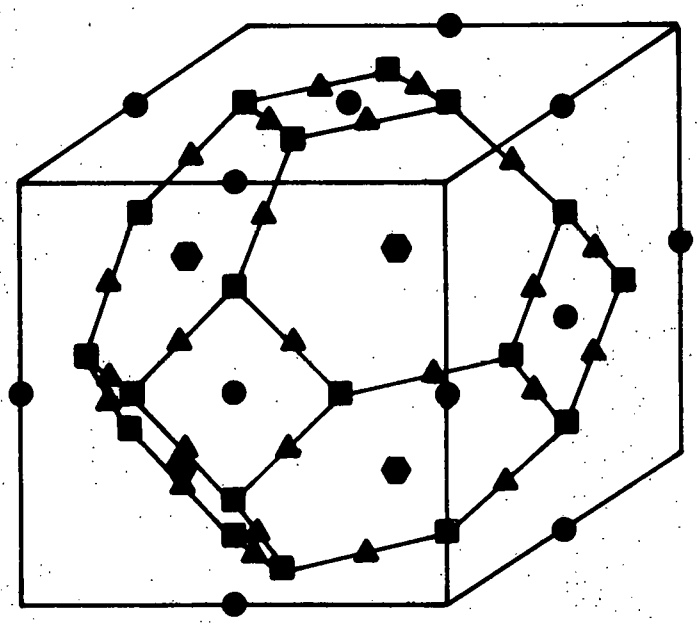

Schaumann et al. 1970) suggested that other sites might also be occupied, especially hexahedral sites.

Channelling measurements (Carstanjen and Sizmann 1972; Shakun et al. 1975) confirmed the tetrahedral site occupation, but did not rule out the possibility of other additional sites.

Diffuse neutron scattering results of Fender (1976) showed that the tetrahedral sites are occupied by hydrogen, and that triangular sites have occupation probabilities almost as large as those for the tetrahedral sites, at least at room temperature. They also indicate at most a very low occupation probability for octahedral sites.

Quasi-elastic neutron scattering from hydrogen and deuterium interstitials in niobium (Gissler et al. 1973; Wakabayashi et al. 1974) indicate that deviations from a harmonic Debye-Waller broadening are best explained using two r.m.s. amplitudes of vibration; 0.14 and about 1 angstrom. The lattice distortion surrounding the interstitials is seen to have almost cubic symmetry (Bauer, Seitz et al. 1975).

4.0 The Birnbaum-Flynn Model

Birnbaum and Flynn began by assuming that hydrogen localizes itself by self-trapping at low temperatures (Flynn and Stoneham 1970). They included the possibility of the hydrogen wave function overlapping onto neighboring interstitial sites. Several systems made of tetrahedral, triangular, and octahedral sites were considered (Figure 3). They compared the properties of each system to the experimental observations. These observations are: (a) Debye-Waller factors indicate two r.m.s. amplitudes

Figure 3. Interstitial systems considered by Birnbaum and Flynn (1976) to explain heat capacity of hydrogen in niobium. Orbital systems are centered on octahedral (a), tetrahedral (b), and triangular (c) sites.

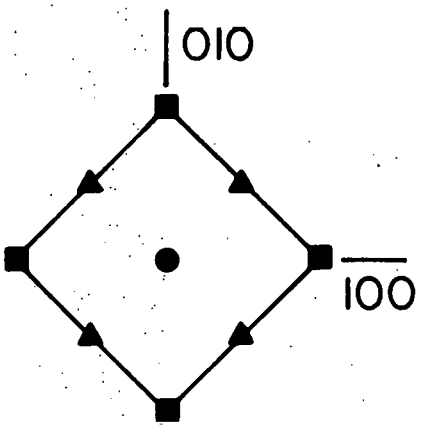

(a)

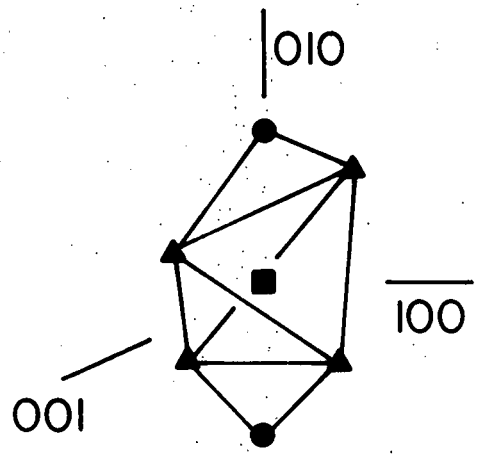

(b)

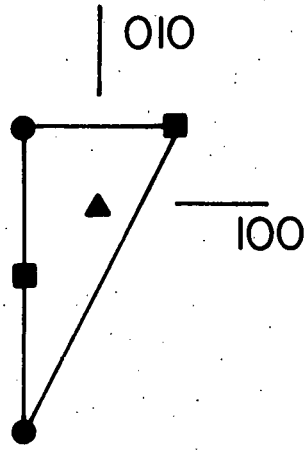

(c)

of vibration, 0.14 and 1 angstrom (Gissler et al. 1973; Wakabayashi et al. 1974); (b) non-classical isotope effects exist in heat capacity (Sellers, Anderson and Birnbaum 1975) and thermal conductivity (Sellers 1975) anomalies; (c) neutron structure analysis (Petrunin et al. 1970) and diffuse scattering (Fender 1976) indicate that tetrahedral sites are occupied, that triangular sites have similar occupation probability at room temperature, and that octahedral sites have a small occupation probability; and (d) lattice distortions surrounding hydrogen interstitials possess almost cubic symmetry (Bauer, Seitz et al. 1975; Buchholz et al. 1973; Bauer and Schmatz 1975).

The neutron scattering results are consistent with all three models if the octahedral sites are constrained to be unoccupied. The 0.14 angstrom Debye-Waller factor corresponds well with the value of 0.12 angstrom expected for a harmonic oscillator with the observed proton energy (Pan et al. 1969; Chernoplekov et al. 1970). The mean ring radius of model (a) of 0.7 angstrom compares favorably with the larger Debye-Waller contribution, while models (b) and (c), being smaller in size, compare less favorably.

To compare the heat capacity results, energy levels of the quantum eigenstates of models (a), (b) and (c) were calculated. A matrix method was used, assigning diagonal energies ϵ and zero to tetrahedral and triangular sites respectively, and an off-diagonal term V representing transitions between adjacent sites. Diagonalization of the 8 × 8 matrix gives for model (a)

$$E_1,\ E_8 = 2V[w \mp \sqrt{w^2 + 1}] \tag{1.1}$$

$$E_{2,3},\ E_{6,7} = 2V[w \mp \sqrt{w^2 + 1/2}] \tag{1.2}$$

$$E_4 = 0, \quad E_5 = 4Vw. \tag{1.3}$$

Model (b) gives,

$$E_1, E_5 = 2V[w \mp \sqrt{w^2 + 1}] \tag{1.4}$$

$$E_2, E_3, E_4 = 0 \quad , \tag{1.5}$$

and similarly, model (c) gives,

$$E_1, E_3 = 2V[w \mp \sqrt{w^2 + 1/2}] \tag{1.6}$$

$$E_2 = 0 \quad , \tag{1.7}$$

where $w = \epsilon/4V$.

The heat capacity is calculated from these energy levels using

$$C = d\{kT^2(d/dT)[\ln \sum_i \exp(-E_i/kT)]\}/dT \quad . \tag{1.8}$$

None of the models presented before reproduces the observed heat capacity anomaly, but (a) is closest, so it was used throughout the rest of the calculations. Its energy levels are shown as functions of w in Figure 4.

The two doublets $E_{2,3}$ and $E_{6,7}$ couple to strains of the lattice. This coupling produces static distortions similar to those produced in Jahn-Teller systems. Random internal strains produced by hydride precipitates, neighboring defects, etc., can also couple to these states, producing

Figure 4. Energy eigenvalues of octahedral centered tunnelling system are shown as a function of $w = \varepsilon/4V$, where ε is the energy difference between tetrahedral and triangular sites, and V is the off-diagonal overlap integral. (From Birnbaum and Flynn 1976).

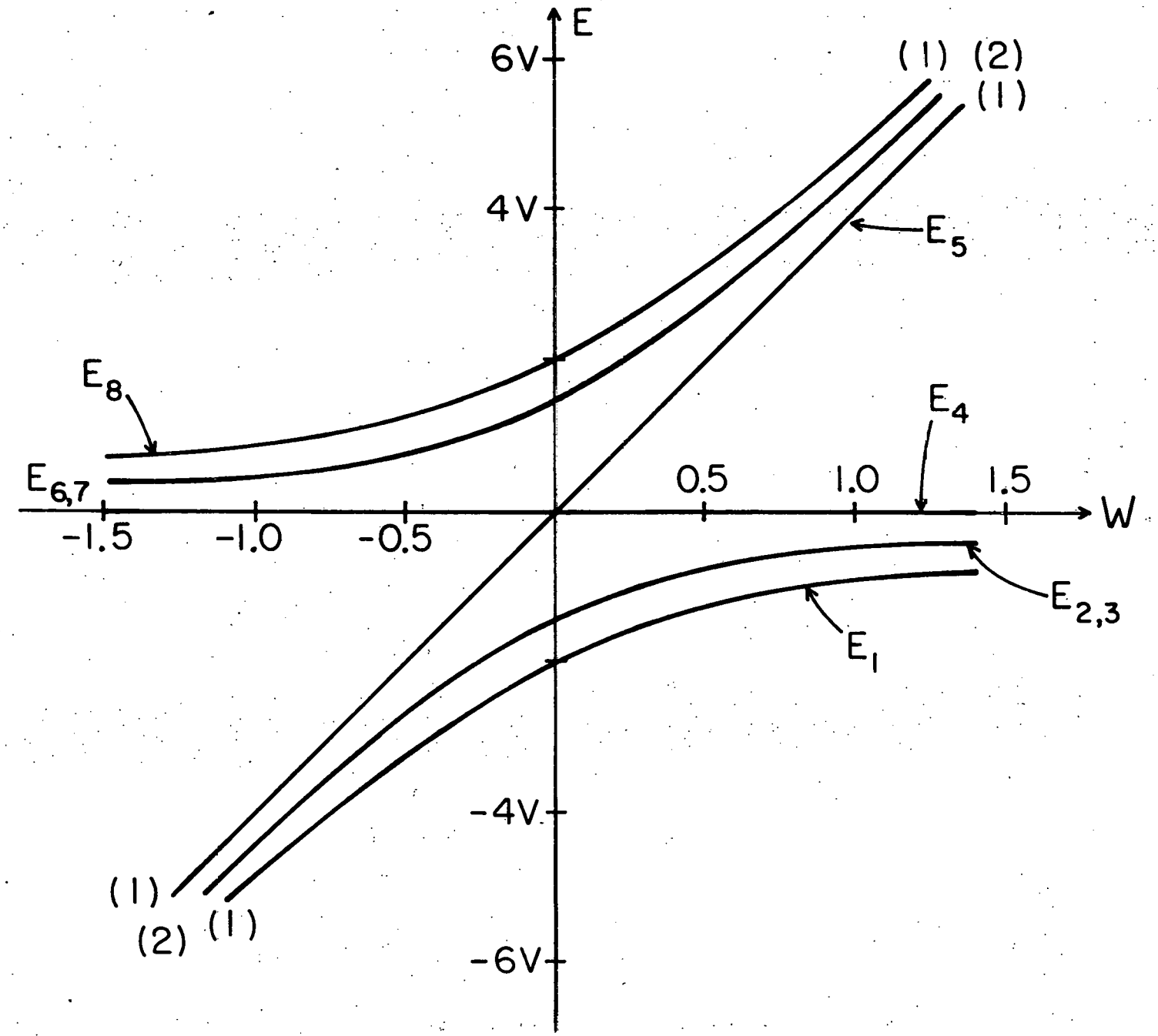
E
6V
4V
-4V
-6V
(1) (2)
(1)
E5
E8
E6,7
E4
0.5
1.0
1.5
W
-1.5
-1.0
-0.5
E2,3
E1
(1)
(2) (1)

a distribution in the density of states as a function of energy. Birnbaum and Flynn acknowledged that the strain coupling parameters and strain field distributions are unknown, so they assumed a uniform distribution of doublet energy splittings from zero to αV_d where V_d is the deuteron overlap integral. They assumed that the strain coupling parameters for hydrogen and deuterium were nearly identical, so the energy splitting would also be the same. However, the tunnelling is different, so they assumed the hydrogen overlap integral V_h was related to V_d by $\beta = V_h/V_d$.

Their fit to the heat capacity is shown in Figure 5. The temperature and heat capacity have been normalized to 1 relative to the values at the deuterium peak temperature T = 1.42 K. The two adjustable parameters have values $\beta = 3$ and $\alpha = 0.5$. The fit was insensitive to the offset energy w and did not strongly depend upon α. The energy level diagrams for both hydrogen and deuterium corresponding to the best fit are shown in the lower right corner of Figure 5.

Birnbaum and Flynn attribute the success of the model in duplicating the heat capacity results to three features: (a) the first excited state is a degenerate doublet; (b) the strain splitting lowers some of the excited states close to the ground state for deuterium, but not for hydrogen, because of the isotope effect in V; and (c) there exist more states above the first excited states to account for contributions to the heat capacity at still higher temperature. They conclude that other tunnel-split systems could possibly reproduce these results, but that it is unlikely.

Finally, the authors treat the subject of the near-cubic nature of the observed lattice strain surrounding the defects. They sum the contributions

Figure 5. Experimental heat capacities as a function of temperature for hydrogen and deuterium in niobium. The open circles are for as-received specimens, while the closed circles are for 3000 ppm charged specimens. The solid lines represent the fit of the Birnbaum-Flynn model for $\alpha = 0.5$ and $\beta = 3$. The broken curve represents the deuterium calculation for $\alpha = 1.5$ and $\beta = 3$ (displaced vertically for clarity). The energy level spectra for hydrogen and deuterium are shown at the lower right. (From Birnbaum and Flynn 1976).

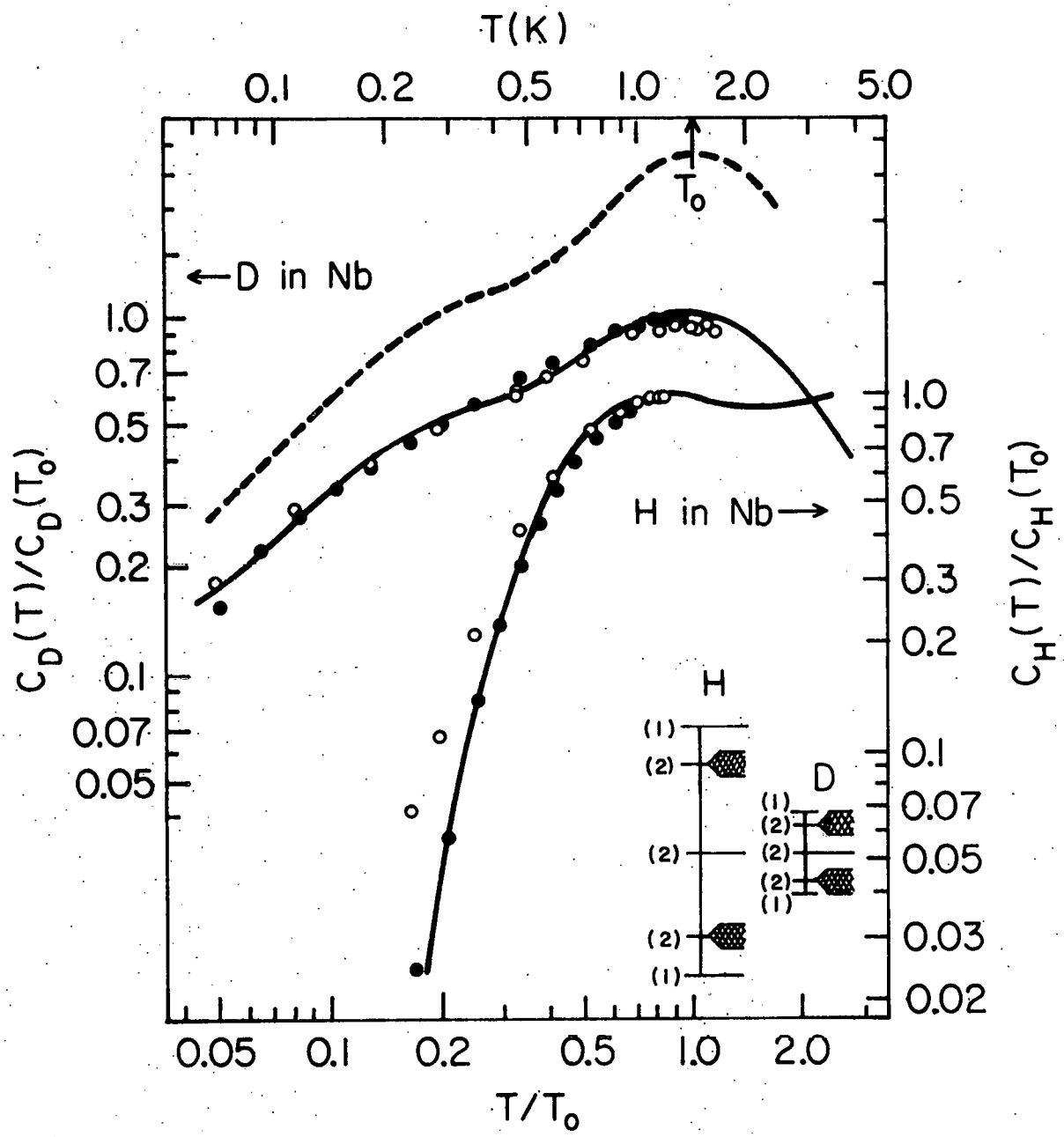
T(K)
0.1
0.2
0.5
1.0
2.0
5.0
T₀
←D in Nb
H in Nb→
1.0
0.7
0.5
0.3
0.2
0.1
0.07
0.05
C_D(T)/C_D(T₀)
C_H(T)/C_H(T₀)
H
D
(1)
(2)
0.03
0.02
0.05
0.1
0.2
0.5
1.0
2.0
T/T₀

to the lattice strain from all eight interstitial sites to obtain an average strain field. This strain field turns out to be nearly cubic due to cancellation of the non-cubic terms in the sum.

The Birnbaum-Flynn model, as presented, describes the behavior of a delocalized, unbound hydrogen atom. The possibility of binding the hydrogen to another defect has not been considered. This effect of binding, or trapping, of the hydrogen will become very important, in view of recent discoveries.

5.0 Effect of Interstitial Trapping

As mentioned previously, the low temperature limit of the solubility of hydrogen in niobium is expected to be quite small (Whitton et al. 1975; Westlake and Ockers 1975). As early as 1973, Baker and Birnbaum showed that anelastic relaxations of hydrogen charged niobium which appear around 150K at 10 MHz were due to complexes of hydrogen with nitrogen and oxygen (Baker and Birnbaum 1973; Mattas and Birnbaum 1975). Relaxations of hydrogen pairs were also seen, but no evidence was seen of isolated, indivdual hydrogen relaxations. These relaxations are believed to be caused by reorientation of the hydrogen around the trapping interstitial in the presence of the applied stress. Separate relaxations were seen for different polarizations of the ultrasonic wave, indicating that more than one symmetry of the hydrogen-trap system exists.

Resistance measurements by Pfeiffer and Wipf (1976) verified the trapping of hydrogen in nitrogen in niobium. Their analysis indicates that only one hydrogen atom traps at any one nitrogen interstitial with a binding energy of 0.12 eV, consistent with the results of Baker and Birnbaum.

The heat capacity experiments by Sellers, Anderson, and Birnbaum (1973, 1974) were redone by Morkel, Wipf, and Neumaier (1978) to investigate the effect of nitrogen trapping. They found that no excess heat capacity was present in nitrogen free samples. The introduction of nitrogen produced excess heat capacities similar to those seen previously by Sellers, Anderson and Birnbaum (1973, 1974) for both hydrogen and deuterium. They conclude that the excess heat capacity can be accounted for by assuming that the hydrogen traps into a localized site near a nitrogen interstitial without undergoing delocalized tunnelling. There exist various orientations of the H-N defect which are degenerate by symmetry. This degeneracy can be lifted by the interaction of the defect strain fields due to other neighboring defects. They estimate that a concentration of about 3000 ppm of nitrogen, which was used as the trapping defect, could cause splittings as large as 10^{-3} eV. This is more than the amount required to exhibit the observed heat capacity effect. The splitting is dependent upon the trapping concentration, so that the temperature dependence as well as the size of the heat capacity effect would be affected by the trapping concentration. This behavior will be referred to as the localized bound model.

6.0 Effects Upon Elastic Constants

There exist two models of hydrogen motion in niobium, the Birnbaum-Flynn delocalized unbound model, and the localized bound model of Morkel, Wipf and Neumaier. Both models allow for the existence of elastic constant changes and a relaxation. The Birnbaum-Flynn model provides a more specific basis for predictions than the Morkel, Wipf and Neumaier model. However, neither model can adequately account for all the available experimental

data. It was hoped that a study of the ultrasonic relaxation would provide sufficiently detailed results to decide between the existing models, or to require the creation of a new model. As will be seen, a modification of the Birnbaum-Flynn model to take account of hydrogen trapping can be used to explain the ultrasonic data as well as other results.

CHAPTER 2.

EXPERIMENTAL TECHNIQUES AND APPARATUS

1.0 Sample Preparation

Two cubic specimens slightly larger than one centimeter dimension were spark cut from a six inch section of a single crystal niobium rod one inch in diameter which was supplied by Dr. H. K. Birnbaum. The surfaces were oriented with one set of (100) faces and two sets of (110) faces. The orientation was done by x-ray diffraction to within 1/2 degree using the double exposure method of Ochs (1968). The surfaces were mechanically polished by mounting in stainless steel polishing disks and using diamond paste as an abrasive. The surfaces were measured to be flat within one wavelength of sodium light and parallel to 3×10^{-5} radians.

Impurity analysis indicated that the primary impurity was Ta with large amounts of N, O and C. Concentrations of these and other impurities are listed in Table 1.

One sample was returned to the ultra high vacuum system for oxygen treatment. It was heated to 1800 C in an atmosphere of 10^{-6} Torr oxygen to remove carbon and nitrogen impurities. The pressure was then increased to 2×10^{-6} Torr for a period of five hours to introduce approximately 1000 ppm of oxygen.

2.0 Hydrogen and Deuterium Charging

Sample charging with hydrogen and deuterium was done from the gaseous phase at high temperature. Two methods of gas charging were used, a thermodynamic equilibrium method and a measured volume method.

TABLE 1.

IMPURITY CONCENTRATION IN PARTS PER MILLION BEFORE FINAL ANNEAL

Ta	200	Na	< 1	Zn	< 0.06
C	70	W	0.8	Fe	0.05
O	64	In	< 0.3	Cu	< 0.04
N	40	Al	0.2	Cr	< 0.04
Cl	< 9	Pb	0.1	Ti	< 0.04
Si	3	Mo	< 0.1	Ni	0.04
Ca	3	Sb	< 0.1	Mn	< 0.03
K	2	Au	< 0.08	V	< 0.03
Se	2	Re	< 0.08	As	< 0.03
Mg	1	Zr	< 0.06		

Originally the equilibrium method was used. It consisted of heating the specimen to about 600 C in a vacuum of 10^{-8} Torr. Hydrogen or deuterium, which had been purified by passing through a palladium cell, was introduced to the vacuum chamber at the pressure required to equilibrate the concentration of the gas in the sample to the desired value. As the temperature of the sample was lowered, the pressure of the gas was correspondingly reduced to maintain equilibrium. When the sample had cooled to about 100 C, air was introduced into the chamber, forming an oxide layer on the sample and sealing the surface against further hydrogen passage.

After the experiments were performed, the sample was outgassed at high temperature and the evolved gas was collected into a known volume. The

original concentration of gas in the sample could then be calculated. After several chargings it was discovered that the concentration of gas in the sample was beginning to fall below the value expected from thermodynamic consideration. It was felt that this could possibly be caused by surface contamination of the sample which interferred with the equilibration of gas concentration. Hence it was decided to use a measured volume method for charging, which would give an immediate indication of proper charging.

In the measured volume method, the amount of hydrogen or deuterium required to achieve the desired concentration in the sample was calculated. This amount was measured into a calibrated volume, and was then bled into the sample chamber. The sample was heated, absorbing almost all of the gas before equilibrium was achieved. Much better success was obtained with this method, except when charging to very high concentrations, around 1000 ppm. The sample chamber then had to be pressurized to a higher pressure, with the concentration of gas in the sample calculated from the difference between initial and final pressures.

3.0 Ultrasonic Measurement

Measurements were made on two samples, designated Nb1 and Nb2. All experiments but one were conducted with Nb1. This sample was initially charged with oxygen to a concentration of approximately 1000 ppm. Experiments were conducted using various additional concentrations of hydrogen and deuterium. The purpose of the oxygen doping was to provide trapping centers for the hydrogen, and to reduce precipitation into the beta phase (Westlake and Ockers 1975; Whitton, et al. 1975). Nb2 was not charged with oxygen, but analysis showed an inherent concentration of about 200 ppm of oxygen,

carbon and nitrogen, combined. Polarization of the ultrasonic wave was adjusted by choosing longitudinal or transverse transducers and mounting upon the appropriate face. Table 2 lists the elastic constant measured for each polarization.

TABLE 2.

ELASTIC CONSTANT VERSUS POLARIZATION

Polarization	Elastic Constant
[100] Longitudinal	$C_{11} = (B + 4C')/3$
[100] Transverse	C_{44}
[110] Transverse along [100]	C_{44}
[110] Transverse along $[1\bar{1}0]$	$C' = (C_{11} - C_{12})/2$

Therefore the sets of (100) and (110) faces allow measurement of the three independent elastic constants C', C_{44}, and B, the bulk modulus. C_{44} can be measured by two different polarizations, allowing a check of the data. B, the bulk modulus, cannot be measured directly to the accuracy required, but it can be derived from the measurements of C_{11} and C'.

The sound was generated and detected by 3 MHz and 10 MHz quartz transducers cut for shear and longitudinal modes of propagation. The transducers were bonded to the sample using Nonaq stopcock grease. Due to the difference in thermal expansion between the quartz and niobium sample, great care had to be taken to insure the survival of the bond while cooling from room temperature to helium temperature. The cooling rate had to be adjusted so as not to exceed 1 K/min. A good quality bond could survive cooling rates

as high as 10 K/min, but as this sometimes led to irreversible changes in bond characteristics, it was avoided except during quenching experiments.

The procedure for producing a good bond is of such importance that it will be summarized here. The sample surface and transducer were cleaned in acetone, and the sample was heated to about 40 C by placing upon a warm block of aluminum. A drop of Nonaq was placed under vacuum and warmed slightly to evaporate any condensed water. A very small drop of the Nonaq was transferred to the sample surface. The transducer was placed over the drop and wrung down using the eraser end of a pencil. Wringing continued in a circular and figure-eight pattern to remove as much Nonaq as possible from beneath the transducer. Eventually, the bond would noticeably stiffen and seize to the surface. The sample could then be removed from the aluminum block and cooled to room temperature. The bond was immediately tested using a Sperry Attenuation Comparator to determine the quality. The bond could be immediately remade if it was not of sufficient quality to use.

Measurement of decrement was performed using Matec Models 6000 and 2470A pulse echo generator and attenuation recorder. The pulse generator was frequency variable and generated a pulse about one microsecond in length. The frequency could be adjusted to any odd harmonic of the transducer fundamental frequency, allowing a large variation in the measurement of decrement versus frequency. The attenuation recorder measured the logarithmic difference in amplitude of two echoes in units of decibels. Dividing by the transit time between echoes gave the attenuation in decibels/μsec. The decrement was obtained by the relation (Truell, Elbaum and Chick 1969)

$$\delta = \alpha/8.68\ f \qquad (2.1)$$

where α is the attenuation in db/μsec and f is the frequency in MHz.

Velocity was measured with a pulse superposition system (Holder 1970). Stability is determined by the frequency synthesizer (Figure 6). The output frequency, usually 10 MHz, is divided by an integer D and triggers a pulse generator. The pulse generator controls the gated amplifier, which passes a 1 microsecond segment of the 10 MHz wave on to the driving transducer mounted on the sample. The receiving transducer detects the echoes, which are amplified and rectified by the RF amplifier. The amplitude of the echoes depends upon the phase relationship between the applied pulse and the echoes. When the ratio D/f is equal to an integer multiple of the round trip transit time, constructive interference occurs, and the echoes have maximum amplitude. A low frequency (35 Hz) reference signal from the lock-in amplifier is used to frequency modulate the 10 MHz wave. The frequency modulation of the 10 MHz produces a corresponding amplitude modulation of the echoes. The output of the lock-in amplifier is proportional to the amount by which the modulation is displaced from the center of the amplitude maximum. The output of the lock-in, when integrated, is used to provide the error signal to correct the frequency synthesizer and maintain the relationship between D/f and the transit time. The velocity is determined by

$$v = 2\, n\ell f/D \tag{2.2}$$

$$\delta v/v = \delta f/f \tag{2.3}$$

where ℓ is the length of the sample and n is the number of round trip transits per driving pulse. The corresponding elastic constant C_{ij} is related to the velocity by

Figure 6. The pulse superposition velocity system. The synthesizer produces a 10 MHz continuous wave which is frequency modulated by the lock-in reference signal. A digital frequency divider triggers a pulse generator every D cycles of the 10 MHz wave, which turns on a gated amplifier for 1 microsecond, delivering the pulse to a transducer mounted on the sample. The lock-in measures the echoes from the RF amplifier, providing an error signal which is integrated to provide a correction to the frequency synthesizer.

PULSE SUPERPOSITION VELOCITY SYSTEM

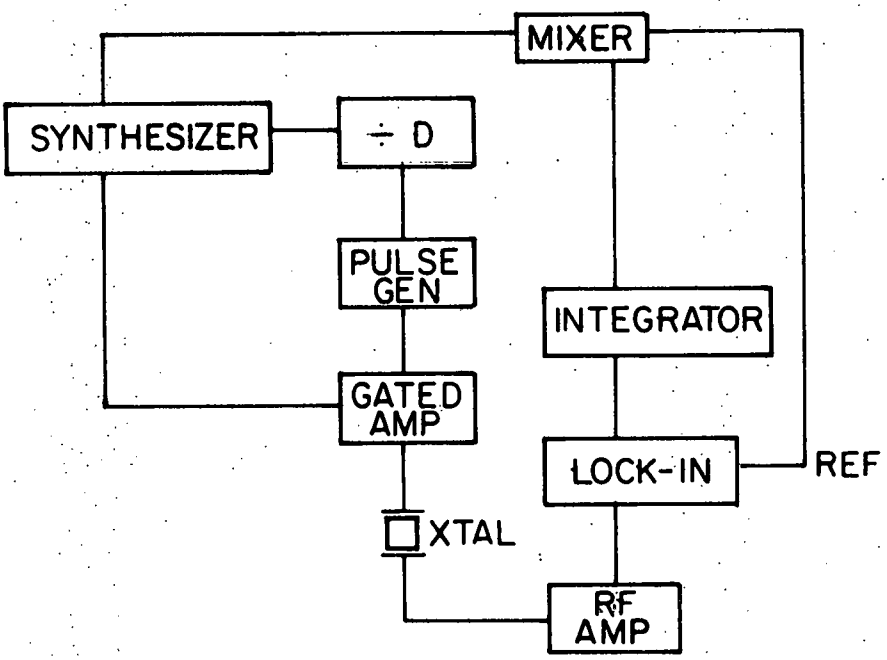

$$C_{ij} = \rho v^2 \quad . \tag{2.4}$$

For small changes in velocity and at low temperature, where the thermal expansion is small, the frequency is related to the corresponding elastic constant by

$$\delta C/C = 2\ \delta f/f \quad . \tag{2.5}$$

Measurement of the frequency of the 10 MHz wave is sufficient to determine relative changes in the elastic constants. With materials having low background decrement, such as niobium, it is possible to measure changes in frequency as small as 1 Hz, corresponding to a sensitivity of 2×10^{-7} in the elastic constant.

The use of separate transducers for driving and detecting was prompted by the need to investigate the low temperature behavior of the velocity, and so required the use of very small amplitude pulses to prevent acoustic heating of the sample. When the same transducer is used for driving and detecting, an overload of the RF amplifier occurs, which reduces the maximum gain available. Using separate transducers eliminates the overload, allowing higher gains from the RF amplifier, and the use of smaller amplitude pulses.

4.0 Cryostat

It was decided that the measurements of velocity and attenuation should extend to temperatures comparable to those used in the heat capacity experiments, 0.1 to 1 K. A He^3 refrigerator fit this requirement and had the advantage of being much simpler to build and operate than a He^3-He^4 dilution refrigerator.

The insert shown in Figure 7 is immersed in liquid He^4. An outer can (A) compresses the inner can (B) against an indium O-ring, creating a vacuum tight cryogenic seal. The inner can is evacuated to about 2×10^{-6} Torr for thermal insulation. A valve (C) operated manually from outside the cryostat is opened to allow liquid He^4 to fill the He^4 pot (D). The valve is closed and the He^4 pot is evacuated with a mechanical pump having a pumping speed of 500 liters/min. This lowers the temperature of the He^4 pot to 1.3 K. He^3 gas is introduced into the He^3 chamber (F). The He^3 gas condenses on the inside wall of the He^4 pot and drops down the tube to collect at the bottom of the He^3 chamber. The He^3 chamber is then pumped using a 300 liter/sec, high throughput diffusion pump, lowering the temperature of the copper cold plate (G) at the bottom of the He^3 chamber to 0.3 K. A radiation shield (E) hung from the He^4 pot provides additional thermal isolation for the sample volume.

A thermal impedance is introduced between the cold plate and the sample plate (H). A heater and thermometers are mounted on the sample plate along with the sample (I). The thermal impedence allows the sample to be held at temperatures higher than 0.3 K without rapidly vaporizing all the liquid He^3. The thermal impedence was designed to give a cooling time constant of about one second in the range of He^3 temperatures. This was short enough to give good coupling when the lowest temperatures were desired, but large enough to give some isolation at higher temperatures.

The sample is held against the sample plate to maintain good thermal contact with the heater and thermometers. Provision is left for mounting a bellows (J) below the sample for applying bias stresses to the sample.

The bellows was pressurized with He^4 gas. At temperatures below 1 K and pressures above about 25 bars, the He^4 solidifies. Also, the maximum

Figure 7. The He^3 cryostat insert.

A - Outer can

B - Inner vacuum can

C - He^4 fill valve

D - He^4 pot

E - Radiation shield

F - He^3 chamber

G - Copper cold plate

H - Sample plate

I - Sample

J - Pressure bellows

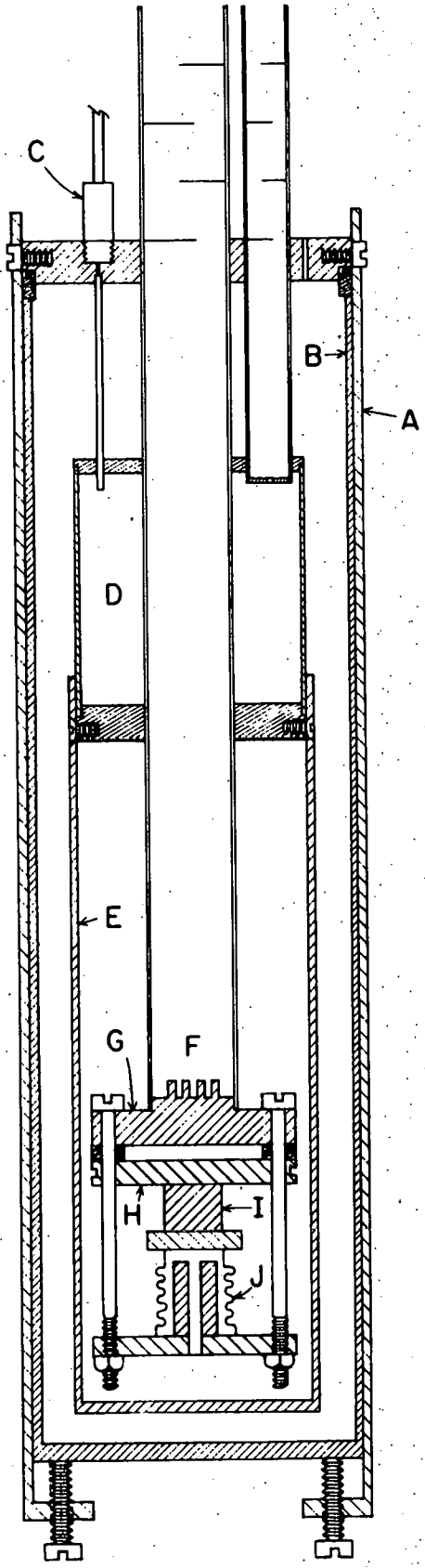
C
B
A
D
E
G
F
H
I
J

rated pressure of the bellows was 7 bars. Therefore, the pressure of He^4 was kept below 6 bars at all times. The sample cross section was considerably smaller than the bellows cross section, which allowed the applied stress on the sample to reach about 28 bars. At these pressures and temperatures the He^4 in the bellows and supply tube were liquified, so great care had to be taken when changing the bias temperature and pressure. Instability in the pressure occurred above 8 K, so no experiment was attempted above that temperature with the use of bias stress.

5.0 Temperature Measurement and Control

Temperature measurements were done with two germanium resistance thermometers (Scientific Instruments) and a platinum resistance thermometer (Rosemount Inc.). One of the germanium thermometers was designed for use with a He^3 refrigerator and was calibrated from 9000 ohms at 0.3 K to 50 ohms at 3 K. The other germanium thermometer was more useful at higher temperatures, varying from 20,000 ohms at 1.5 K to 2 ohms at 100 K. The platinum thermometer was useful from 40 K to room temperature, varying from 5 ohms to 100 ohms in this interval.

A four terminal AC measurement was utilized, with a bridge design developed by Anderson (1972). The sensitivity was better than a part in 10^4, to the limit of the thermometer calibration. A PAR 113 preamp and PAR 120 lock-in amplifier were used to improve sensitivity and noise immunity. A reference frequency of 25 Hz was chosen to minimize the effect of lead capacitance and inductance.

The output of the lock-in amplifier, proportional to the bridge imbalance, was used for temperature control. Voltages which were the integral of, differential of, and proportional to the error signal were summed. The

heater voltage was derived from this sum. The time constants of the integral and differential signals and the gain of all three signals were variable. A variable resistance in series with the heater allowed the controller to be used from 0.3 K, where microwatts of heater power were required, to room temperature, where several watts of power were necessary to make temperature changes at a reasonable rate. The temperature controller was able to maintain the temperature to within one millikelvin over a temperature range from 0.3 K to over 20 K. From 20 K to 50 K none of the thermometers had sufficient sensitivity to maintain the temperature stability to better than 1 millikelvin. However, since most of the measurements of velocity and attenuation were made from 0.3 to 15 K, no problem with temperature control occurred.

The germanium thermometers, as supplied, were mounted inside small copper cylinders 0.093 by 0.1875 inches, which were soldered to a small plate. The plate was then screwed to the sample plate. The copper cylinder contained He^4 as thermal exchange gas. However, at the lowest temperatures, the He^4 condensed, reducing the thermal conductivity through the case. The lowest thermal impedence was then through the electrical leads. Hence, at the lowest temperatures, if the electrical leads were not well thermally grounded to the sample plate, large errors in temperature measurement were possible. This became a severe problem below 0.5 K.

To improve thermal conductivity through the electrical leads, the copper cylinder containing the thermometer was removed from the mounting plate. A copper rod was threaded on one end to mount into a hole in the sample plate. The thermometer was inserted into a snugly fit hole in the opposite end of the rod, vacuum grease being used to improve thermal contact. A layer of rice paper was cemented around the rod using GE 7031 varnish. The paper

provided electrical insulation while its small thickness (0.0005 inch) did not adversely affect thermal conductivity. The electrical leads were replaced with 0.005 inch manganin wire and wound around the rod. Another layer of varnish was used to cement the leads to the rod. This provided excellent thermal contact between the thermometer, electrical leads, and the sample plate. This technique has been used on thermometers which operate down to 0.3 K with very good results.

CHAPTER 3.

ANELASTIC RELAXATION

The introduction of a substitutional or interstitial defect into a lattice produces a distortion of the neighboring atoms to accommodate the solute atom. The anisotropy of the distortion will reflect the symmetry of the defect site. For some defect symmetries there will exist more than one orientation or position of the defect having the same energy. The application of the appropriate external stress can remove the degeneracy, causing a redistribution of the number of defects in the various orientations. This ordering of defect concentrations leads to the production of an additional lattice strain due the corresponding ordering of the distortion surrounding the defect. This additional strain is reflected in changes in the elastic constants and internal friction. The process whereby an applied stress leads to ordering of an internal variable which produces a change in the elastic constants is referred to as anelastic relaxation.

An excellent review of anelastic relaxation is provided by Nowick and Heller (1963,1965) and Nowick and Berry (1972). The results that are relevant to this discussion will be presented here.

1.0 Relaxation as a Function of Frequency

Transitions between defect orientations are assumed to occur with a characteristic time, defined as the relaxation time, τ. When an external stress with an angular frequency ω is applied, the response of the decrement,

δ, and the relative change in the elastic constant, $\delta C/C$, are given by the Debye equations:

$$\frac{\delta}{\pi} = \Delta \frac{\omega\tau}{1 + \omega^2\tau^2} \tag{3.1}$$

$$\frac{\delta C}{C} = \Delta \frac{1}{1 + \omega^2\tau^2} \tag{3.2}$$

where Δ is the relaxation strength. The relaxation strength is temperature dependent, and for classical systems is given by

$$\Delta = \frac{\beta c_o v_o}{kT} C(\delta\lambda)^2 \tag{3.3}$$

where β is a dimensionless geometrical constant of order unity, c_o is the atomic concentration of defects, v_o is the molecular volume, C is the appropriate elastic constant, k is Boltzmann's constant, T is the temperature, and $\delta\lambda$ represents the difference in the lambda tensor between the defect orientations. The lambda tensor represents the distortion of the lattice by the defect and is defined as the strain produced per unit concentration of defects in the same orientation.

The temperature dependence of the relaxation strength for a quantum mechanical system can be different from that given above. In general, the relaxation strength will approach the classical value at high temperatures, but can exhibit deviations at lower temperatures. The comparison of the classical and quantum mechanical behaviors will be made in the discussion.

The behavior of the decrement and elastic constant are displayed in Figure 8 as functions of the product $\omega\tau$. The decrement is seen to peak

Figure 8. The decrement, δ, and elastic constant changes $\delta C/C$, due to an anelastic relaxation as function of $\omega\tau$. δ is the relaxation strength. $\omega\tau$ is represented by a log scale.

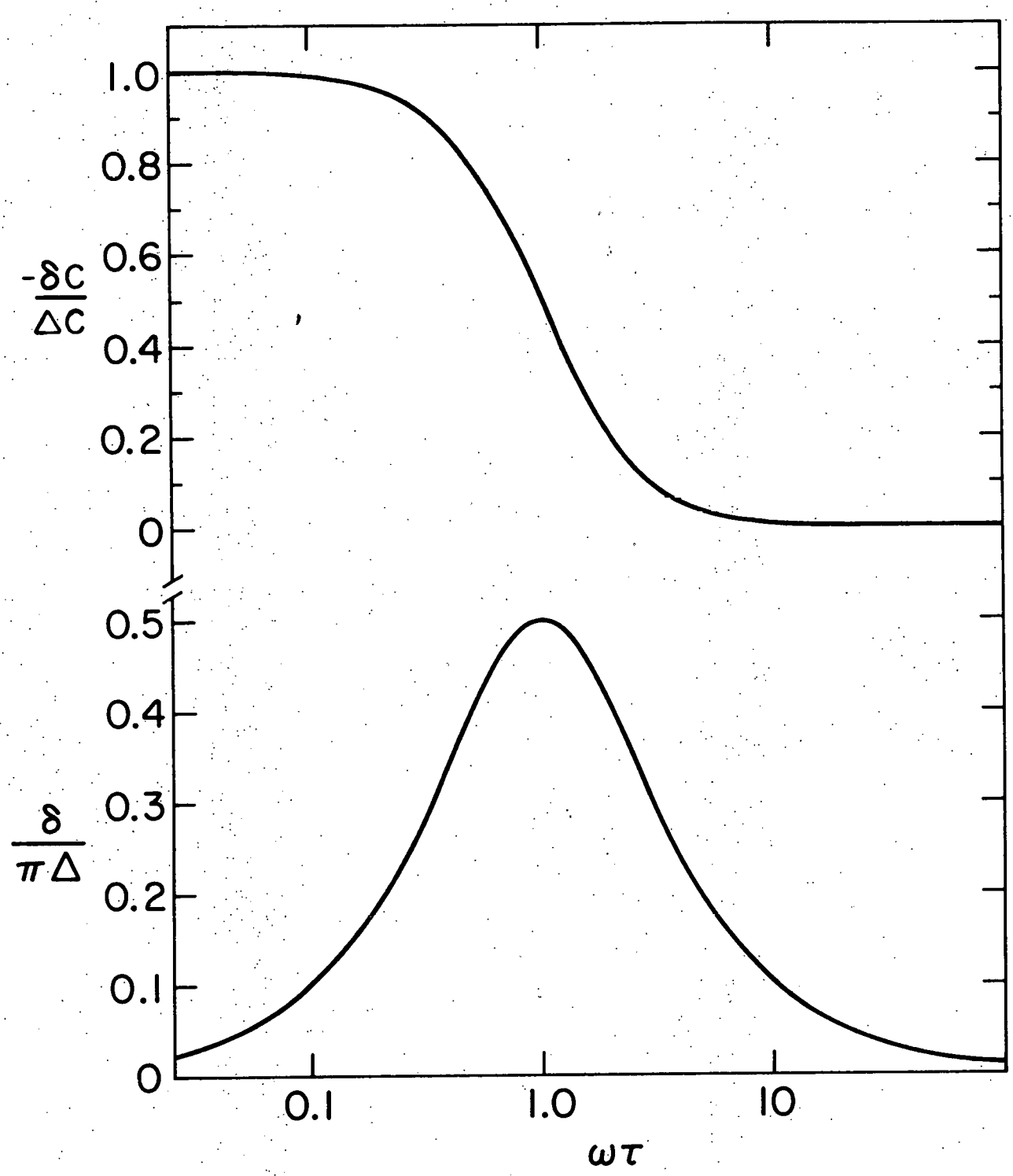
1.0
0.8
0.6
0.4
0.2
0
$-\frac{\delta C}{\Delta C}$
0.5
0.4
0.3
0.2
0.1
0
$\frac{\delta}{\pi \Delta}$
0.1
1.0
10
$\omega\tau$

at a frequency where $\omega\tau = 1$, where a dispersion in the elastic constant occurs. The decrement peaks at a value of $\pi\Delta/2$ while the relative change in the elastic constant, $\delta C/C$ is equal to Δ for small values of $\omega\tau$.

2.0 Relaxation as a Function of Temperature

The forms of the response functions have been shown to be simple when expressed as functions of $\omega\tau$. The independent variable was assumed to be ω, with τ kept constant. Since it is usually difficult to vary ω by more than one or two orders of magnitude when measuring any one sample, this usually means the preparation of several samples to cover various frequencies. It is usually simpler to vary τ by varying the temperature. The temperature dependence of τ may take various functional forms, but often the function follows the Arrhenius equation,

$$\tau = \tau_o e^{Q/kT} \tag{3.4}$$

where Q is the activation energy and k is Boltzmann's constant. The response functions for this temperature dependence are similar to those shown in Figure 9. The decrement response is again a single peak at a temperature where $\omega\tau$ equals one. The response in the elastic constant is qualitatively different. At low temperature, where τ is very large, $\delta C/C$ is small because the defect does not move fast enough to make a transition during a cycle of stress. At higher temperatures, the elastic constant decreases, the dispersion occurring in the same temperature range as the peak in the decrement. At still higher temperatures, instead of becoming constant the elastic constant rises again to its low temperature value. This occurs because of the 1/T temperature dependence of the relaxation strength, as seen in Equation (3.3).

Figure 9. The decrement, δ, and elastic constant change, $\delta C/C$, for an anelastic relaxation as functions of temperature. The decrement peak and elastic constant decrease are centered at a temperature where $\omega\tau = 1$.

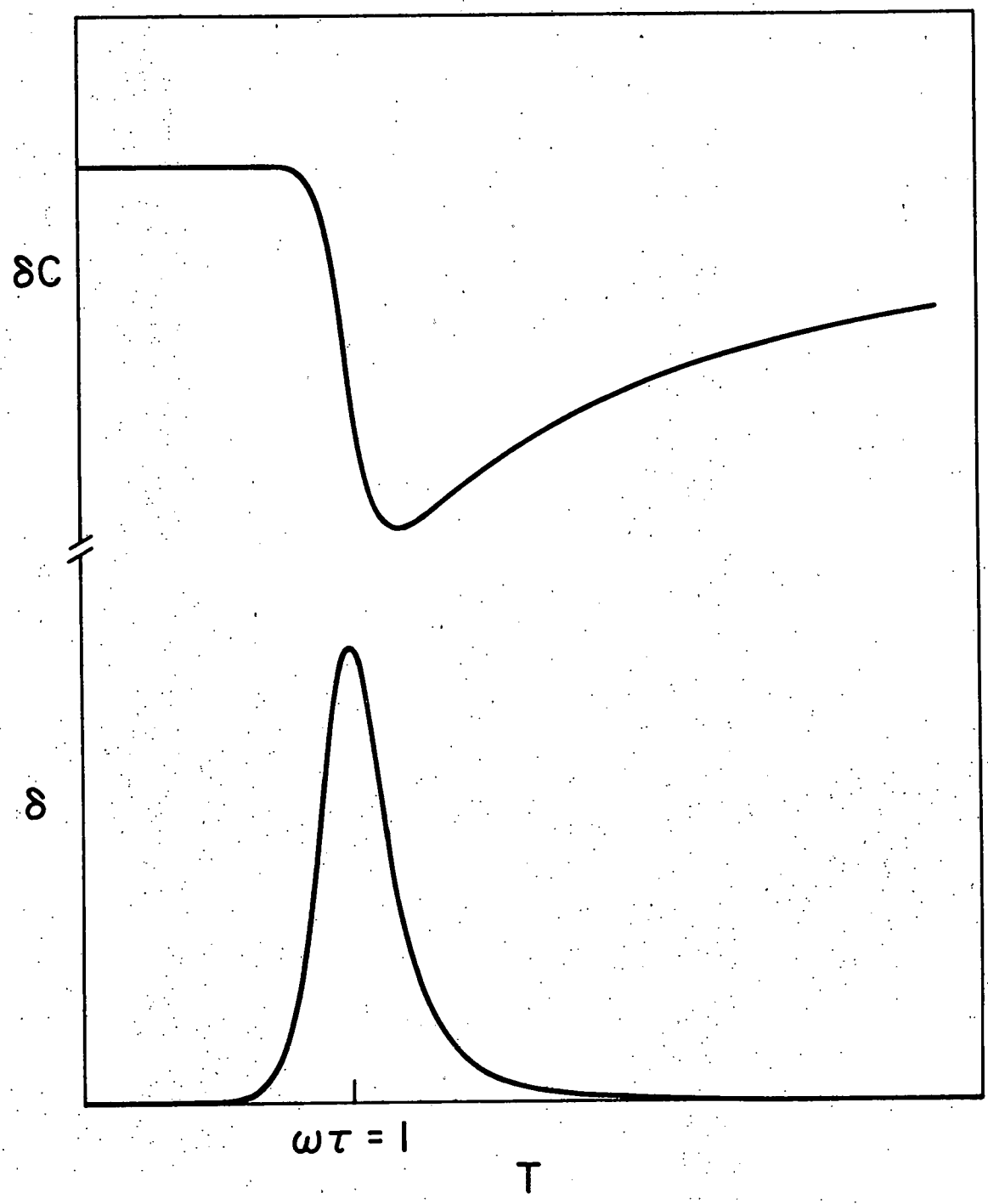
δC
δ
ωτ = 1
T

This 1/T temperature dependence of the relaxation strength helps to identify a relaxation, since the 1/T temperature dependence is not common in the elastic constant for other physical processes.

CHAPTER 4.

EXPERIMENTAL RESULTS

The objective of this work was to determine whether there existed relaxations which were associated with the motion of hydrogen at low temperatures, and to explain the results with a model which would also be consistent with measurements of other properties of this and related systems.

Measurements were made of attenuation and velocity in niobium containing various concentrations of oxygen and hydrogen as a function of temperature, frequency, polarization of the ultrasonic wave, and hydrogen isotope. Measurement of the velocity could be done with greater sensitivity than measurement of attenuation, but the dependence of the attenuation on temperature made it more valuable in determining the characteristics of relaxations. The velocity could be measured with a relative accuracy of one part in 10^7, but the behavior of the velocity in the hydrogen free specimen was complicated by the superconducting transition and a strong temperature dependence. This made it difficult to accurately measure differences between the velocities of hydrogen charged and hydrogen free samples.

The attenuation could not be measured to as great an accuracy as the velocity, but the temperature dependence of the attenuation in the uncharged sample was much simpler. The superconducting contribution was predictable and could easily be accounted for. The attenuation of the normal metal was nearly independent of temperature through the range of interest. The contribution of hydrogen to the attenuation therefore was easier to determine.

The initial experiments were performed on Nb1 charged to a low concentration of hydrogen. At this time an accurate attenuation recorder was not available. The low concentration also indicated that the relaxation would be too small to be seen in the attenuation. For these reasons, only velocity measurements were performed originally.

The relaxation strength was larger than first expected, and with the improvement in accuracy of the available attenuation recorder, attenuation measurements were attempted. Hence, the later experiments, especially the ones with high concentrations of hydrogen, included both velocity and attenuation measurements, while the experiments with low concentrations of hydrogen occasionally included only velocity measurements.

The various concentrations of hydrogen and deuterium, along with the concentrations of trapping defects such as oxygen, nitrogen, or carbon for both samples are indicated in Table 3.

TABLE 3.

DEFECT CONCENTRATIONS

Sample	Trapping Concentration	Hydrogen Concentration	Isotope
Nb1	1000 ppm 0	160 ppm	H
		200 ppm	H
		2150 ppm	H
		200 ppm	D
		575 ppm	D
		1800 ppm	D
Nb2	200 ppm 0,N,C	700 ppm	H

1.0 Temperature Dependence of Background Velocity

Measurements were made of the velocity and attenuation in uncharged samples to determine the background behavior. The temperature dependence of the normal elastic constant at low temperatures contains both T^2 and T^4 terms,

$$\frac{\delta C}{C} = - \alpha T^2 - \beta T^4 \quad . \tag{4.1}$$

The coefficients α and β could be determined by fitting the above equation to the velocity data above the superconducting temperature, 9.1 K. The coefficients for the three modes are listed in Table 4.

TABLE 4.

T^2 and T^4 COEFFICIENTS

Elastic Constant	α	β
C_{11}	8.2×10^{-8}	7.6×10^{-10}
C_{44}	2.4×10^{-6}	2.1×10^{-10}
C'	4.4×10^{-7}	1.3×10^{-9}

2.0 Low Concentration Hydrogen Results

Measurements of the frequency change at 10 MHz of the C' mode versus temperature for Nb1, containing 1000 ppm oxygen, with and without 160 ppm of hydrogen are indicated in Figure 10. The relative change in the velocity is equal to the frequency change divided by the measuring frequency, 10 MHz, from Equation 2.4. The relative elastic constant change is equal to twice

Figure 10. The frequency change of the C' mode as a function of temperature. The upper curve represents data taken on a hydrogen free sample. The lower curve represents data taken on a sample charged with 160 ppm of hydrogen. The two curves have been drawn so that the difference between them decreases as 1/T at high temperature.

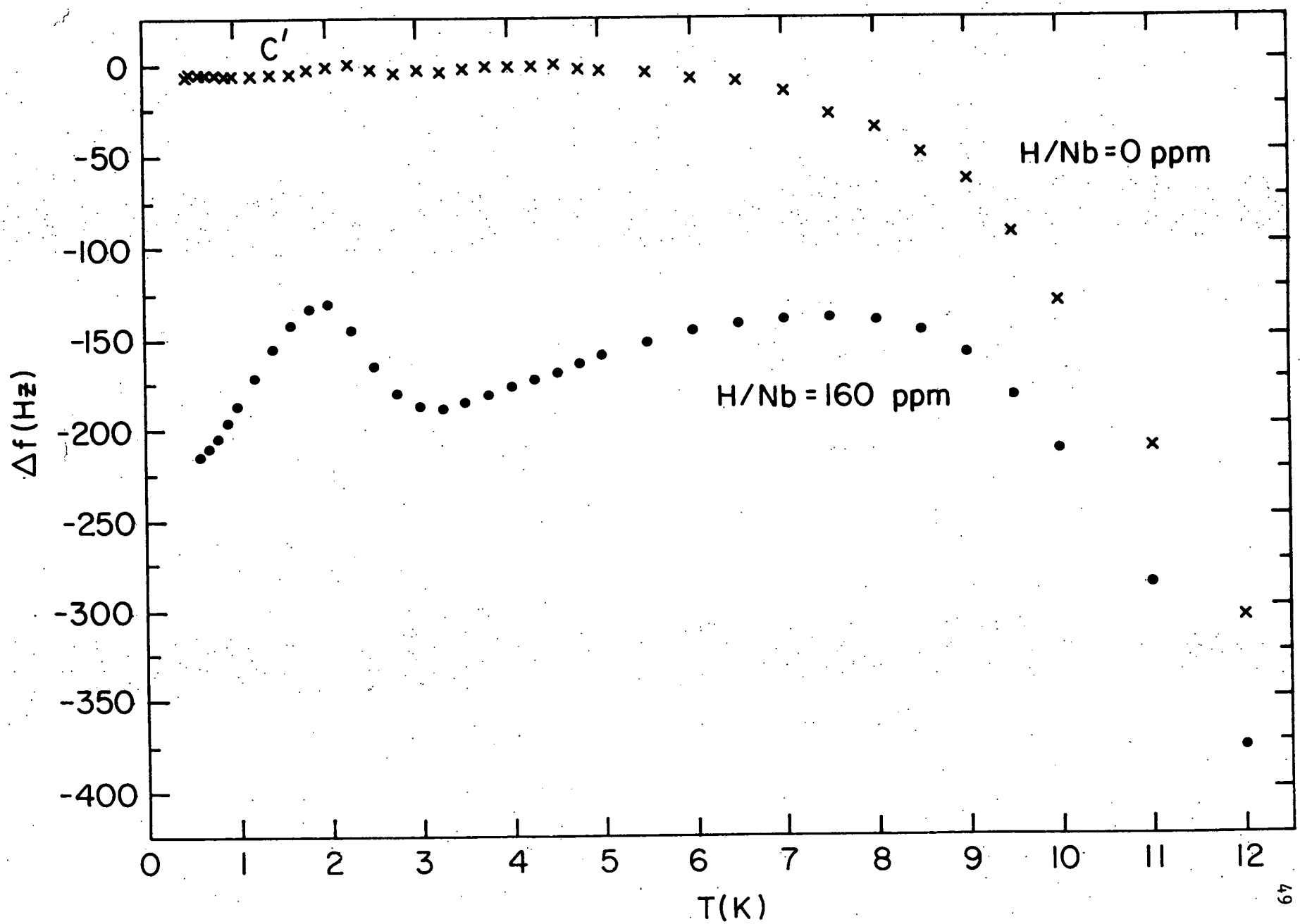
C'
H/Nb = 0 ppm
H/Nb = 160 ppm
Δf (Hz)
T(K)
0
-50
-100
-150
-200
-250
-300
-350
-400
0
1
2
3
4
5
6
7
8
9
10
11
12

the relative change in velocity, from Equation 2.5. The relative changes in both the velocity and elastic constant are therefore proportional to the changes in frequency. The upper curve represents the velocity change with no hydrogen and is characteristic of most metals. The curve is flat at low temperatures, approaching the vertical axis with zero slope. Above a few degrees the velocity decreases, with a discontinuity in slope at the superconducting transition temperature, 9.1 K. This is difficult to see in Figure 10 because of the small size of the superconducting contribution to C', but can be more easily seen later in the C_{44} mode. At higher temperatures, the velocity decreases rapidly, with the second and fourth powers of temperature.

The lower curve represents the velocity change when the sample was charged with 160 ppm of hydrogen. Since the relative accuracy of the velocity measurements is much greater than the absolute accuracy, the relative positions of the two curves is difficult to determine. These curves were positioned so as to coincide at the highest temperatures of measurement. For this case, it is seen that the charged curve falls below the uncharged curve, the velocity defect becoming greater with lower temperatures. Below 3 K the velocity increases until about 2 K, where it again starts to decrease.

This behavior is a strong indication of a relaxation when compared to the expected behavior as shown in Figure 9. Above 3 K, the velocity defect decreases monotonically. Below 2 K and 3 K, there is a dispersion in the velocity. The normal behavior for a relaxation is that the velocity at temperatures below the dispersion approaches the value in the absence of the relaxation. Here it is seen that the velocity instead begins to decrease below

2 K down to the lowest temperature, about 0.4 K. Possible reasons for this unusual behavior will be considered later.

To verify whether the effect seen is due to a relaxation, the decrement was also measured. The results are shown in Figure 11, along with the frequency defect from Figure 10. The upper curve represents the decrement change per unit concentration of hydrogen. The decrement peaks at the temperature where the velocity is undergoing dispersion, dropping off at higher and lower temperatures. The relaxation strengths predicted by each curve are similar, about 2×10^{-5}. This is exactly the behavior expected from a relaxation. There is also evidence of a much smaller peak in the decrement at about 6 K.

Measurements of the velocity for the C_{44} mode are shown in Figure 12. The behavior of this mode is markedly different from that of C'. Note the large superconducting effect which was not present in C'. Above 9 K, the velocity decreases with the second and fourth powers of temperature. Below this temperature the velocity also sharply decreases before levelling off, approaching the vertical axis with zero slope. This behavior is common in superconducting metals, as indicated by Alers (1966).

Notice that the addition of 160 ppm hydrogen produces changes in velocity of less than 1 ppm. This absence of a relaxation in the C_{44} mode is valuable for the interpretation of various models for the relaxation and indicates the usefulness of ultrasonic methods in determining symmetry properties of defects.

The third independent elastic constant is the bulk modulus, B. Measurements of the bulk modulus directly are not possible to this accuracy, but it is seen in Table 2 that the bulk modulus can be obtained from measurements of C' and C_{11}. Nowick and Berry (1972) indicate that no relaxation is expected

Figure 11. The decrement per unit concentration for H/Nb = 200 ppm and frequency change for H/Nb = 160 ppm as functions of temperature for the C' mode. The frequency change data represents the difference between the two curves in Figure 10.

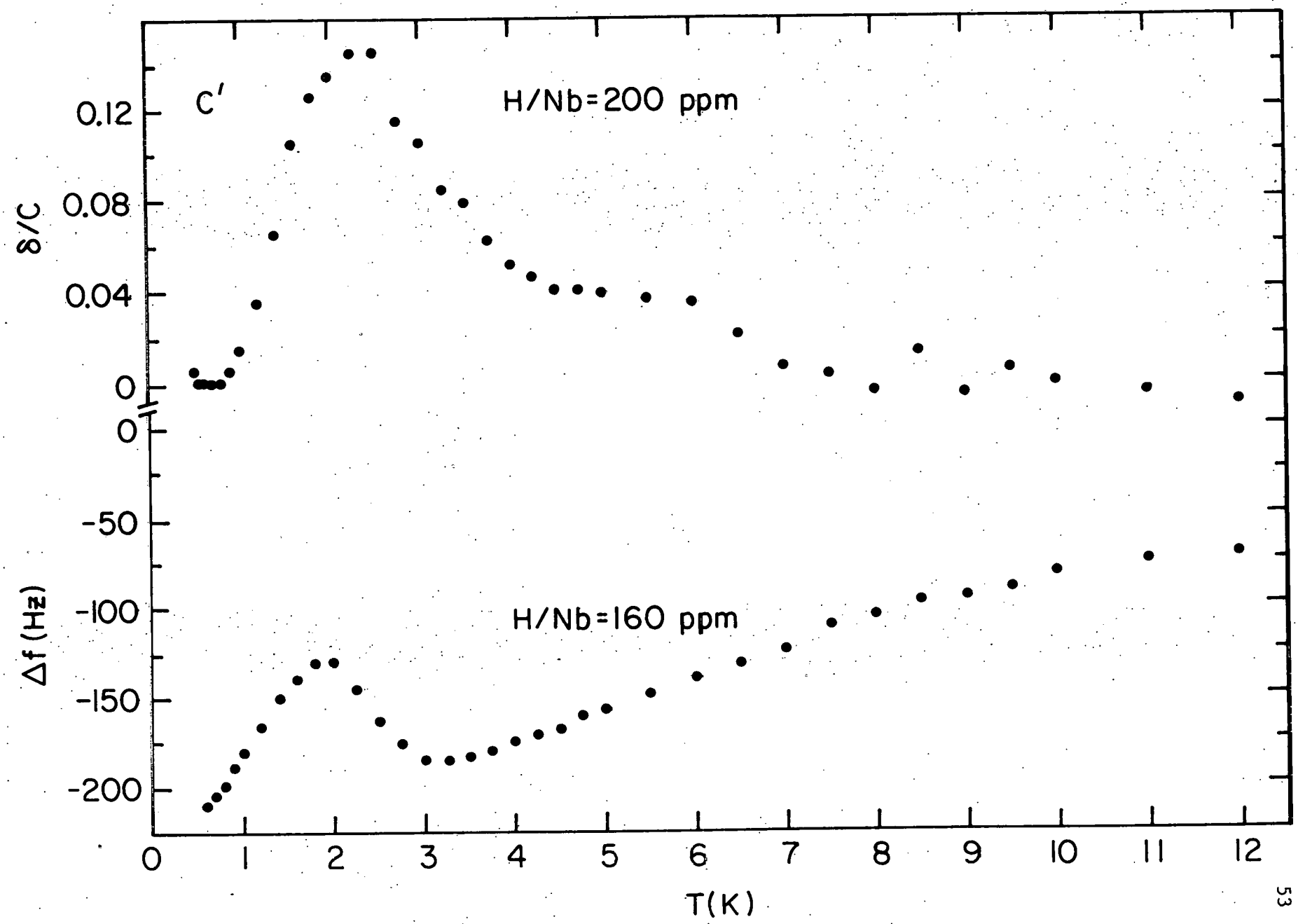
C'
H/Nb=200 ppm
H/Nb=160 ppm
δ/C
Δf (Hz)
T(K)
0.12
0.08
0.04
0
0
-50
-100
-150
-200
0
1
2
3
4
5
6
7
8
9
10
11
12

Figure 12. The frequency change of the C_{44} mode as a function of temperature for H/Nb = 0 and 160 ppm. The discontinuity in slope at 9 K is due to the superconducting transition.

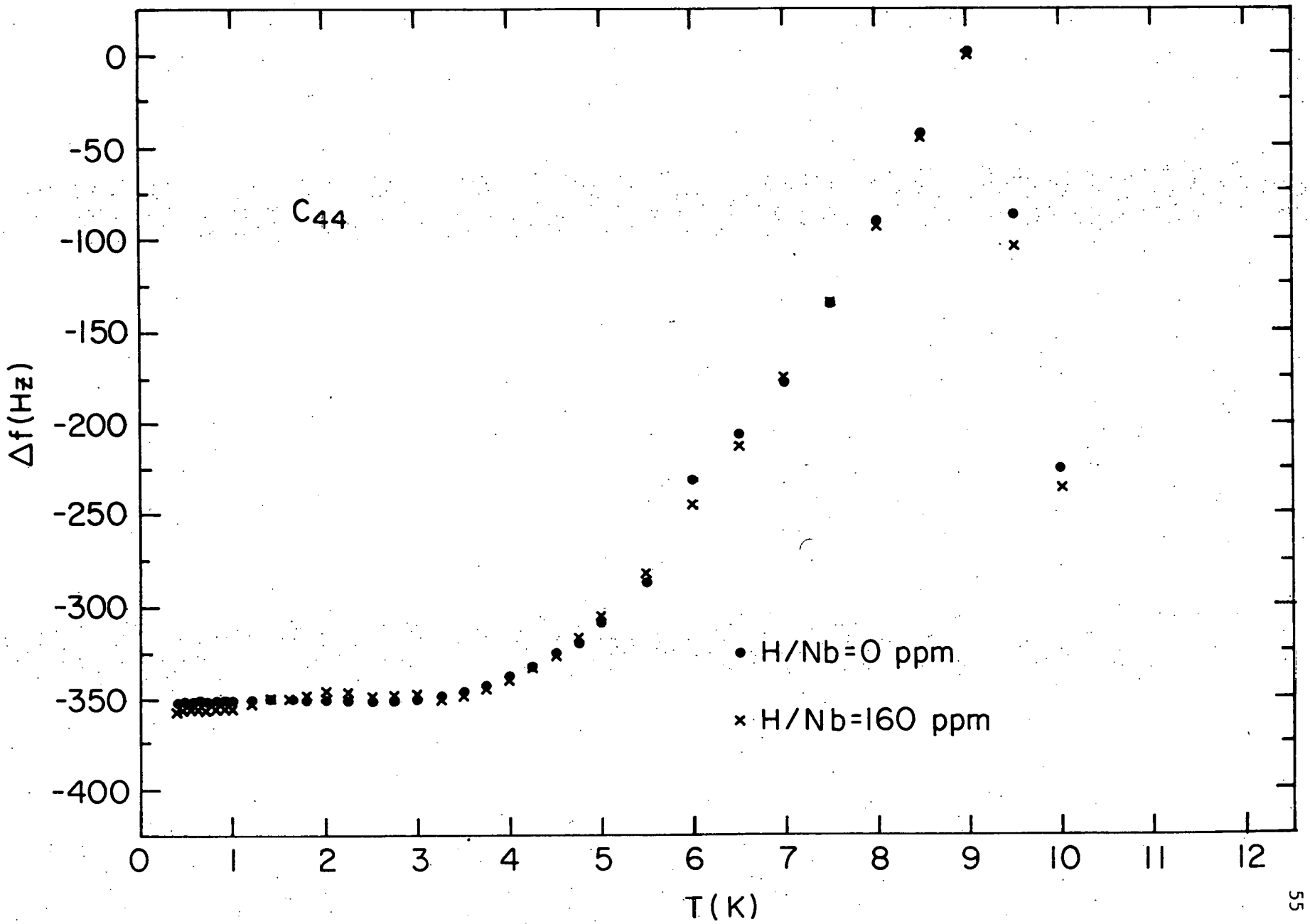
0
-50
-100
-150
-200
-250
-300
-350
-400
Δf(Hz)
C44
H/Nb=0 ppm
H/Nb=160 ppm
0
1
2
3
4
5
6
7
8
9
10
11
12
T(K)

in the bulk modulus for a defect which undergoes position changes without a change of the defect species. That is, a transition between symmetrically equivalent interstitial sites does not change the defect species, and so does not lead to a bulk modulus relaxation. A transition to an inequivalent site or a transition which changes the atomic identity (e.g., an H_2 defect which dissociates into separate H defects during a transition) can in general lead to a bulk modulus relaxation. These measurements at low concentration were not accurate enough to rule out a B relaxation, but later results were.

3.0 Low Concentration Deuterium Results

The sample Nb1 was also used for measurements of the isotope effect. The hydrogen was removed by vacuum annealling and 230 ppm of deuterium was introduced. The resulting velocity and decrement curves are shown in Figure 13. The velocity curve was very difficult to match to the uncharged curve, so the maximum velocity, occurring at 2 K, was used as the reference point for measuring changes.

The decrement peak is much broader than the peak caused by hydrogen, and occurs at higher temperature. The relaxation strength is also greater for deuterium by about a factor of 2 for comparable concentrations. The velocity decreases below 2 K as it does with hydrogen. Above 2 K the velocity also decreases, but the dispersion continues through the superconducting temperature. The width of the dispersion in temperature is reflected in the width of the decrement peak.

Measurements of C_{44} with deuterium charging indicate no relaxation as in the case of hydrogen. The increased relaxation strength of deuterium allows more accurate measurements of C_{11} and C', so that the bulk modulus can be calculated. If the bulk modulus change is zero, then

Figure 13. The decrement per unit concentration and the frequency change of the C' mode as functions of temperature for D/Nb = 230 ppm. The frequency change data is referenced to the frequency at 2 K.

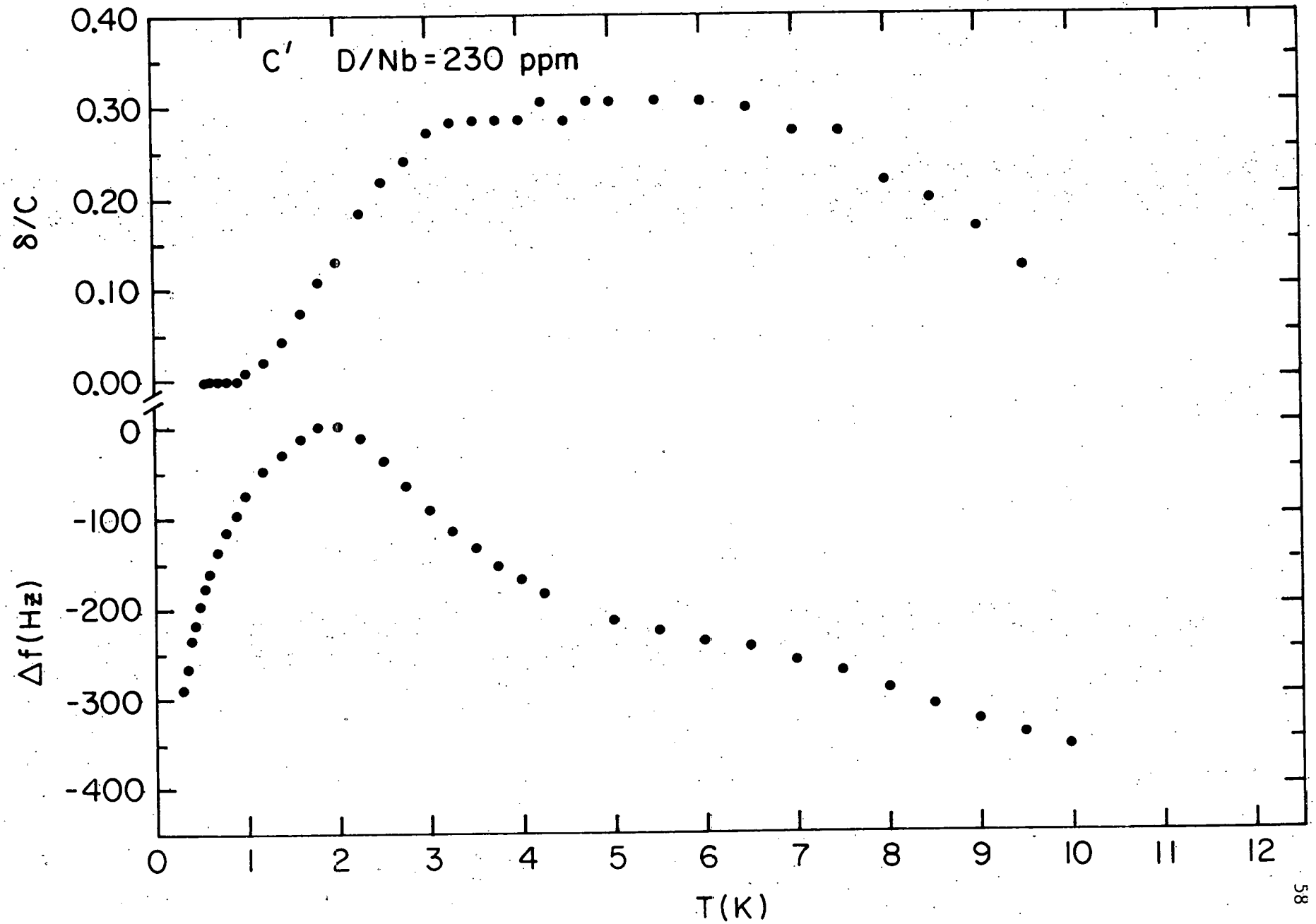
C′ D/Nb = 230 ppm
δ/C
Δf(Hz)
T(K)
0.40
0.30
0.20
0.10
0.00
0
-100
-200
-300
-400
0
1
2
3
4
5
6
7
8
9
10
11
12

$$\delta B = 3\delta C_{11} - 4\delta C' = 0 \qquad (4.2)$$

$$\delta C_{11}/C_{11} = 0.32\ \delta C'/C' \qquad (4.3)$$

so the change in C_{11} should be about one third the relative change in C'. The curves in Figure 14 show C' and C_{11} with a factor of three difference in scales, offset slightly to allow easier viewing. The bulk modulus is also shown, with no observable relaxation occurring above 1 K.

These results for low concentrations of hydrogen and deuterium indicate the presence of a relaxation occurring at 2.4 K at 10 MHz for hydrogen and at about 5 K at 10 MHz for deuterium. The deuterium relaxation has a larger strength for comparable concentrations and is much broader in temperature than for hydrogen. The relaxation strengths for both isotopes is small, typically 0.1 ppm for 1 ppm of defects.

4.0 High Concentration Hydrogen Results

In an effort to obtain better accuracy, the hydrogen concentration of Nb1 was increased to 2150 ppm. The corresponding decrement is shown in Figure 15, as a function of temperature for various frequencies from 10 to 150 MHz. Instead of a single peak in the decrement, two peaks are now seen. The low temperature peak occurs at the same temperature as the single peak at low hydrogen concentrations, but another peak appears at higher temperature. As a function of increasing frequency, the two peaks shift to higher temperatures and become broader.

An important feature of the low temperature peak is the temperature dependence of its relaxation strength. The normal behavior of the relaxation strength is to vary as the inverse of temperature (Equation 3.3). However,

Figure 14. The C', C_{11} and B mode frequency changes as functions of temperature for D/Nb = 575 ppm. The C' data are plotted against the upper left scale, while the B data are plotted against the lower left scale. The C_{11} data are plotted against the right scale. The C' and C_{11} scales are in a ratio of 3:1, showing that parallel C' and C_{11} curves give no B relaxation. The origins of the C' and C_{11} scales are shifted slightly to permit easier viewing.

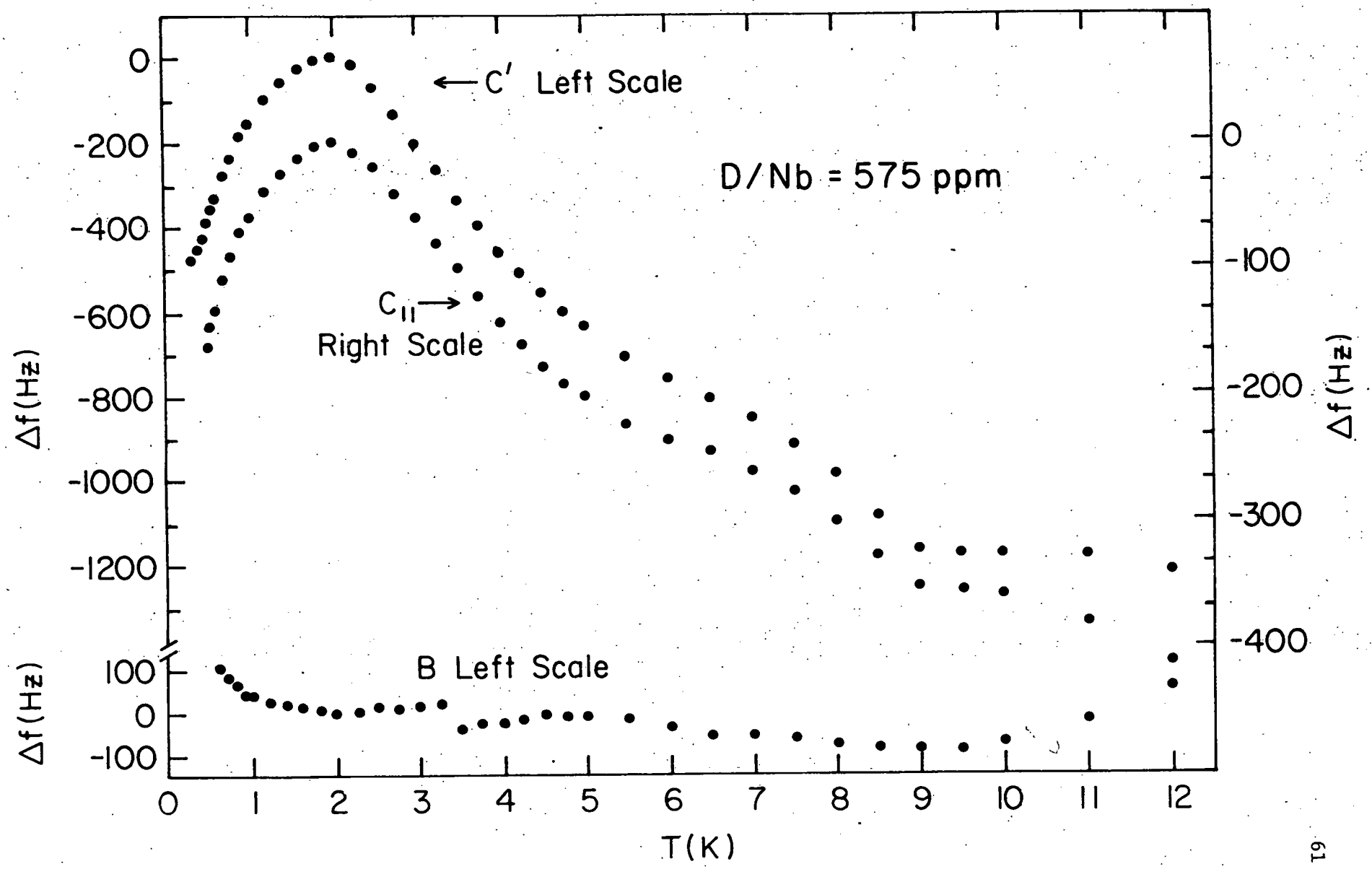
0
-200
-400
-600
-800
-1000
-1200
100
0
-100
Δf(Hz)
← C′ Left Scale
D/Nb = 575 ppm
C11 →
Right Scale
B Left Scale
0
-100
-200
-300
-400
Δf(Hz)
0 1 2 3 4 5 6 7 8 9 10 11 12
T(K)

Figure 15. The decrement of the C' mode per unit concentration as a function of temperature for H/Nb = 2150 ppm at 10, 30, 50, 70, and 150 MHz. The horizontal axis of each successive curve has been displaced upward by 0.15 along the vertical axis to permit easier viewing.

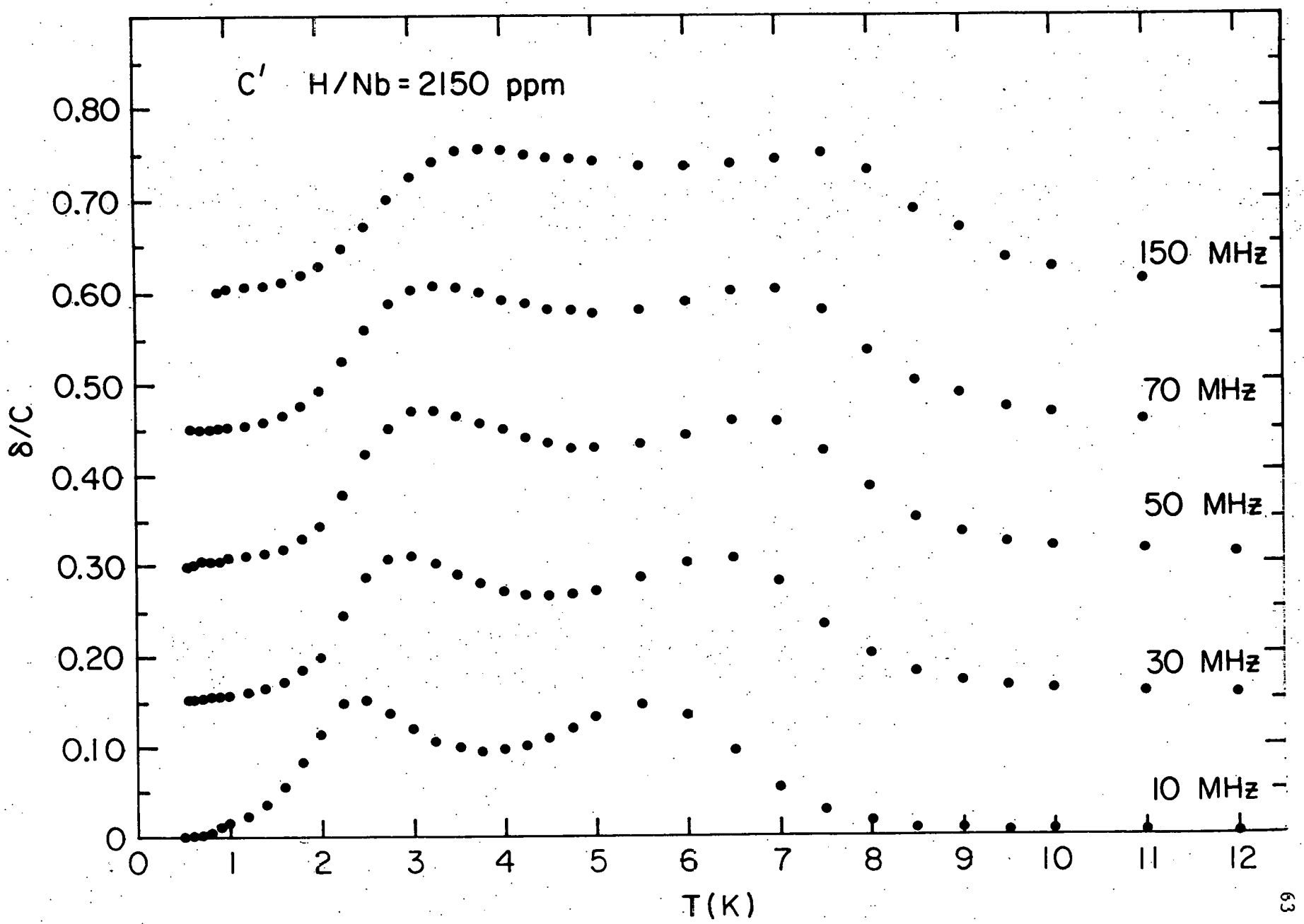
C′ H/Nb = 2150 ppm
0.80
0.70
0.60
0.50
0.40
0.30
0.20
0.10
0
δ/C
0
1
2
3
4
5
6
7
8
9
10
11
12
T(K)
150 MHz
70 MHz
50 MHz
30 MHz
10 MHz

the peak heights of the low temperature relaxation in Figure 15 do not vary much while the peak position changes in temperature by 50%. This unusual behavior of the relaxation strength will be considered in the discussion of the theoretical models.

If an Arrhenius dependence of transition time with temperature is assumed as in Equation 3.4, then the activation energies of both peaks can be calculated. The low temperature peak has an activation energy of 1.8 meV while that of the high temperature peak is about 4 meV.

The appearance of the new peak can be seen in Figure 16. The vertical axis represents decrement per unit concentration. The curves are measurements taken with hydrogen concentrations of 200 and 2150 ppm. The two curves overlap very well around the lower temperature peak at 2.4 K, indicating that the peak is due to a relaxation whose strength varies linearly with concentration. The high temperature peak is very different. The low concentration curve exhibits only a slight excess decrement at 5.5 K, whereas the high concentration curve has a high temperature peak which is equal in size to the low temperature peak. This suggests that the defect which gives rise to the high temperature peak has a nonlinear dependence on the hydrogen concentration. A likely candidate for the defect type which gives rise to the high temperature relaxation would be a hydrogen atom cluster, where two or more hydrogen atoms combine to form a single defect. The concentration of clusters containing n atoms, C_n, is easily derived in terms of the hydrogen concentration:

$$C_n = \beta\, C_H^n \exp\,(B/kT) \qquad (4.4)$$

where C_H is the total hydrogen concentration, β is a geometric constant, and

Figure 16. The decrement of the C' mode per unit concentration as a function of temperature for H/Nb = 200 and 2150 ppm. The low temperature peaks match, indicating a linear concentration dependence. The high temperature peak has a concentration dependence which is stronger than linear.

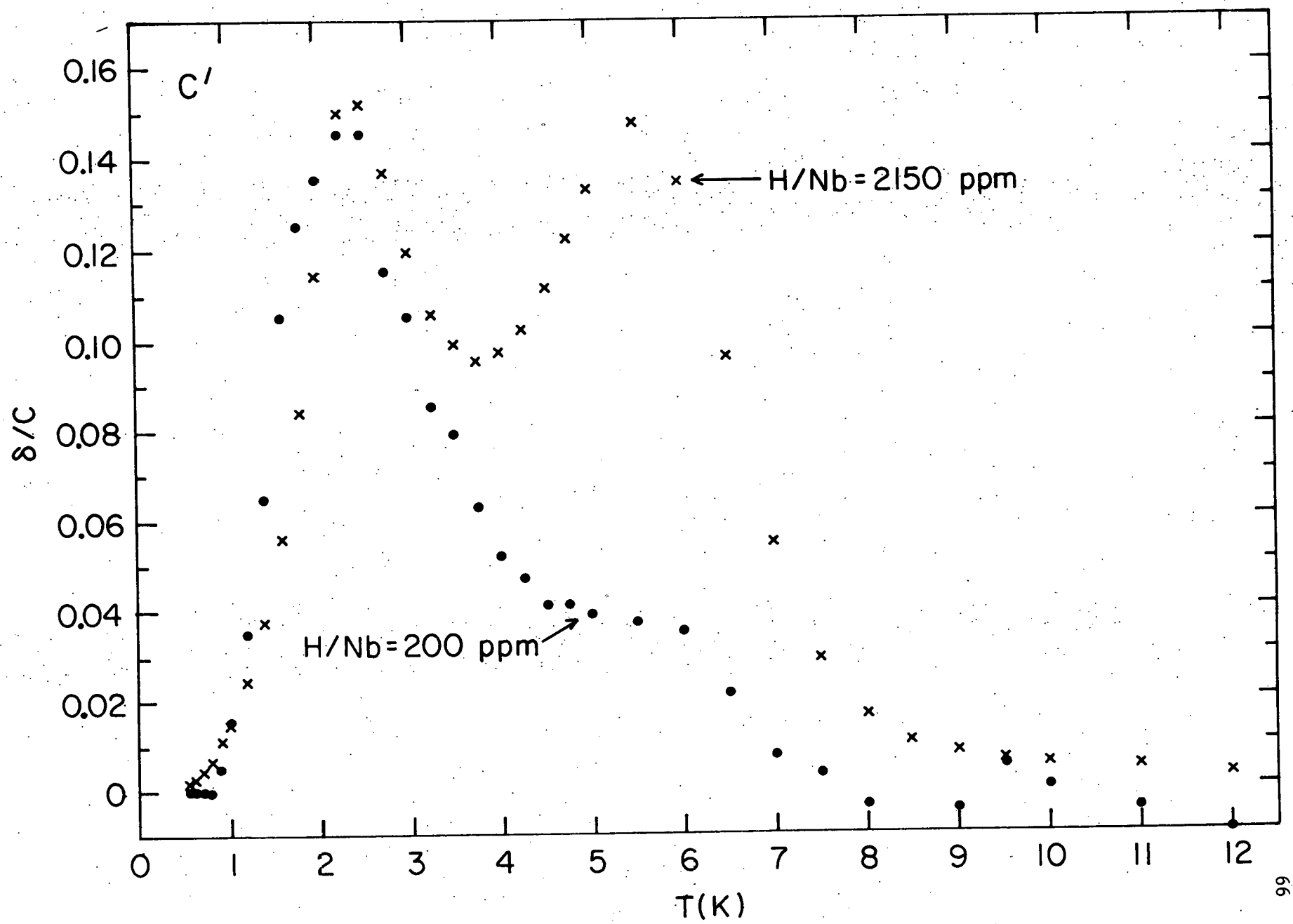
C'
0.16
0.14
0.12
0.10
0.08
0.06
0.04
0.02
0
δ/C
H/Nb = 2150 ppm
H/Nb = 200 ppm
0
1
2
3
4
5
6
7
8
9
10
11
12
T(K)

B is the binding enthalpy. This equation is valid as long as C_n is much less than the total hydrogen concentration. At a constant temperature, the concentration of defects containing n hydrogen atoms is proportional to the nth power of hydrogen concentration. Using the two concentrations for which data is available, a value of 1.9 is derived for n. This indicates that the most likely candidate for the high temperature relaxation is a defect consisting of a hydrogen pair. No information is available to determine whether the pair is also associated with an oxygen atom, or whether it exists as an isolated defect.

A comparison of the results for the C' and C_{44} modes can be seen in Figure 17. Decrement per unit hydrogen concentration versus temperature is plotted for C' and C_{44} modes for a hydrogen concentration of 2150 ppm. Background decrement for both curves has already been subtracted. The size of the C' relaxation can easily be seen. The maximum decrement is equal to $\pi/2$ times the relaxation strength (Equation 3.1), which indicates a relaxation strength per unit concentration of about 0.1 at 2.4 K. The C_{44} curve gives no evidence of a relaxation. The accuracy of the data indicates that the upper limit on the relaxation strength of the C_{44} mode is thirty times less than the relaxation strength of the C' mode. This would give a maximum relaxation strength per unit concentration of 0.003 for the C_{44} mode.

The velocity of the C' mode was also measured with the higher concentration of hydrogen. The results are shown in Figure 18. The correspondence between the velocity and decrement can be seen by comparing with Figure 17. The two dispersions in the velocity, centered at 2.5 K and 5.5 K, agree with peaks which occur in the decrement. There also exists the drop in velocity below 2 K which was seen at lower hydrogen concentration, but which does not

Figure 17. The decrement of the C' and C_{44} modes per unit concentration as functions of temperature for H/Nb = 2150 ppm. Two relaxation peaks appear in the C' mode, while none occur in the C_{44} mode.

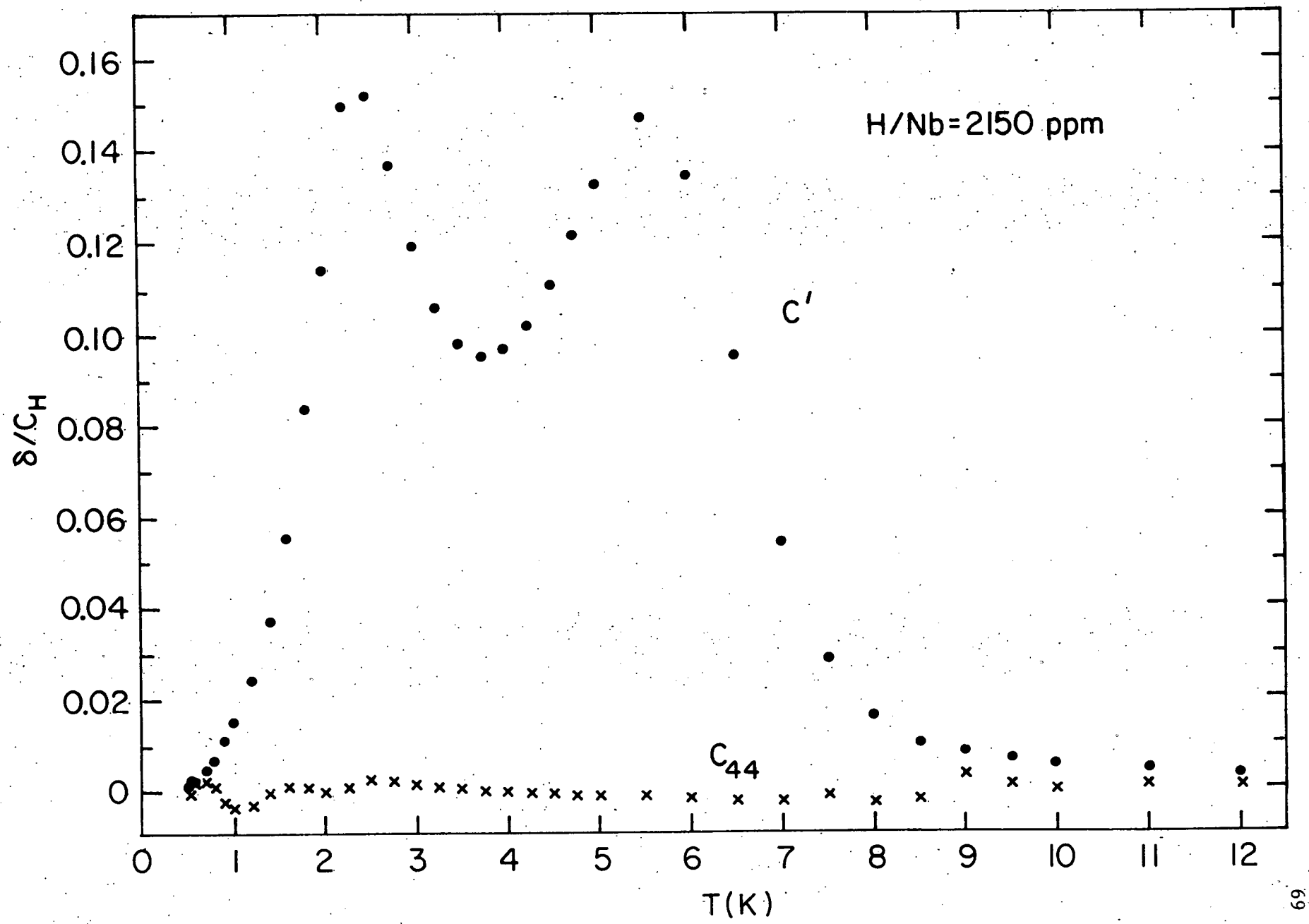
H/Nb=2150 ppm
C'
C44
δ/CH
T(K)
0.16
0.14
0.12
0.10
0.08
0.06
0.04
0.02
0
0
1
2
3
4
5
6
7
8
9
10
11
12

Figure 18. The frequency change of the C' mode as a function of temperature for H/Nb = 2150 ppm. The data points are indicated by the x's. Two dispersions can be seen, at 2.5 and 5.5 K. The solid curve will be discussed in terms of a theoretical model in Chapter 6.

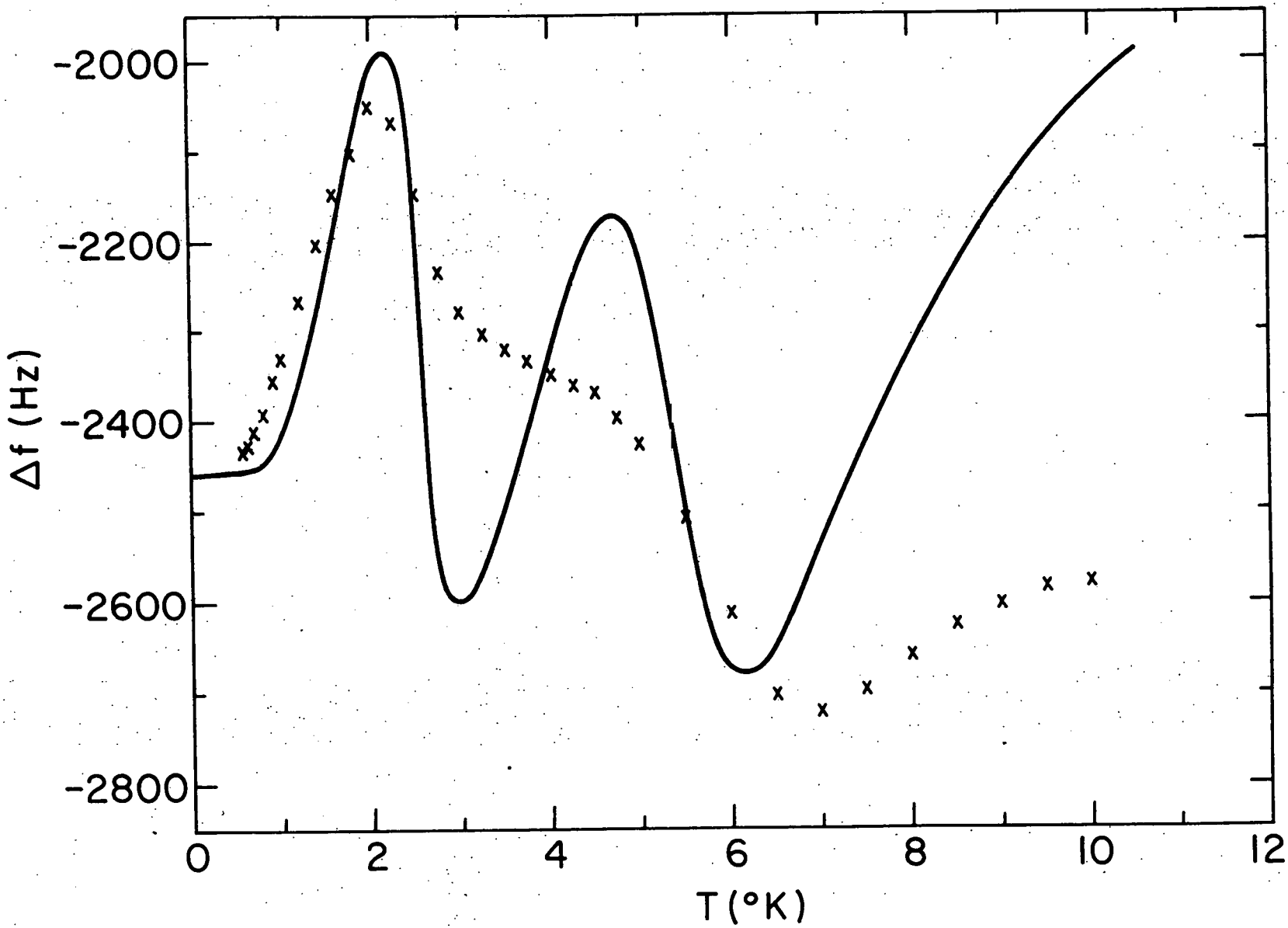
-2000
-2200
-2400
-2600
-2800
Δf (Hz)
0
2
4
6
8
10
12
T(°K)

have a corresponding effect upon the decrement. The solid line drawn in Figure 18 will be considered in the discussion of the theoretical models.

5.0 High Concentration Deuterium Results

Sample Nb1 was vacuum annealled to remove any hydrogen, and then was charged with 1800 ppm of deuterium. In Figure 19 are plotted the results of decrement measurements of the C' mode at 3 and 9 MHz. Measurements were attempted at 30 MHz and higher, but the results were such that subtraction of the background decrement was not possible. The decrement curves contain some similarities to the corresponding hydrogen results. Two peaks are observable, especially in the 3 MHz data. A low temperature peak appears at 4.75 K at 3 MHz with a high temperature peak at about 8.5 K. The broadness of the peaks in temperature and the inability to subtract the background decrement at higher frequencies makes it impossible to calculate a possible activation energy. This subject will be dealt with in the discussion of theoretical models.

The comparison of C' and C_{44} mode results are shown in Figure 20. Here, as in the case of hydrogen, no relaxation is seen in C_{44}, with a relaxation in C' which has a larger relaxation strength than the C' relaxation with hydrogen.

The velocity of the C' mode with the high concentration of deuterium is indicated in Figure 21. In contrast to the hydrogen velocity curve where two distinct dispersions were seen, there appears to be a single broad dispersion due to deuterium. Upon close examination, it can be seen that one dispersion occurs between 2.5 K and 5 K. Above 5 K the slope of the velocity curve appears to be decreasing before increasing sharply again around 8 K.

Figure 19. The decrement of the C' mode per unit concentration as a function of temperature for D/Nb = 1800 ppm at 3 and 9 MHz.

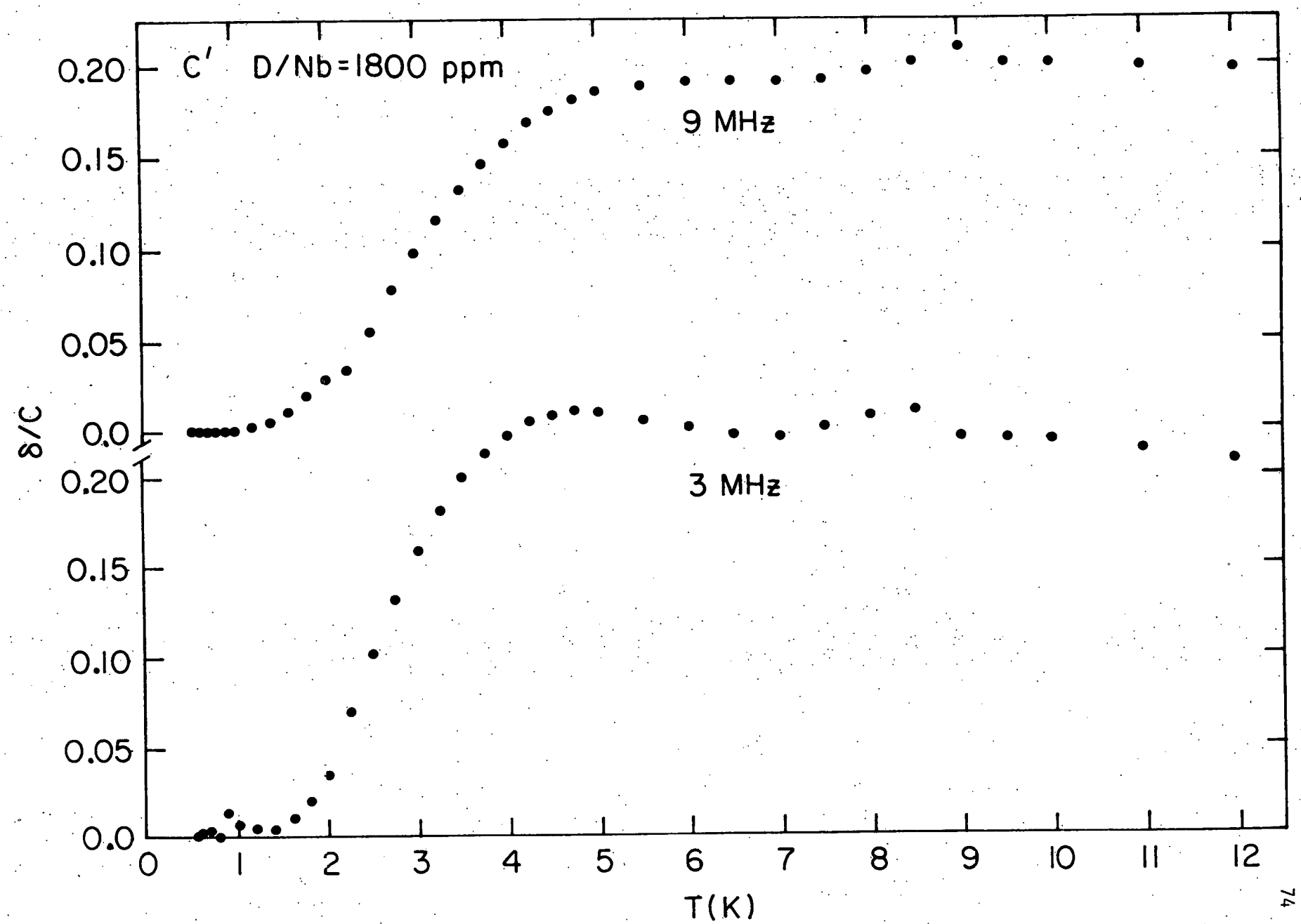
C′ D/Nb=1800 ppm
9 MHz
3 MHz
δ/C
0.20
0.15
0.10
0.05
0.0
0
1
2
3
4
5
6
7
8
9
10
11
12
T(K)

Figure 20. The decrement of the C' and C_{44} modes per unit concentration as functions of temperature for D/Nb = 1800 ppm. Two relaxations appear in the C' mode, while none occur in the C_{44} mode.

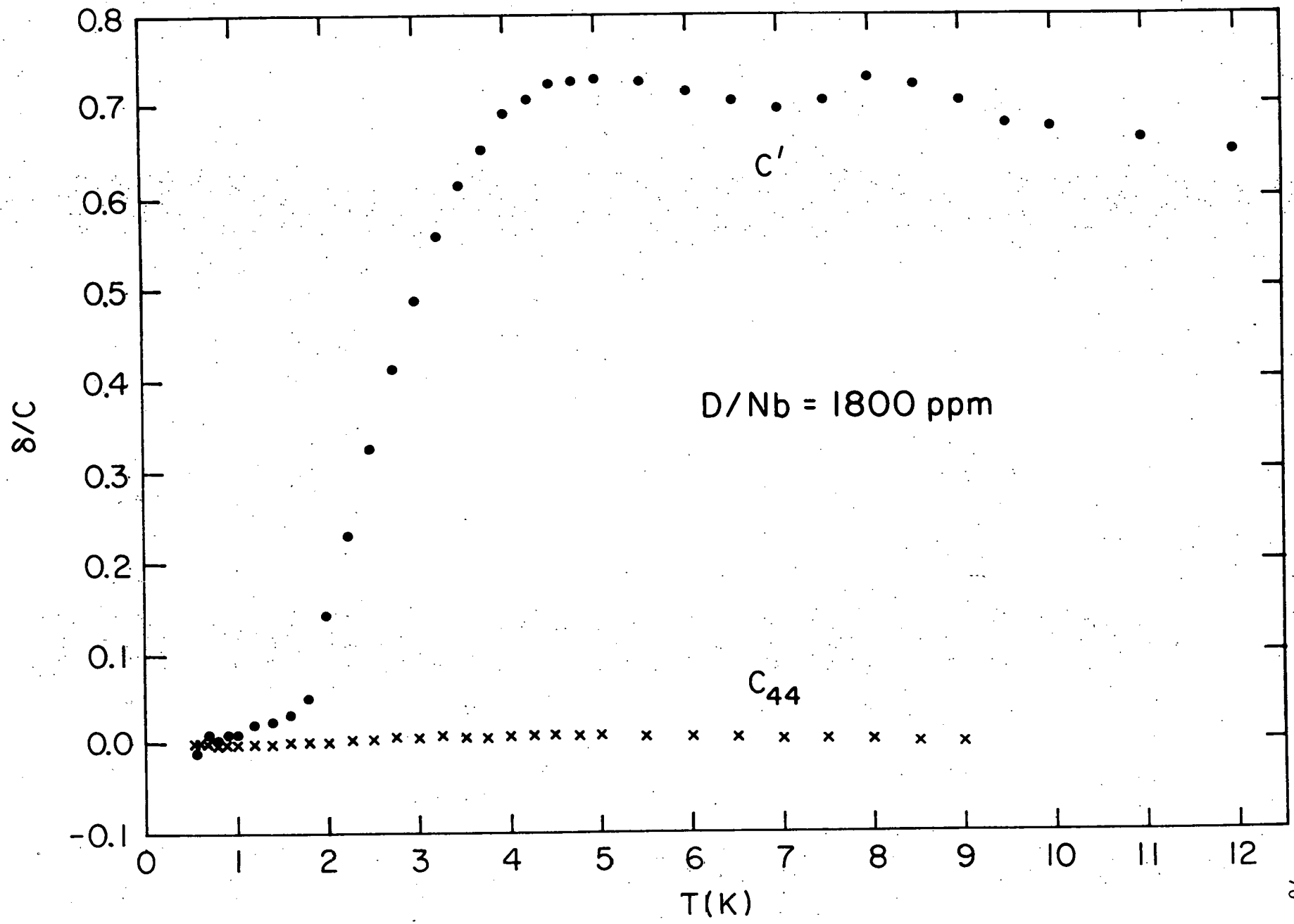
0.8
0.7
0.6
0.5
0.4
0.3
0.2
0.1
0.0
-0.1
δ/C
C′
D/Nb = 1800 ppm
C44
0
1
2
3
4
5
6
7
8
9
10
11
12
T(K)

Figure 21. The frequency change of the C' mode as a function of temperature for D/Nb = 1800 ppm.

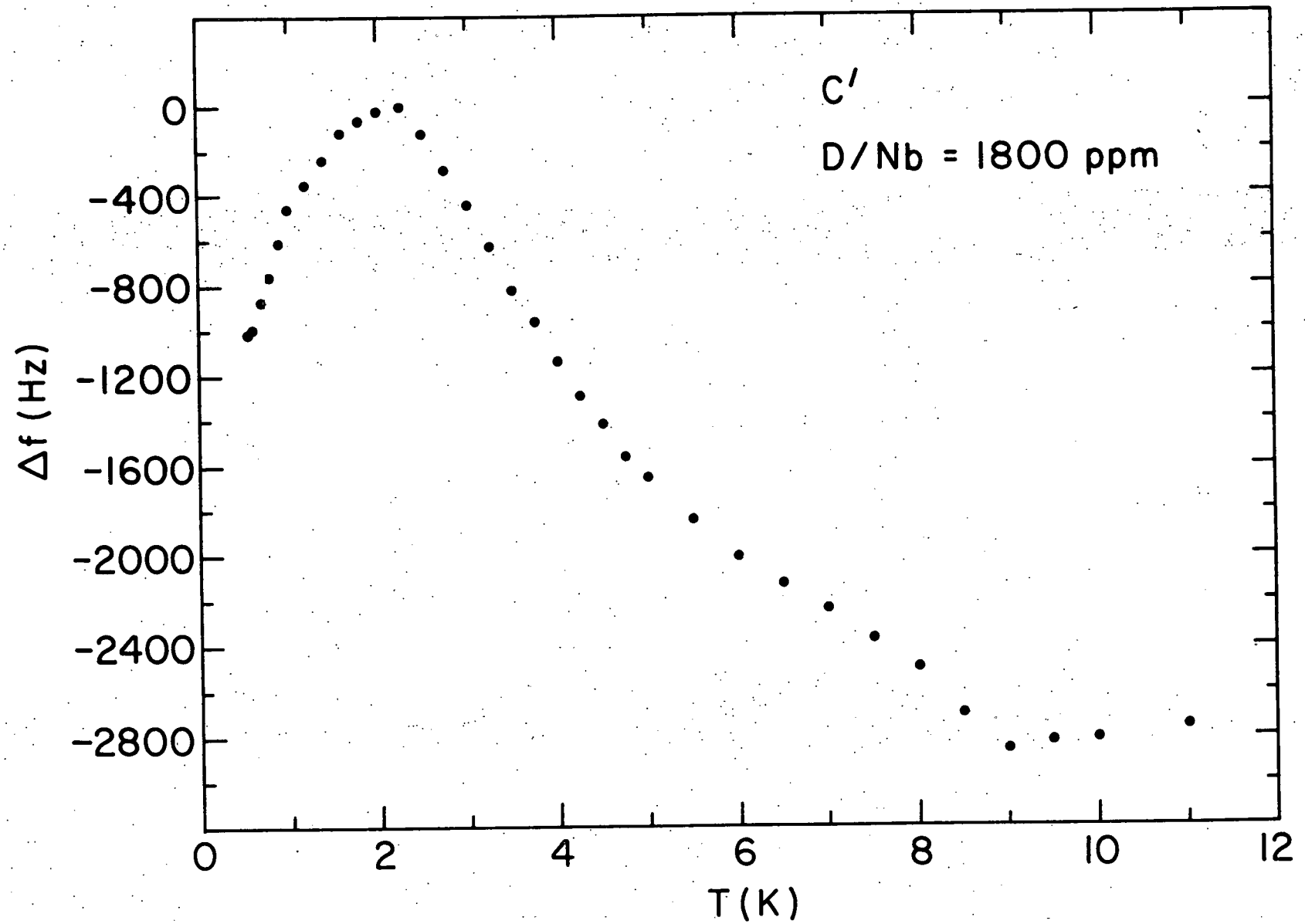
C′
D/Nb = 1800 ppm
0
-400
-800
-1200
-1600
-2000
-2400
-2800
Δf (Hz)
0
2
4
6
8
10
12
T(K)

These dispersions correspond to the positions of the peaks in the decrement. Just as the broadness of the decrement peaks makes it difficult to separate them, the broadness of the dispersions also makes it difficult to determine where each dispersion occurs. The discontinuity in slope between 9 and 9.5 K is due to the superconducting effect, and makes the behavior of the velocity curve above 9 K difficult to interpret. As in all the other velocity measurements, there is a decrease in the velocity below 2 K with no corresponding decrement effect.

6.0 The Effect of Cooling Rate

In the process of data reduction, it was noticed that the relaxation strength of various modes would vary by as much as 50% between seemingly identical experiments. It was noted in Equation 3.3 that the relaxation strength is proportional to concentration. If the concentration varied from experiment to experiment, this would explain the anomaly. It is doubtful that the total concentration of hydrogen and deuterium would vary at room temperature by escape from the sample. Faber and Schultz (1972) showed that niobium forms a very durable surface oxide at room temperature which is impervious to hydrogen. Secondly, comparable concentrations of hydrogen were usually calculated from both charging and discharging data, indicating no change in concentration between those times.

The possibility of a variation of the amount of hydrogen in solution was considered previously by Sellers, Anderson, and Birnbaum (1974). Below 200 K, hydrogen precipitates into beta phase niobium hydride which presumably does not contribute to heat capacity or ultrasonic effects. The binding energy of hydrogen to oxygen was measured by Mattas and Birnbaum (1975) at

about 0.1 eV. This would suggest that hydrogen can dissociate from oxygen down to at least nitrogen temperature, 77 K. Therefore the amount of hydrogen which is associated with oxygen would depend upon the cooling rate between 200 K and about 77 K.

To test this hypothesis, the following experiment was attempted: The C' decrement of 2150 ppm hydrogen was measured after cooling at the normal rate, about 1 K/minute. The relaxation strength measured was typical of this type of experiment, as shown by the open circles of Figure 22. The sample was warmed to 150 K for one hour to allow hydrogen to dissociate and precipitate. It was then cooled rapidly, about 10 K/minute, to helium temperatures. The decrement was then a factor of two lower as shown by the squares of Figure 22. The sample was then warmed to about 230 K for one hour. Since this was above the precipitation temperature, some hydrogen would be expected to redissolve. The sample was again cooled rapidly, about 10 K/minute, and the decrement, represented by the triangles of Figure 22, had regained most of its former magnitude. These results are interpreted as an indication that the concentration of oxygen-hydrogen pairs is variable, and depends upon the cooling rate. Since the concentration of hydrogen which remains paired to oxygen and therefore contributes to the relaxation is not known, it is not possible to use Equation 3.3 to derive the lambda tensor elements which characterize the elastic interaction.

7.0 Effect of Bias Stress

The inclusion of a bellows in the cryostat insert allowed the investigation of the effects of bias stress upon the relaxation. The sample Nb1, with a

Figure 22. The decrement of the C' mode per unit concentration as a function of temperature for H/Nb = 2150 ppm after various quenches.

○ - 1 K/min from room temperature

□ - Warmed to 150 K, followed by quench to helium temperature

△ - Warmed to 250 K, followed by quench to helium temperature.

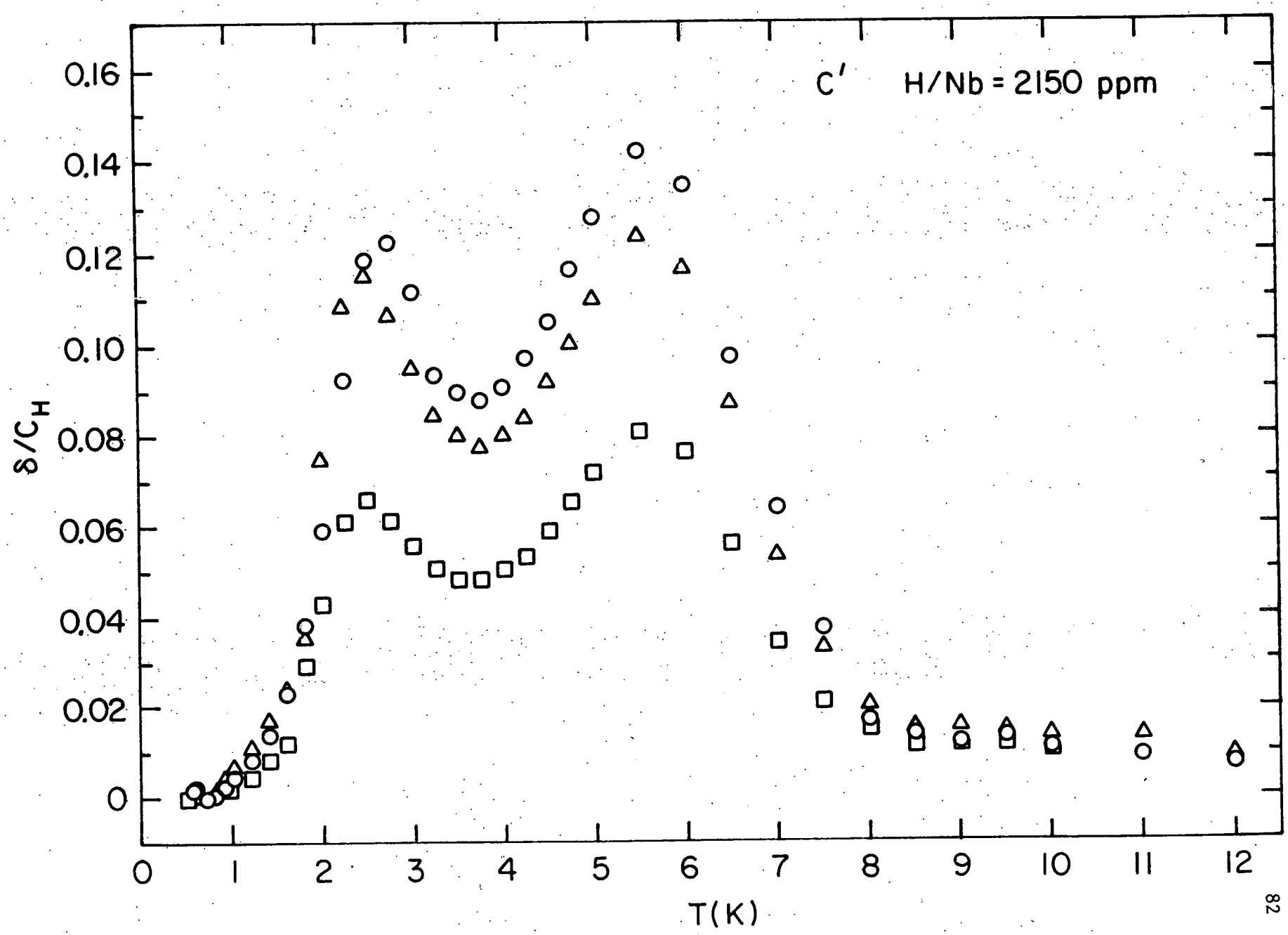
C′
H/Nb = 2150 ppm
δ/C_H
0.16
0.14
0.12
0.10
0.08
0.06
0.04
0.02
0
0
1
2
3
4
5
6
7
8
9
10
11
12
T(K)

hydrogen concentration of 160 ppm, was used to measure the velocity of the C_{11} mode. Application of the bias stress was done in several ways. A stress of 7 bars, corresponding to a strain of about 3×10^{-6}, was applied at room temperature and was maintained while cooling to helium temperature. The sample was warmed to 115 K, where the stress was increased to 27 bars while cooling to helium temperature. The sample was warmed to 77 K, the bias stress was removed, and the sample was again cooled to helium temperature. No change in the relaxation was detected due to any of the applications of bias stress.

The binding of the hydrogen to an oxygen interstitial would be expected to introduce local strains of several percent. The application of additional strains three orders of magnitude smaller due to the external bias stress would not be expected to produce large perturbations of the system. For this reason, the lack of any effect of bias stress would be expected. The application of bias stresses which are comparable to those produced by the oxygen was not possible, so no further bias stress experiments were attempted.

8.0 Effect of Oxygen Concentration

To determine the effect of the oxygen concentration upon the relaxation, the second sample, Nb2, was charged with hydrogen to a concentration of about 700 ppm. Impurity analysis showed a combined concentration of oxygen, carbon and nitrogen to be about 200 ppm. The objective of using smaller concentrations of these impurities was to reduce the internal strains produced by them, and to investigate the concentration dependence of the relaxation strength. The result can be seen in Figure 23 for the C' mode at 10 and 30 MHz, compared to the previous results at higher oxygen concentration.

Figure 23. The decrement of the C' mode per unit concentration as a function of temperature for two trap concentrations. The solid line under the low temperature 10 MHz peak represents the expected peak shape for a relaxation with no broadening and with the observed activation energy.

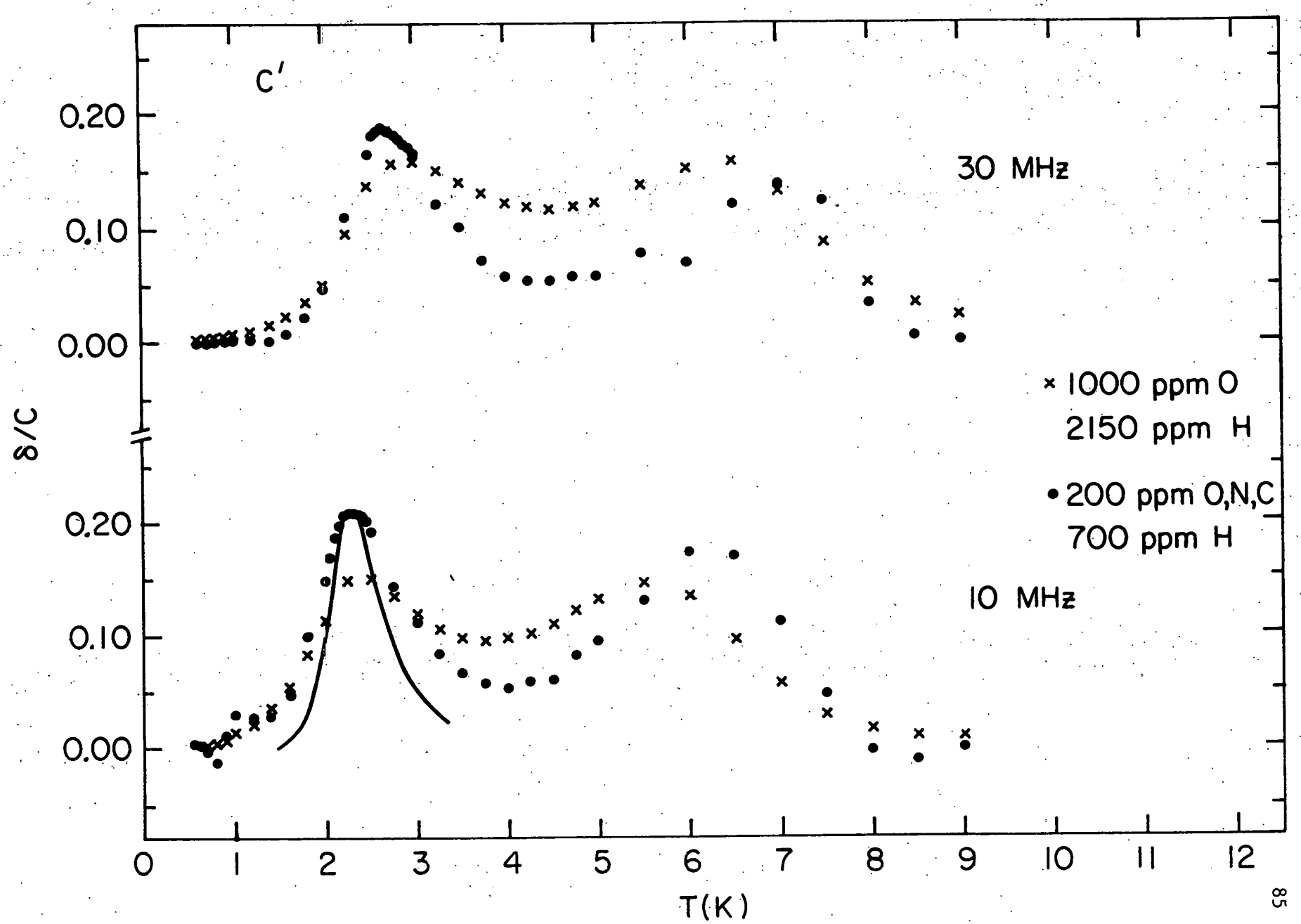
C′
0.20
0.10
0.00
30 MHz
× 1000 ppm O
2150 ppm H
• 200 ppm O,N,C
700 ppm H
10 MHz
δ/C
0
1
2
3
4
5
6
7
8
9
10
11
12
T(K)

The most striking difference is the sharpening of the relaxation peaks at lower concentration of oxygen. The width of the peaks is narrower in temperature and they peak at higher values of decrement. This is consistent with a reduction in the width of the distribution in relaxation time. For comparison, the solid line in the lower curve near the 2.4 K peak indicates the expected result for a single relaxation with no broadening and with an activation energy equal to that observed for the low temperature relaxation. The peak corresponding to the low trapping concentration conforms much more closely to the line than the peak for the higher trapping concentration.

The high temperature peaks also appear to be shifted to higher temperature with lower concentration of oxygen. Most of this shift is explained by the width of the peaks. In the high oxygen concentration curves, the low temperature peak is broad enough to overlap the high temperature peak. The falling tail of the low temperature peak appears to shift the high temperature peak to lower temperatures. Decreasing the oxygen concentration sharpens the peaks, reducing the overlap, and shifting the high temperature peaks towards higher temperatures.

9.0 Summary of Experimental Results

The most important experimental results, which will be used in the interpretation, are:

1) An anelastic relaxation due to hydrogen-oxygen complexes exists in niobium.
2) The relaxation is absent in the C_{44} and bulk modulus modes over an order of magnitude in hydrogen concentration.
3) The relaxation is present in the C' mode at 2.4 K at 10 MHz for hydrogen, with an apparent activation energy of about 1.8 meV.

The deuterium relaxation has a frequency of 3 MHz at 4.75 K with an undetermined activation energy. In addition, there exists a decrease in the elastic constant without a corresponding peak in the attenuation below 2 K.

4) A second relaxation appears at higher hydrogen concentrations in the C' mode. The concentration dependence of the relaxation strength indicates a hydrogen pair defect, either isolated or possibly bound to an oxygen. The relaxation appears at 5.5 K at 10 MHz with an activation energy of 4 meV for hydrogen and at 8 K at 3 MHz for deuterium.

5) The deuterium relaxation occurs at a higher temperature, the peak is wider in temperature, and it has a larger relaxation strength than the hydrogen relaxation. At the highest frequencies measured, the deuterium decrement does not decrease with increasing temperature above the peak temperature, but remains elevated.

6) The low temperature relaxation is too broad in temperature to be due to a single relaxation time. The broadening is decreased by decreasing the trapping defect concentration.

7) The dependence of hydrogen concentration on cooling rate makes the concentration determination difficult. The relaxation strength remains the product of concentration and lambda tensor.

8) The relaxation strength of the hydrogen relaxation does not follow a normal 1/T dependence, but begins to decrease at the lowest temperatures.

The effects which are unusual for a relaxation, and which produce the most severe test for a model are the broadening of the deuterium peaks

relative to the hydrogen peaks, the low temperature decrease in the elastic constant without the corresponding peak in the attenuation, and the decrease of the hydrogen relaxation strength at low temperatures.

Any model for the behavior of hydrogen at low temperatures must be consistent with these results. The next two chapters will include an explanation of these results in terms of a delocalized bound hydrogen model.

CHAPTER 5.

A DELOCALIZED BOUND HYDROGEN MODEL

The delocalized unbound model of Birnbaum and Flynn (1976) provided an excellent description of the contribution of hydrogen and deuterium interstitials to the heat capacity of niobium. However, no allowance was made for the binding of hydrogen to other interstitials to prevent precipitation. Since no appreciable quantities of free hydrogen are present at the temperatures under consideration, and since trapping interstitials produce internal strains which affect the properties of the bound hydrogen, modifications are required to be made to the delocalized model to account for trapping.

The localized bound model of Morkel, Wipf and Neumaier (1978) includes the effect of hydrogen trapping. However, the lack of a detailed, quantitative calculation of the interaction makes difficult the comparison to experimental data. The properties of the localized bound model are very dependent upon interactions with other neighboring defects, and so should be sensitive to trapping concentration. As this sensitive concentration dependence is not seen in the heat capacity (Morkel, Wipf and Neumaier 1978) or in the elastic constants, it would be difficult to conform this model to the experimental results. Other comparisons which indicate inconsistencies of this model with the experimental results will be discussed in the next chapter.

The delocalized model, in the form given by Birnbaum and Flynn, does not provide explicit expressions for the strain interactions. These can be included by considering a hindered rotator calculation, which while not giving analytical solutions, does allow more detailed numerical calculation

of the strain interaction than can be done with the matrix method used by Birnbaum and Flynn.

1.0 The Hindered Rotator

Examination of the eight interstitial sites which make up the delocalized model of Birnbaum and Flynn (Figure 3(a)), suggests a ring structure. The sites are coplanar and are approximately equidistant from the octahedral site. It would be reasonable to assume that the essential characteristics would be contained in a hindered rotator model. The hindered rotator consists of a single particle constrained to move in a plane in a ring of constant radius. The only coordinate of motion in the cylindrical coordinate system is the angle ϕ. The localization of the wave function into the triangular and tetrahedral sites is accomplished by using a barrier potential

$$V = \frac{B}{2} (1 - \cos 8\phi) \quad . \tag{5.1}$$

This potential contains eight minima, with the first minima at $\phi = 0$, and will set the bottom of each minima at $V = 0$.

The offset between triangular and tetrahedral sites, ε, can be included by adding another term

$$V = \frac{\varepsilon}{2} (1 - \cos 4\phi) \quad . \tag{5.2}$$

Strains can be included by adding terms such as

$$V_{\varepsilon'} = \alpha_1 \varepsilon' \cos 2\phi \quad , \qquad V_{\varepsilon_{44}} = \alpha_2 \varepsilon_{44} \sin 2\phi \quad . \tag{5.3}$$

In cubic crystals, the strain C' represents a symmetric distortion of the lattice in which a [100] direction is compressed, while another [100] direction is extended the same amount. The strain C_{44} represents a symmetric distortion of the lattice in which a [110] direction is compressed, while the perpendicular $[1\bar{1}0]$ direction is extended the same amount.

While these potentials are not the exact potentials seen by the hydrogen atom, they are the first terms of the expansion of the potential as a function of ϕ for the various symmetries, and should be adequate for this calculation.

Eigenfunctions and eigenvalues are obtained from Schroedinger's equation, using exponentials as the basis functions.

$$\psi = \sum_{m=-\infty}^{\infty} A_m \exp(im\phi) \quad . \tag{5.4}$$

In practice, values of m between -40 and 40 are used, since the coefficients A_m become vanishingly small for higher values of m.

Without including strain terms in the potential, the energy levels obtained for large values of the barrier height agree with the values obtained by the matrix method, as expected (Equations 1.1-1.3). Including the strain terms gives the dependence of the energy levels upon strain. A C' strain splits the lower degeneracy as seen in Figure 24(a). These are the only states which contain a linear energy dependence upon C' strain. The upper degeneracy is not split by a C' strain. These and the other energy levels contain second and higher order dependences upon the C' strain.

The energy levels are numerically derived by the hindered rotator calculation, which does not give analytical results. However, a very good approximation can be made to the numerical solution. The result has an

Figure 24. The energy levels of the hydrogen system as a function of C' strain.

(a) The energy levels of the hydrogen system alone in the presence of C' strain.

(b) The potentials for the solution of the energy levels of the hydrogen-niobium local mode using the Born-Oppenheimer approximation. The energy levels of the local mode are shown at the top of (b). The numbers to the right of the energy levels indicate the degeneracy of the energy level.

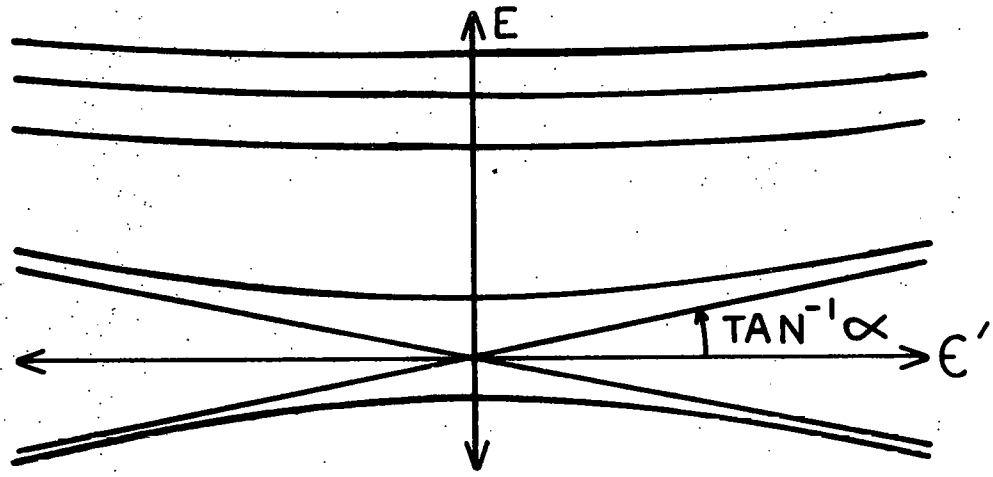

(a)

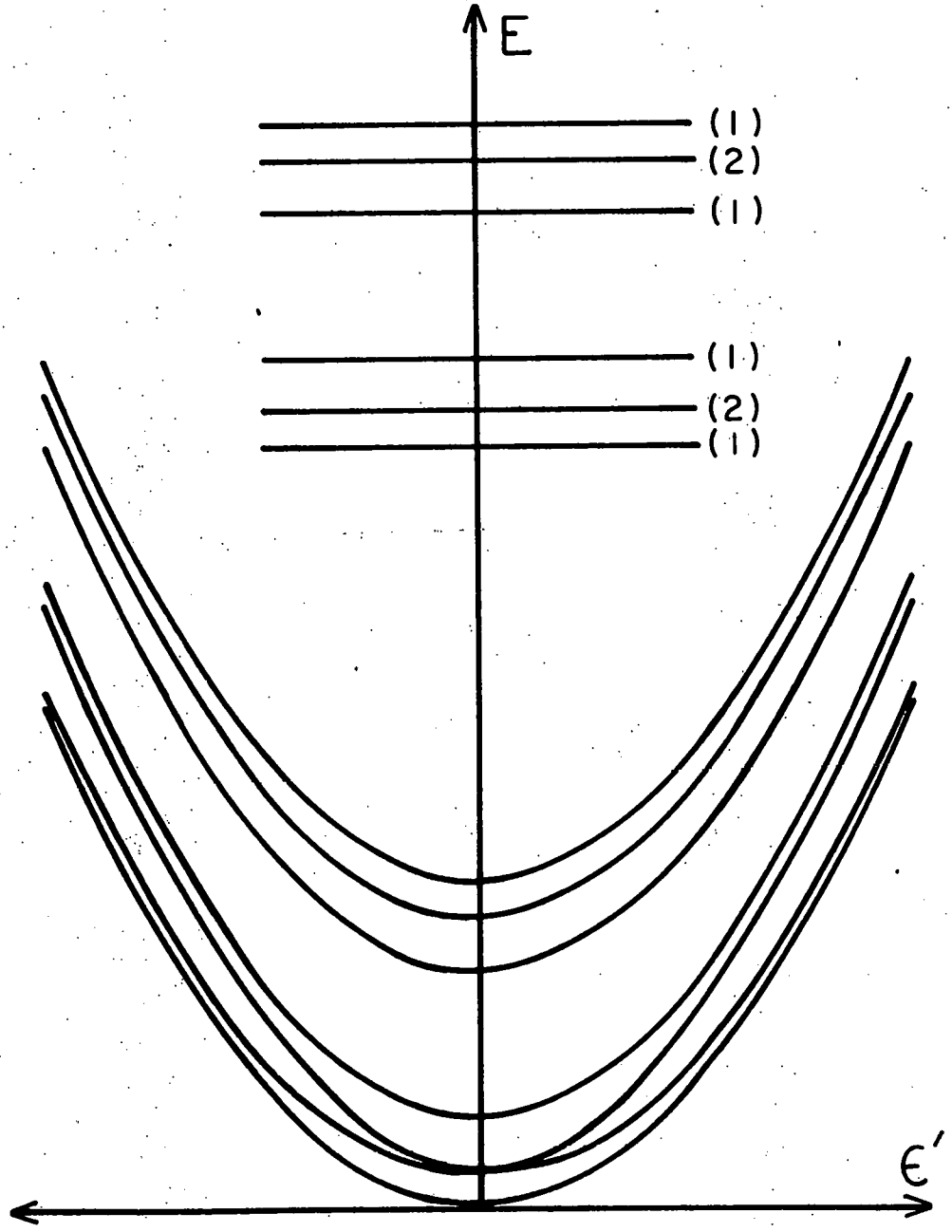

(b)

especially simple formula when the energies are measured with respect to the energy of the lower degeneracy in the absence of strain. In this case, the result is

$$E_1(\varepsilon) = -\sqrt{E_1(0)^2 + \alpha^2\varepsilon^2} \tag{5.5}$$

$$E_{2,3}(\varepsilon) = \pm \alpha\varepsilon \tag{5.6}$$

$$E_i(\varepsilon) = \sqrt{E_i(0)^2 + \alpha^2\varepsilon^2} \qquad i \neq 1,2,3 \tag{5.7}$$

where $E_i(0)$ is the energy of each level in the absence of strain. The parameter α determines the slope of the energy of the lower degeneracy. It also determines the relaxation strength and is related to the lambda tensor (Equation 3.3).

The behavior of the energy levels under a C_{44} strain is similar, except that the upper degeneracy is now split, while the lower degeneracy is not. These results depend upon the offset ε being of the same order or larger than the energy level splitting in the absence of offset. For small offsets, both degeneracies are split by both C' and C_{44} strains.

These calculations were performed with the assumption that the potentials used were due to interactions with a rigid lattice. The motion of the lattice, especially local modes around the defect, will add coordinates of motion. As long as the motion of the hydrogen is faster than the motions of the neighboring lattice atoms, the Born-Oppenheimer approximation can be used to separate the coordinates of motion of the hydrogen and neighbor atoms (Seitz 1940). For instance, a local mode with C' symmetry will add quadratic and higher order strain terms to the energy levels due to the elastic energy of the neighbors

(Figure 24(b)). These curves now become the potentials for finding the energy levels of the entire system. These new energy levels can be seen near the top of Figure 24(b). The energy levels retain the same features as the energy levels of the hydrogen alone. A Jahn-Teller type splitting of the lower degeneracy occurs, but the new energy levels remain degenerate, and are lowered with respect to the surrounding levels. A simple calculation of the expected size of the energy shift indicates that it will be small compared to the scale of the energy splitting. Since including the motion of the neighbors does not introduce new features and does not drastically change the energy levels, this discussion will no longer include that motion.

2.0 Trapping Orientations

The effect of bias strains due to trapping can now be considered. Baker and Birnbaum (1973) suggest three orientations of the O-H complex from their measurements of relaxation around 150K (Figure 25).

The first orientation places the hydrogen ring in the nearest neighbor position with respect to the oxygen. This is shown in the lower diagram of Figure 25 and is designated as a [100] orientation. By symmetry it can be seen that no C_{44} strain due to the oxygen can exist, but a large C' strain, designated ε_2, is present. The effect of this combination of strains is seen at the right of the diagram, showing how the lower degeneracy has been split.

The second orientation has the ring in the next nearest neighbor position as shown by the middle diagram of Figure 25. Again, no C_{44} strain is present, by symmetry. A C'strain, designated ε_1, is still present, but because of the increased distance between the hydrogen and oxygen and because the oxygen is not in the plane of the hydrogen ring, the strain is expected to be smaller.

Figure 25. The three orientations of the O-H complex. The oxygen is represented by the large circle on the edge of each unit cell. The splittings of the degeneracies is indicated to the right of each complex. The number in parenthesis indicates the degeneracy of the energy level.

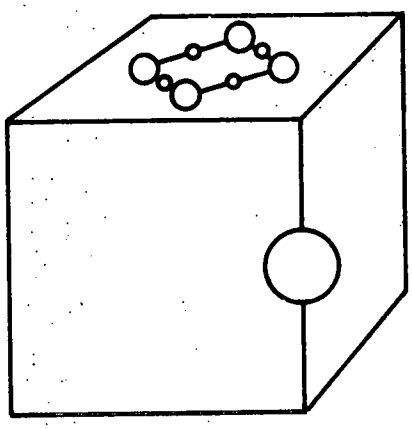

[111]

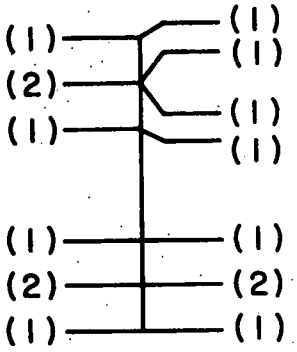

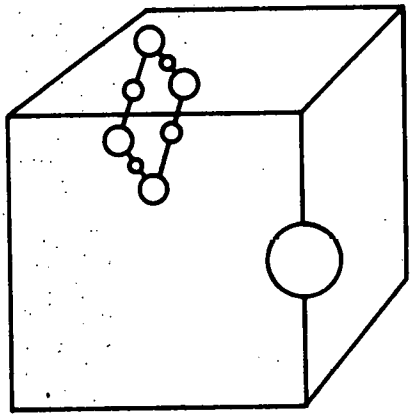

[110]

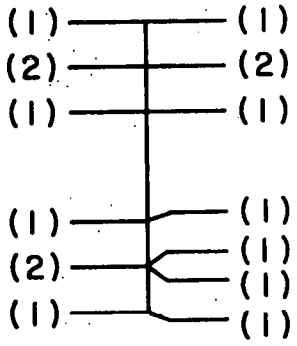

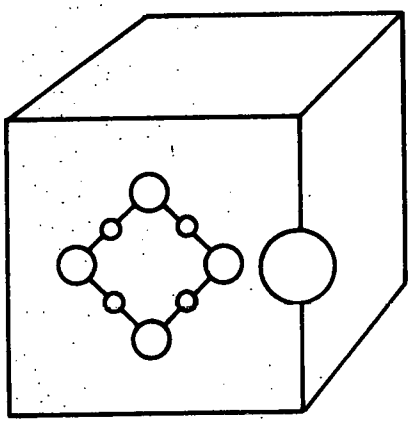

[100]

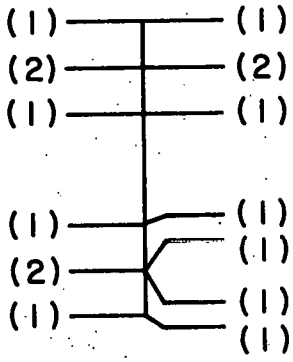

The effect upon the energy levels is shown to the right of the diagram, similar to the [100] results, but with less splitting.

The third orientation moves the ring to the third nearest neighbor [111] position shown in the top diagram of Figure 25. No C' strain is present by symmetry, but a C_{44} strain is present. The energy level diagram shows that the lower degeneracy is not split, while the upper degeneracy is split.

In summary, there is a large C' bias strain for the [100] orientation, a smaller C' bias strain for the [110] orientation and no C' bias strain for the [111] orientation. Furthermore, a distribution of additional strains from other neighboring defects provide additional splittings. These additional, random strains should be smaller in magnitude than the strains due to the trap defect because of the greater distance between the hydrogen and the defect. This distribution of bias strains superimposed upon the trapping strains produce a distribution of strains and energy levels as shown in Figure 26. The additional strains produced by the other defects do not depend upon the orientation of the O-H complex, so the width of the distribution of strains for each orientation, $\delta\varepsilon$, should be equal. Since the distribution of random strains is dependent upon other defects than the trapping defect, purer samples would be expected to have narrower distributions of the bias strains.

The splitting of the lower degeneracy varies the energy difference between the ground state and first excited state. As the splitting increases, the heat capacity at low temperatures increases. The heat capacity is calculated using Equation 1.8. The energy levels E_i are known as functions of w (Equations 1.1-1.3), along with their strain dependence (Equations 5.5-5.7).

Figure 26. The energy levels of the hydrogen system indicating bias strains of [111], [110] and [100] orientations. The strain broadening, $\delta\varepsilon$, is indicated by the shading and is the same for each orientation.

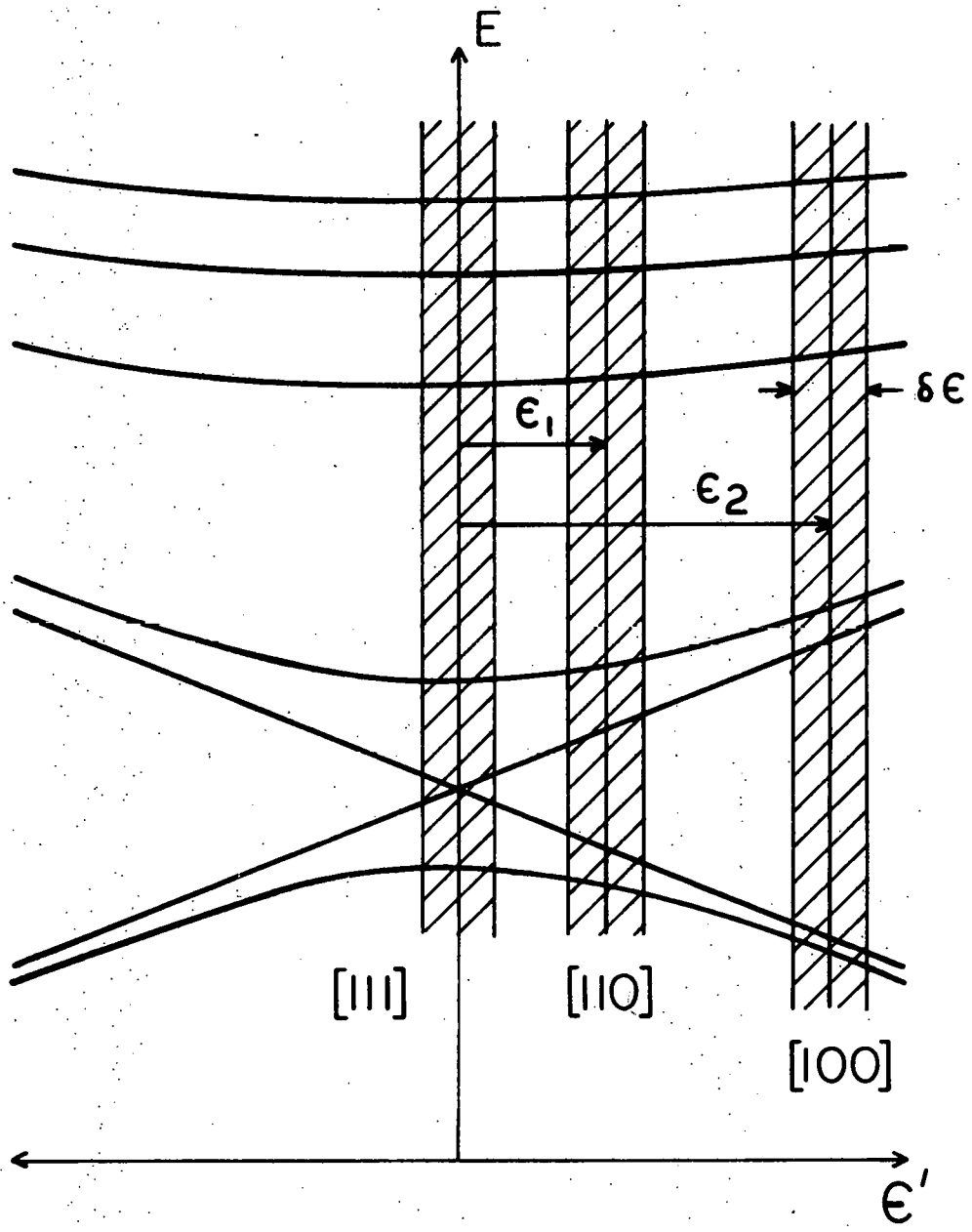
E
δε
ε1
ε2
[111]
[110]
[100]
ε'

A value of 0.5 was assumed for w, and the resulting curves for values $\alpha\varepsilon/k$ equal to 0, 1.5 K and 4 K are shown in Figure 27.

For zero splitting (Curve A), the heat capacity first peaks due to activations to the lower three excited states. The curve peaks again at higher temperatures due to excitations to the upper four excited states. A slight splitting of the lower degeneracy (Curve B, $\alpha\varepsilon/k$ = 1.5 K) moves the first excited state closer to the ground state, increasing the heat capacity at lower temperatures and lowering the first peak, but not drastically changing the shape of the curve. A large splitting (Curve C, $\alpha\varepsilon/k$ = 4 K) moves the first excited state quite close to the ground state, producing a sharp peak at lower temperatures. The rest of the states have much higher activation energies compared to the first state, and so produce a large, broad peak at higher temperatures.

A distribution of population in the three orientations discussed before can therefore produce heat capacity contributions over a wide range in temperature, the behavior being very dependent upon the splitting of the lower degeneracy. These three orientations contain degenerate energy levels which will cause relaxation under the appropriate stress. In the [111] defect, the lower degeneracy remains and will cause a C' relaxation. The [110] and [100] defects have upper degeneracies and will cause C_{44} relaxations.

The description of the relaxation which would be expected from this model depends upon the process by which transitions occur between the degenerate eigenstates. This determines the dependence of the relaxation time upon temperature.

A direct transition between the eigenstates with the emission of a phonon whose energy is equal to the energy difference between the eigenstates is a

Figure 27. The heat capacity of the hydrogen-oxygen complex as a function of temperature for various C' bias strains. The energy levels correspond to a value for w of 0.5. Curve A represents zero bias strain, curve B represents $\alpha\varepsilon/k$ = 1.5 K, and curve C represents $\alpha\varepsilon/k$ = 4 K.

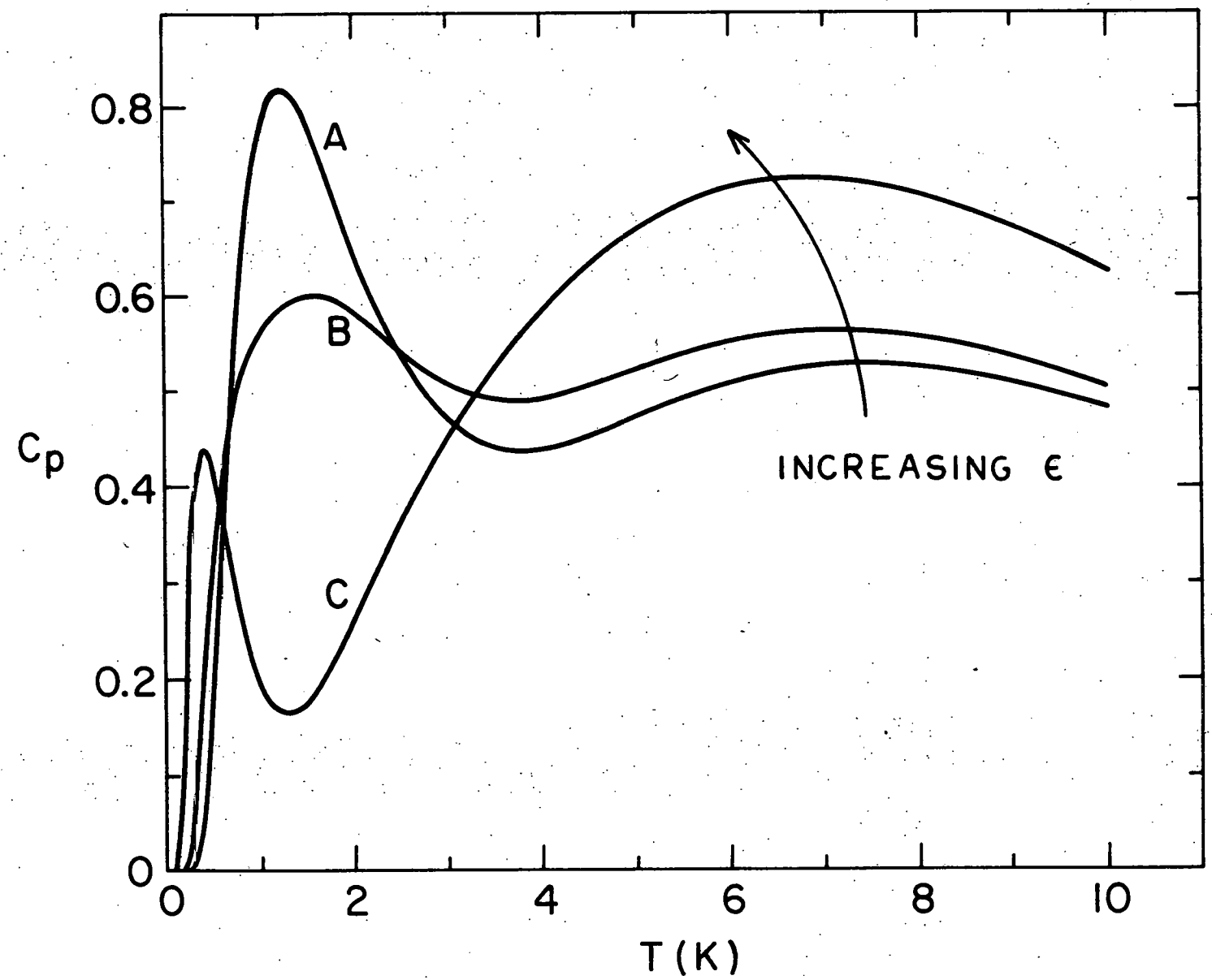
0.8
0.6
0.4
0.2
0
C_p
A
B
C
INCREASING ϵ
0
2
4
6
8
10
T(K)

possible process (Orbach 1961; Sussmann 1964; Stoneham 1975). However, the relaxation frequency has a linear temperature dependence for such a process. The experimental data indicates that the relaxation frequency has an exponential temperature dependence. There is much evidence to indicate that the exponential temperature dependence is not due to a classical activation process. Hence a process involving quantum mechanical eigenstates which produces an exponential dependence of the transition frequency on temperature is needed.

3.0 The Orbach Process

The Orbach process is a process which involves the absorption and emission of two phonons with the system passing through a real intermediate eigenstate (Orbach 1961; Sussman 1964). The process is shown schematically at the top of Figure 28. A transition between eigenstates A and C is desired. The states A and C are almost degenerate, the splitting being produced by an applied stress. If there exists a state B such that the energy difference Δ between state B and states A and C is much greater than the difference in energy between A and C, then the Orbach process proceeds by the absorption of a phonon with energy just less than Δ, causing a transition from A to B, followed by the emission of a phonon with energy just greater than Δ, causing a transition from B to C.

The relaxation time is given by

$$1/\tau = A\Delta^3[\exp(\Delta/kT) - 1]^{-1} \tag{5.8}$$

$$A = \frac{3}{2\pi\rho\hbar^4 v^5} \left\{ \frac{\left|\sum_i \langle A|V_i|B\rangle \langle B|V_i|C\rangle\right|^2}{\left|\sum_i \langle A|V_i|B\rangle\right|^2 + \left|\sum_i \langle B|V_i|C\rangle\right|^2} \right\} \tag{5.9}$$

Figure 28. The Orbach activation process. The transition occurs by the absorption of a phonon with the transition from state A to state B, followed by the emission of a phonon with the transition from state B to state C. The relaxation frequency versus inverse temperature is indicated by curve B. Increasing isotopic mass shifts the curve to A.

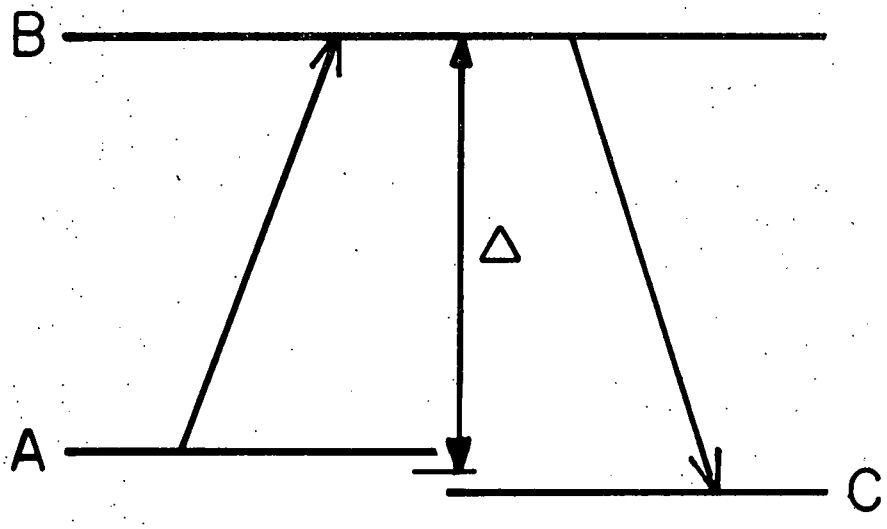
B
Δ
A
C

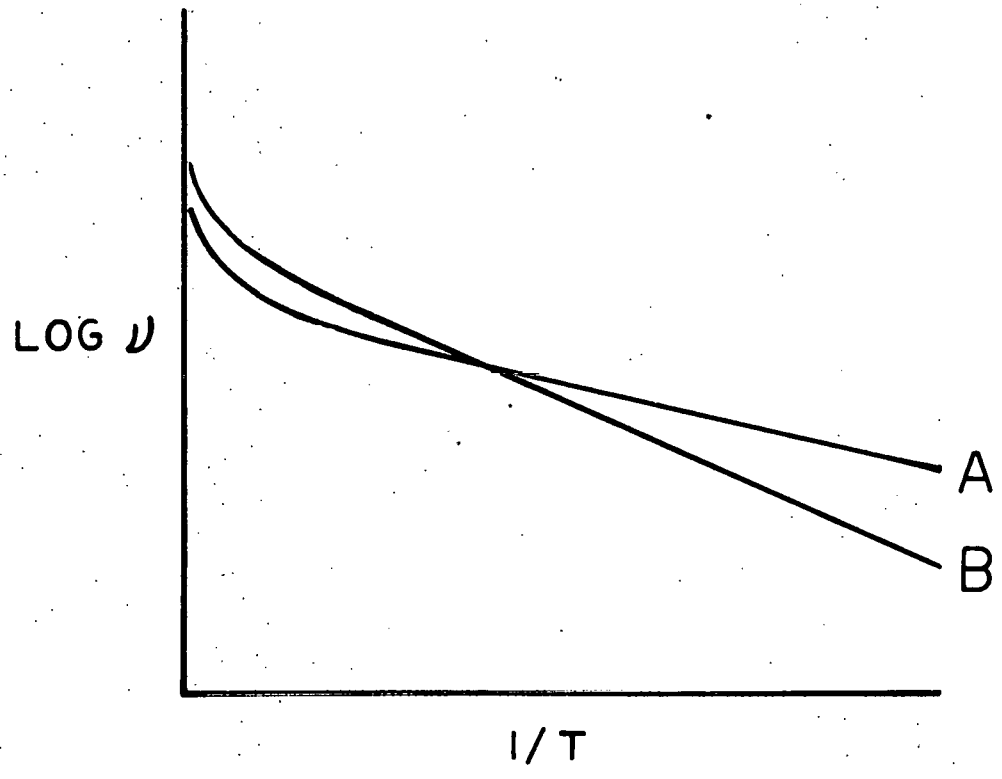
LOG ν
A
B
1/T

where $\hbar$ is Plank's constant, ρ is the density of the solid, v is the velocity of sound in the solid, and k is Boltzmann's constant. The terms $< A|V_i|B >$ represent matrix elements between the initial and final states for each transition caused by the interaction V due to the phonon strain field.

The temperature dependence is contained in the $[\exp(\Delta/kT) - 1]^{-1}$ factor. The log of this function is sketched as curve B at the bottom of Figure 28 versus inverse temperature. At low temperatures, the exponential dominates the factor, but at high temperatures, the difference causes a curvature away from a straight line. Hence at low temperatures the transition time has the form

$$1/\tau = A\Delta^3 \exp(-\Delta/kT) \qquad (5.10)$$

which has the appearance of a thermally activated process. However, the preexponential factors contain some very interesting features, especially for isotope effects, which are not contained in a classical activation process. Increasing mass tends to decrease the tunnelling overlap, causing a decrease in the energy level splittings, and a decrease in Δ. The decrease in Δ causes the slope of the curve in Figure 28 to decrease. However, because of the Δ^3 factor in the preexponential, the entire curve is lowered. These two effects are combined in curve A of Figure 28. If the factor A in Equation 5.10 is assumed to be constant, then two processes with activation energies Δ_1 and Δ_2 will have curves which intersect at a temperature

$$T = \frac{\Delta_2 - \Delta_1}{3 \ln(\Delta_2/\Delta_1)} \quad . \qquad (5.11)$$

Usually the factor A is not constant for changes in isotopic mass, because of the dependence upon the matrix elements. Since the wavefunctions are mass dependent, the matrix elements should also be mass dependent. The decrease in tunnelling overlap with increasing mass might be expected also to decrease the matrix elements. The hindered rotator model can be used to calculate the eigenfunctions and the matrix elements explicitly, while the matrix method cannot. These explicit calculations showing the decrease in the matrix elements for increasing isotopic mass will be considered in the next chapter.

4.0 The Relaxation Strength

The dependence of the energy levels upon strain can be used to calculate the relaxation strength as a function of temperature. The dependence of the energy levels can be characterized with two parameters. The first derivative of the first excited state energy with respect to C' strain is denoted by α. The difference in energy between the ground and first excited states is denoted by γ.

A thermodynamic calculation is used to determine the relaxation strength. The partition function

$$Z = \sum_i \exp(- E_i/kT) \tag{5.12}$$

is calculated from the energy levels derived earlier (Equations 5.5-5.7). The elastic constant change δC_{ij} is derived from the free energy F,

$$F = - kT \ln Z \tag{5.13}$$

$$\delta C_{ij} = \partial^2 F/\partial\varepsilon_i \partial\varepsilon_j \tag{5.14}$$

where ε represents the elastic strain. The results of this calculation are seen in Figure 29. The curve A represents the contribution to the elastic constant due to the transitions between the degenerate states alone. At high temperatures it decreases as 1/T, the same as a classical relaxation. As T approaches γ/k, the excited states begin to depopulate. This lowers the relaxation strength, which eventually goes to zero at T = 0. This decrease of the relaxation strength due to depopulation is unique to quantum mechanical systems and is not seen in classical relaxations.

The curve B is also unique. This contribution is derived from the second derivative of the ground state energy with respect to C' strain. As seen in Figure 24(a), the ground state has a negative second derivative with respect to strain. Since this contribution is not due to a relaxation between eigenstates, it is not a true relaxation. As long as the time required for the ground state to respond to applied stress is much shorter than one period of stress, the response will be in equilibrium and the calculation is valid. The total response is indicated by curve C, the sum of curves A and B. When the transition time between excited states is considered, the elastic constant change is related by

$$-\delta C = \Delta_B + \frac{\Delta_A}{1 + \omega^2\tau^2} \tag{5.15}$$

where Δ_A and Δ_B are the functions represented by curves A and B. At high temperatures, where $\omega\tau$ is small, the elastic constant change is given by curve C. At lower temperatures, where $\omega\tau$ increases, the elastic constant

Figure 29. The relaxation strength as a function of temperature. C_o is the molar concentration of defects, γ is the energy difference between the ground and first excited states, while α is the energy change of the first excited state per unit strain. Δ is the relaxation strength and v is the molecular volume.

Curve A represents the relaxation due to transitions between the degenerate first excited states.

Curve B represents the contribution from the curvature of the ground state.

Curve C is the sum of curves A and B.

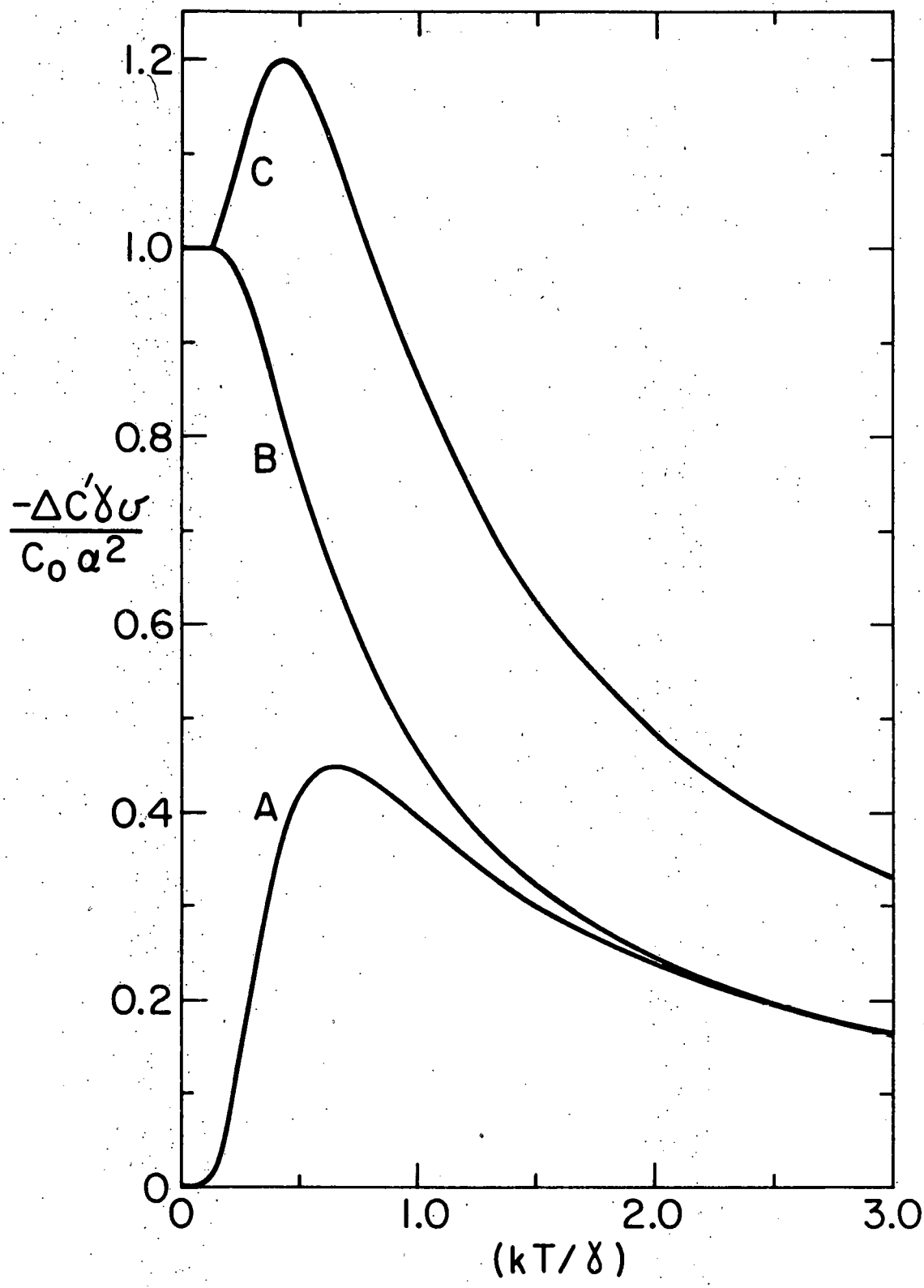
1.2
1.0
0.8
0.6
0.4
0.2
0
C
B
A
$\frac{-\Delta C'\gamma\sigma}{C_0 a^2}$
0
1.0
2.0
3.0
(kT/γ)

change falls below curve C and approaches curve B, which it follows to the lowest temperatures.

The three figures showing relaxation time, relaxation strength and heat capacity as functions of temperature (Figures 28, 29, 27) allow the fitting of the experimental data with essentially three new parameters. The slope of the first excited state energy versus strain, α, which is related to the lambda tensor seen in Equation 3.3, determines the strength of the relaxation. The activation energy Δ, equal to the energy spacing between the lower degenerate state and the excited state through which the transition occurs, determines the temperature dependence of the relaxation time and also the shapes and positions of the relaxations. The energy difference between ground and first excited states, γ, determines at what temperature depopulation occurs, which affects the relaxation strength, and determines the characteristics of the heat capacity contribution. There are other less significant parameters which will be used to fit the experimental data. The bias strains due to trapping, ε_1 and ε_2, the strain broadening due to other defects, $\delta\varepsilon$ and the concentration of defects in each orientation, are used in the fit to the heat capacity. These strain effects also influence the relaxation, because of the dependence of the energy levels upon strain. The strain broadening has a direct effect in changing the temperature dependence of the relaxation, as will be seen. While these other parameters are not unimportant to the model, the three parameters α, Δ, and γ will be found to be critical factors in the test of the delocalized bound hydrogen model.

CHAPTER 6.

THE DISCUSSION

In the previous chapter, the effect on the delocalized model of hydrogen binding to other interstitials was accounted for by considering the bias strains at the hydrogen sites due to the trapping defect. The expected contributions of this delocalized bound model to the heat capacity and anelastic relaxation were calculated in terms of three main parameters. The comparison of the experimental results of Chapter 4 with the model of Chapter 5, along with the determination of the values for the various parameters, remains.

The high temperature relaxation will not be considered in great detail in this discussion, except where it contributes to the understanding of the low temperature relaxation. The high temperature relaxation was identified as being due to hydrogen pairs. Since no allowance was made in the theory to accommodate these pairs, this relaxation will not be discussed further here.

1.0 Model Parameters

There are three main parameters which determine the properties of the delocalized bound hydrogen model. The different methods of calculating the properties of the model each have separate parameters which are most convenient to use with that method. These parameters are not all independent. This discussion will use the parameters which are most convenient for interpreting the ultrasonic data: α, Δ and γ. The parameter α represents the derivative of the first excited state energy with respect to C' strain. The activation energy of the Orbach process is represented by Δ. The energy difference between

the ground state and first excited state in the absence of strain is represented by γ.

The hindered rotator calculation uses the same parameter α. However, the other two parameters are the energy offset between tetrahedral and triangular sites, ε, and the potential barrier between sites, B. The matrix method of Birnbaum and Flynn uses the same parameters α and ε, but uses a different third parameter, V, which represents the overlap integral of wavefunctions located on adjacent interstitial sites. Of these six parameters, only three are independent, and can be converted to the other sets.

The procedure for this discussion will be as follows: (a) the ultrasonic decrement data showing peak position and relaxation strength as a function of temperature will be used to determine the parameters α, Δ and γ; (b) these parameters will be converted to the hindered rotator parameters α, ε and B, and the matrix method parameters α, ε and V for calculating additional properties of the model; and (c) to check the validity of the parameters, theoretical fits will be made to the heat capacity, the deuterium decrement and the hydrogen velocity.

2.0 The Polarization Dependence

The experimental results indicate the presence of a relaxation in the C' mode, with the absence of a C_{44} or B mode relaxation (Figures 17, 14). The splitting of the lower degeneracy by a C' strain provides the basis for a relaxation in that mode. However, the splitting of the upper degeneracy by a C_{44} strain is also expected to lead to a relaxation in that mode. Also, when the offset ε between triangular and tetrahedral sites is much smaller than the energy splitting between levels, both degeneracies give rise to

relaxations in both C' and C_{44} modes. In order to remain consistent with experimental results, the offset ε must be comparable to or larger than the splitting between levels. This eliminates any C_{44} relaxation from the lower degeneracy. If the activation energy from the ground state to the upper degeneracy is large compared to kT in the temperature range of interest, then the population of the upper degeneracy would be too small to give a visible relaxation. Because the background velocity of the C_{44} mode has such a large temperature dependence near the superconducting transition temperature and above (Figure 12), a small relaxation would be difficult to observe except at lower temperatures.

3.0 The Determination of Δ, γ and α

The activation energy of the relaxation process is determined by plotting the log of relaxation frequency versus inverse temperature as in Figure 30. Curve A passes through the data for the hydrogen relaxation. The functional form of curve A is given by

$$\nu = \frac{1}{2\pi\tau} = \frac{3.89 \times 10^{10}}{[\exp(1.8/kT)-1]} \qquad (6.1)$$

where kT is measured in meV. The activation energy, Δ, is thus determined to be 1.8 meV.

While the activation energy has been determined, the transition has not been identified. There are five states which have higher energy than the lower degeneracy, two of which are also degenerate. Transitions can occur to each of these excited states, but the transition which dominates is expected to be the one with the strongest coupling with the lower degeneracy. The matrix

Figure 30. The logarithm of relaxation frequency as a function of inverse temperature. Curve A is the fit to the data points of the hydrogen relaxation, with an activation energy of 1.8 meV. Curve B is the fit to the deuterium data point with the same activation energy. Curve C is the fit to the deuterium data point with the activation energy determined by the hindered rotator calculation, 1.0 meV.

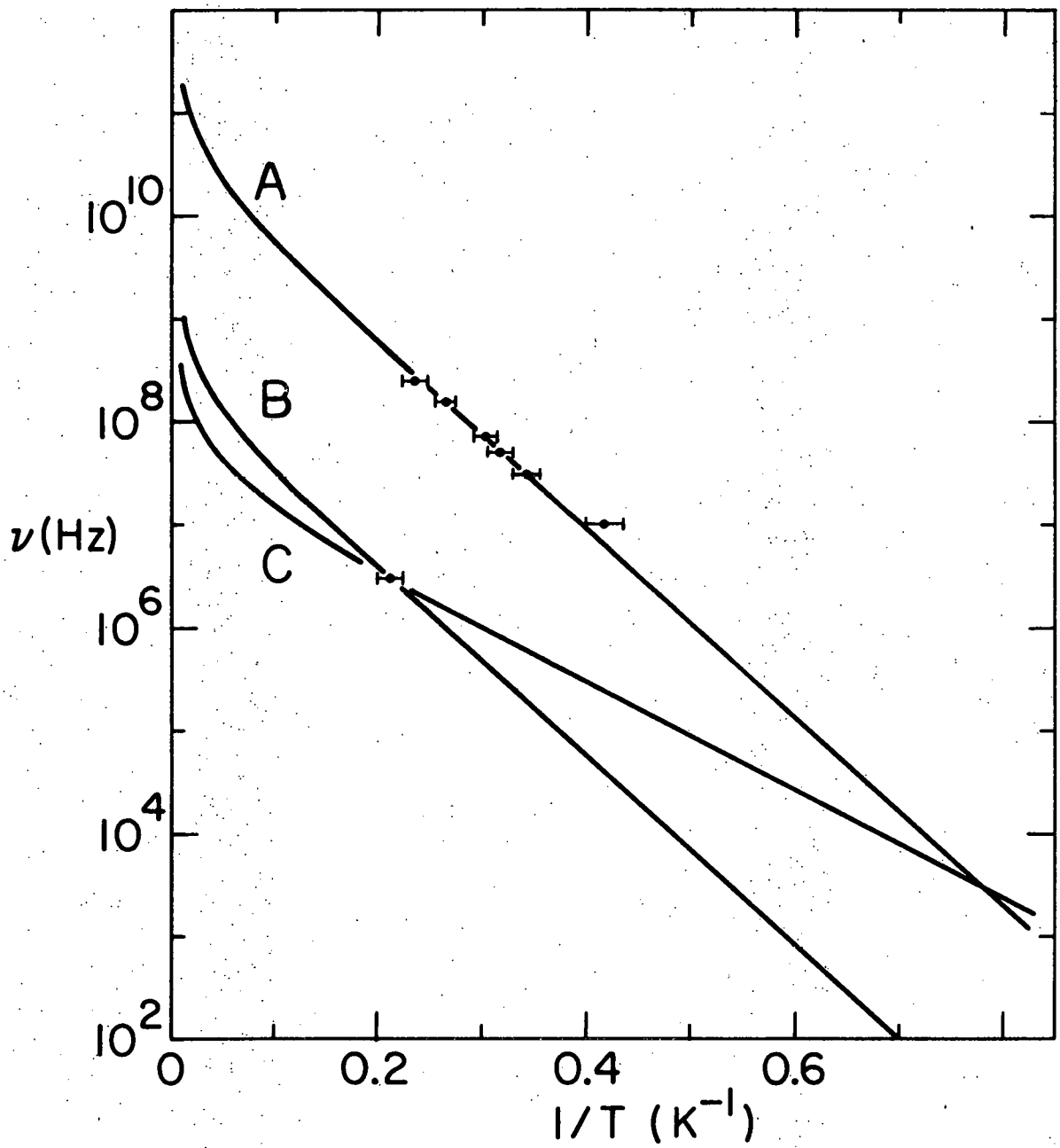
A
B
C
10^{10}
10^{8}
10^{6}
10^{4}
10^{2}
ν(Hz)
0
0.2
0.4
0.6
1/T (K^{-1})

elements due to phonon coupling between the lower degeneracy and each excited state can be calculated. While these matrix elements have been calculated, in the Appendix, a simpler argument using the symmetry of the eigenstates identifies the correct transition.

Inspection of the wavefunctions derived by the hindered rotator model (Figures 32, 33) or the wavefunctions obtained from the matrix method indicates that the wavefunctions of the lower degeneracy have odd symmetry. That is, the inversion operation yields the negative of the original wavefunction. The phonon interaction which causes the transition is due to a strain, which has even symmetry. This provides selection rules for the matrix elements <AIVIB>. Since A is odd and V is even, the matrix element will be non-zero only for states B which also have odd symmetry. The upper degenerate states Ψ_6 and Ψ_7 are the only other states which have odd symmetry, and so are the only states which allow transitions due to phonon interactions. Therefore, the activation energy Δ = 1.8 meV corresponds to the energy difference between the lower degeneracy, E_2 and E_3 and the upper degeneracy E_6 and E_7.

The activation energy was used to determine the energy difference between the two sets of degenerate states. It was seen in Figure 29 that the relaxation strength is a function of the energy difference between the ground state and the lower degenerate states. It was noted in Figure 15 that the relaxation strength for the various frequencies did not follow a classical 1/T temperature dependence. This data is shown in Figure 31. The solid line through the data points is the fit of curve A for a value of 4.5 K for γ/k. The relaxation strength is also determined from this data, at least in principle. However, as pointed out in the experimental data chapter, the concentration of trapped hydrogen has not been determined. Therefore, the product

Figure 31. The relaxation strength versus temperature. The solid line through the data points is the fit of the delocalized bound hydrogen model with the parameter $\gamma/k = 4.5$ K. The other line indicates the classical relaxation strength which approaches the same high temperature limit as the delocalized bound model.

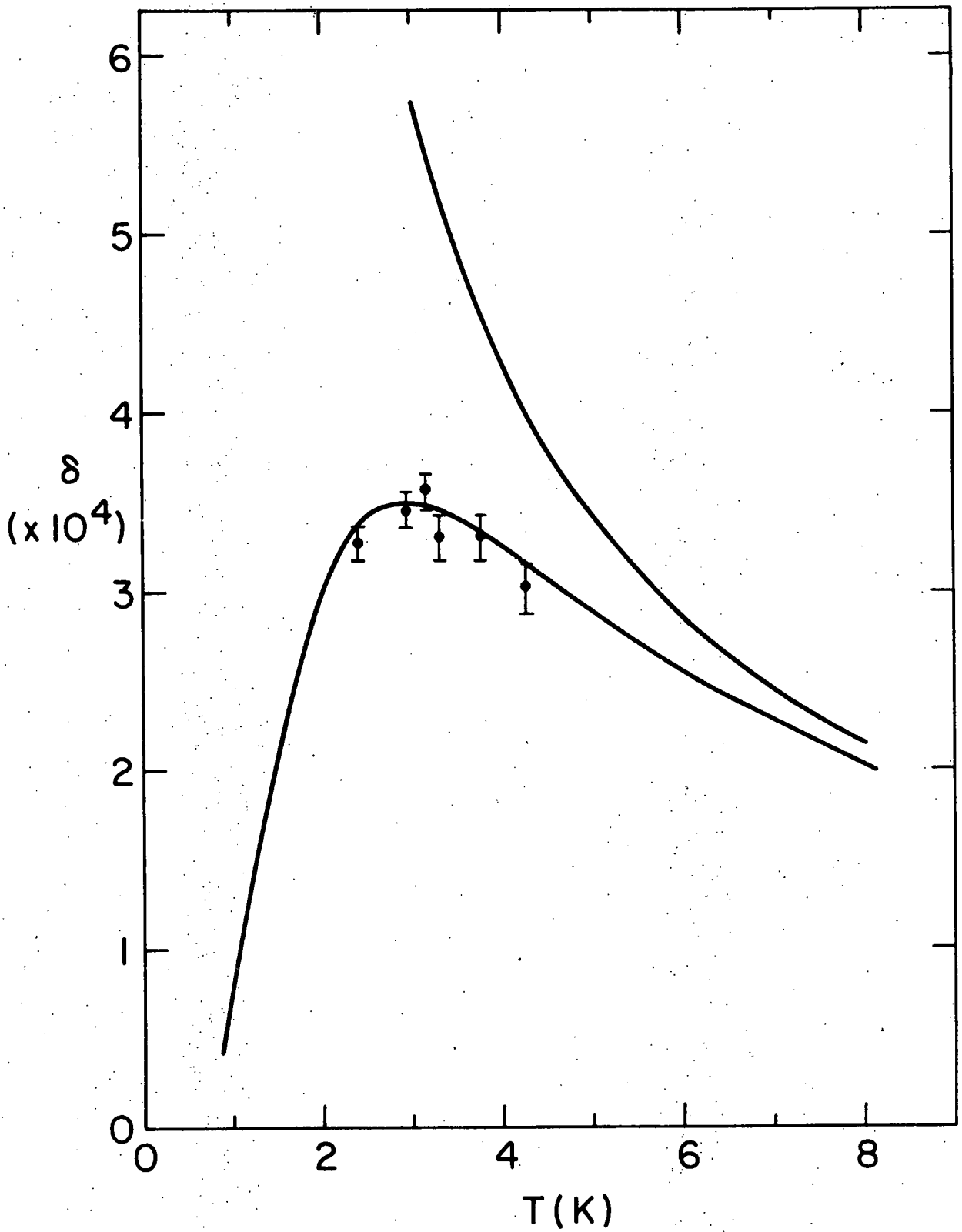
6
5
4
3
2
1
0
δ
(x 10^4)
0
2
4
6
8
T(K)

of concentration and α^2 cannot be separated with confidence. The data gives a value for $C_o\alpha^2$ equal to 1.0×10^{-29} erg^2. The concentration of hydrogen in the sample was 2150 ppm. However, only 1000 ppm of oxygen was present, so the maximum amount of hydrogen which did not precipitate was 1000 ppm. The quenching experiments indicated that even the concentration of bound hydrogen could vary, depending upon the cooling rate, due to the dissociation of O-H pairs and the precipitation of the hydrogen. Therefore an estimate of 500 ppm will be used for the hydrogen concentration, half of the maximum possible value. Since the error introduced into α by an incorrect value of concentration varies with the square root of concentration, this should give the value of α to within 40%. This value for α is 90 ± 40 meV. The three parameters determined by the ultrasonic data are collected in Table 5, along with the equivalent parameters used by the other methods.

Measurements by Buchholz, Volkl and Alefeld (1973) of the elastic constants of tantalum charged with 1% hydrogen found no evidence of a 1/T dependence of the elastic constant due to a relaxation. The maximum possible value of $\delta\lambda$ consistent with their data is 0.03. The value of 90 meV for α derived for NbH corresponds to $\delta\lambda = 0.013$. This is less than half the upper limit placed upon $\delta\lambda$ by their experiment, and is consistent with their conclusion that the strain due to a hydrogen defect is nearly isotropic.

The value of the barrier potential B used in the hindered rotator calculation, 0.8 eV, may seem quite large. As mentioned previously, the potentials are assumed to be sinusoidal. The barrier height is adjusted to give the proper energy level spacing determined by the ultrasonic data. If the actual potential barrier were wider than a sinusoidal barrier, then the barrier height could be greatly reduced and still give a reasonable fit to the data.

TABLE 5.

DELOCALIZED BOUND HYDROGEN PARAMETERS

Calculation	Parameter Values		
Ultrasonic Data	α = 90 ± 40 meV	Δ = 1.8 meV	γ = 0.4 meV
Matrix Method	α = 90 ± 40 meV	ϵ = 1.0 meV	V = 0.5 meV
Hindered Rotator	α = 90 ± 40 meV	ϵ = 1.0 meV	B = 0.8 eV

The matrix method of calculation uses the tunnelling overlap integral V, which is isotope dependent. The hydrogen overlap V_H can be determined from the values of Δ and γ, which gives V_H = 0.5 meV. The deuterium overlap V_D, obtained from the energy levels of the hindered rotator calculation, is found to be 0.028 meV. This gives a value for $\beta = V_H/V_D$ of 18, which is much greater than the value of 3 derived by the Birnbaum-Flynn calculation. However, the calculation of the heat capacity due to hydrogen and deuterium will show that even this larger value of β will fit the experimental data, using the delocalized bound hydrogen model.

4.0 The Deuterium Ultrasonic Results

Because the deuterium decrement peak was so broad as a function of temperature, and overlapped the superconducting transition, the determination of the peak position in temperature was impossible except for the 3 MHz data. For this reason, only one data point is available, as shown in Figure 30 at the intersection of curves B and C. In a classical process, the activation energy is isotope independent. This is indicated by curve B, which has the same activation energy as the hydrogen curve A. However, since this is a quantum mechanical system, the activation energy should be isotope dependent.

Using the hindered rotator calculation (Equations 5.1-5.4), plus the appropriate parameters from Table 5, the deuterium activation energy and matrix elements can be calculated, along with the eigenfunctions for both hydrogen and deuterium.

The activation energy is found to be approximately equal to the level offset ϵ, which is 1.0 meV. This is about one half of the activation energy of the hydrogen and is indicated by curve C in Figure 30. This is represented by

$$\nu = \frac{3.45 \times 10^7}{[\exp(1.0/kT)-1]} \qquad (6.2)$$

where kT is measured in meV. It can be seen that curve C intersects curve A at about 1.2 K. Therefore, at 1.2 K the hydrogen and deuterium relaxation frequencies should be equal, and below 1.2 K, deuterium should relax faster than hydrogen. The Orbach process requires that if the preexponential factor A in Equation 5.8 is isotope independent, then the curves will intersect at 5.4 K (Equation 5.11). Therefore the factor A must be isotope dependent.

The only parts of the factor A which can have an isotope dependence are the matrix elements. The matrix elements are derived from the eigenfunctions, which are shown in Figures 32 and 33 for hydrogen and deuterium. The matrix elements $\langle A|V|B\rangle$ between all the states due to C' or C_{44} strain interaction (Equation 5.3) are displayed in the Appendix. As mentioned earlier, the eigenstates Ψ_2 and Ψ_3 have non-zero matrix elements only with the states Ψ_6 and Ψ_7. For hydrogen, the matrix elements are equal to 0.46 α while for deuterium, they are only 0.06 α. This gives a ratio of matrix elements due to the isotope change of about 8. The preexponentials of curves A and C are in a ratio of

Figure 32. The hydrogen wavefunctions determined by the hindered rotator calculation. The lower degeneracy consists of states Ψ_2 and Ψ_3. The upper degeneracy consists of states Ψ_6 and Ψ_7.

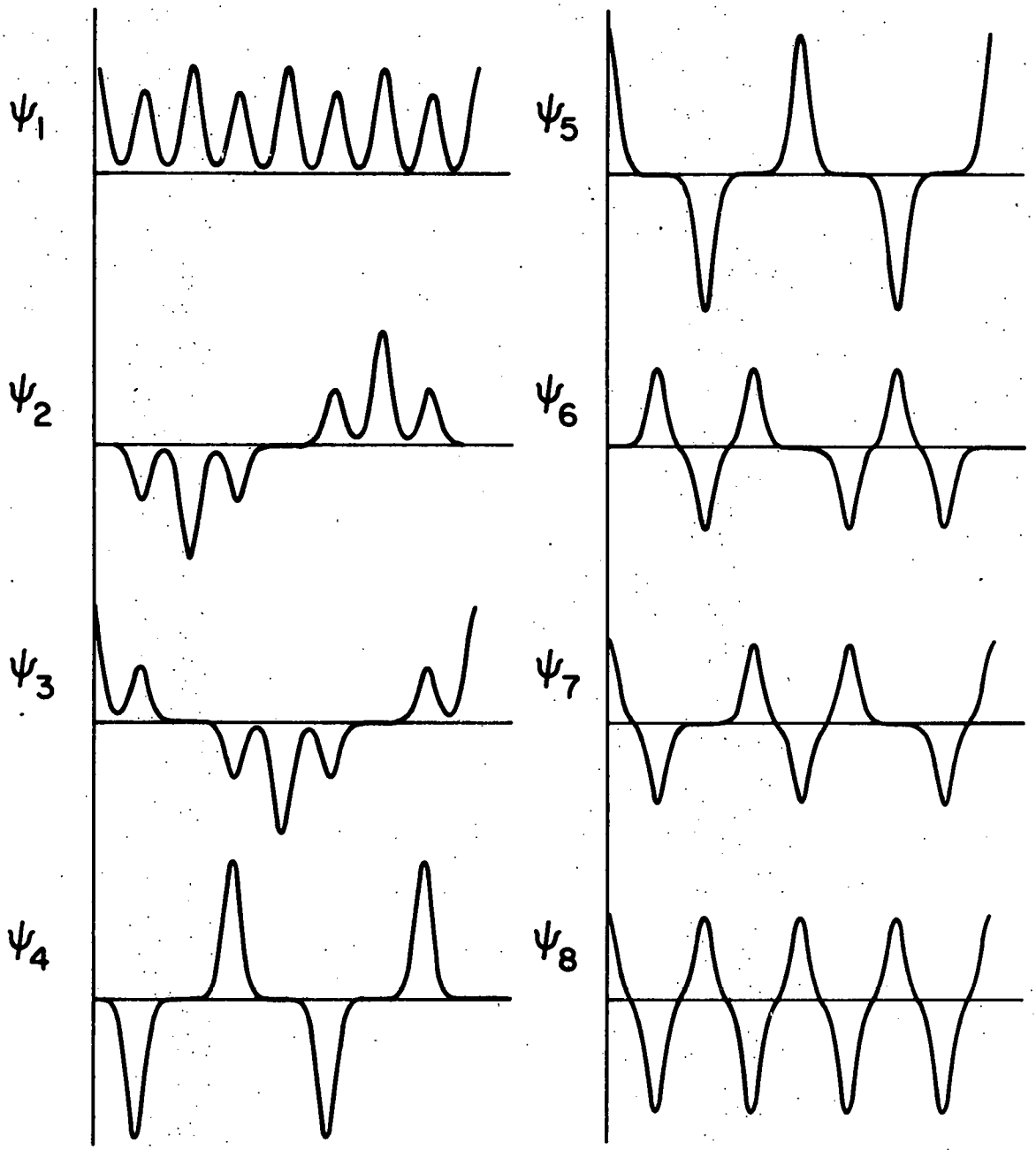
ψ_1
ψ_2
ψ_3
ψ_4
ψ_5
ψ_6
ψ_7
ψ_8

Figure 33. The deuterium wavefunctions determined by the hindered rotator calculation. The lower degeneracy consists of states Ψ_2 and Ψ_3. The upper degeneracy consists of states Ψ_6 and Ψ_7.

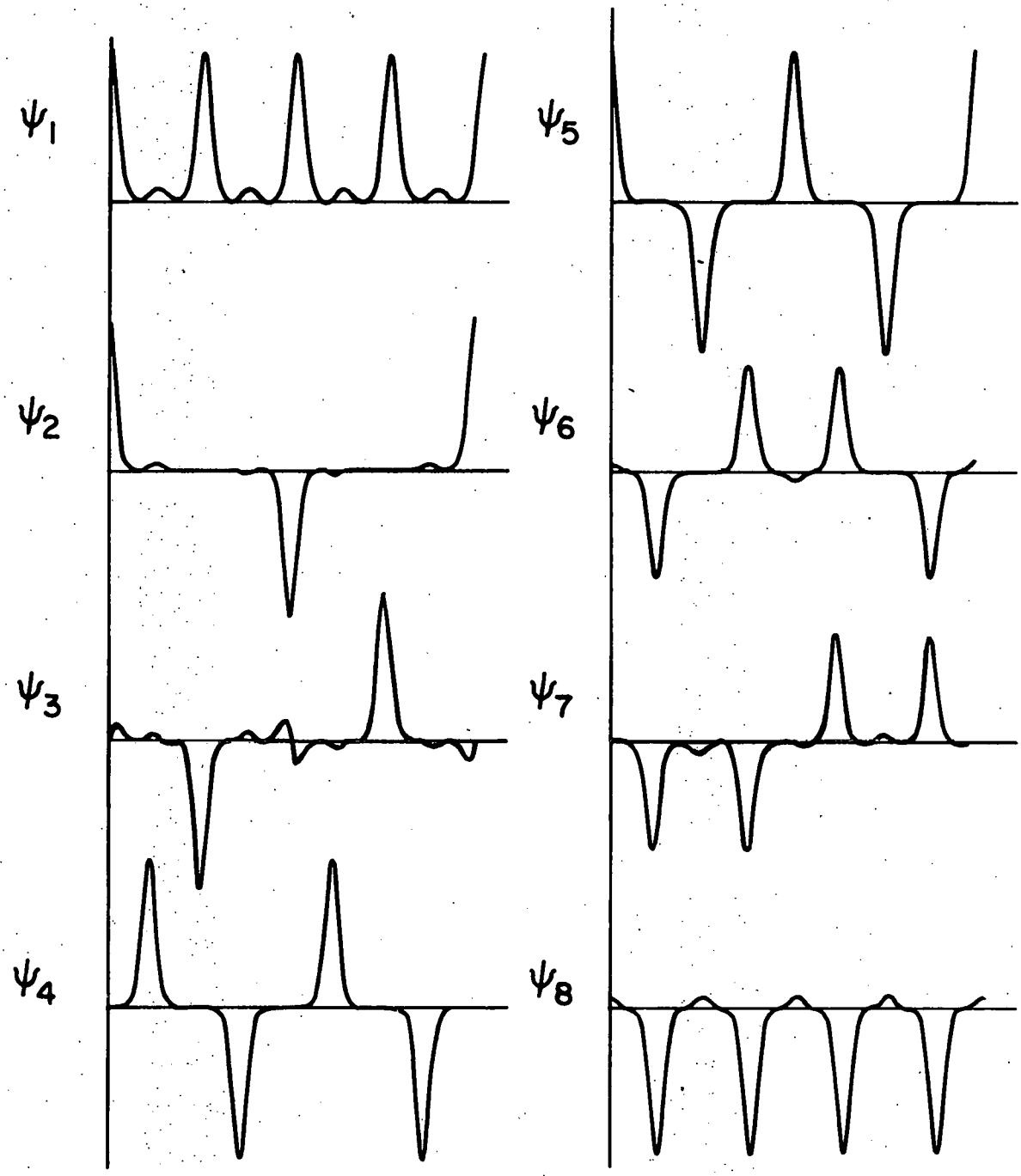
ψ_1
ψ_2
ψ_3
ψ_4
ψ_5
ψ_6
ψ_7
ψ_8

1100. Taking into account the activation energy change, the ratio of matrix elements required to fit the experimental data is 14. While this is not an excellent agreement, it does indicate that the model is capable of obtaining reasonable isotope effects, which a classical model will not produce. Furthermore, the matrix elements are sensitive to the tunnelling overlap between adjacent sites, which has an exponential dependence upon the barrier height. Small changes in the barrier potential mentioned before could therefore affect the matrix element ratio.

5.0 The Deuterium Decrement

The results of the hindered rotator calculation have determined the deuterium relaxation frequency as a function of temperature. A qualitative comparison can be made of the decrement expected from a classical result (Curve B of Figure 30) and the hindered rotator result (Curve C of Figure 30) with the experimental data. This is shown in Figure 34. The data taken at 3 and 10 MHz are normalized and drawn by the solid lines. The classical results are indicated by the dashed lines labeled 21 K, while the hindered rotator results are indicated by the dashed lines labeled 12 K.

On the 3 MHz data, it can be seen that the hindered rotator result produces a wider peak which more closely fits the data than the classical result. Similarly, at 10 MHz, the hindered rotator produces a much wider peak. Especially on the 10 MHz data, the hindered rotator result keeps the decrement elevated on the high temperature side of the peak. The high temperature relaxation which occurs around 9 K also contributes to the decrement to keep the curve elevated at high temperatures.

Figure 34. The fit of the delocalized bound model to the deuterium decrement for D/Nb = 1800 ppm at 3 and 10 MHz. The solid lines represent the experimental data. The dashed curves represent the expected results for a classical activation energy, 21 K, and the activation energy derived by the hindered rotator calculation, 12 K. The effects of strain broadening have not been taken into account in the theoretical fits.

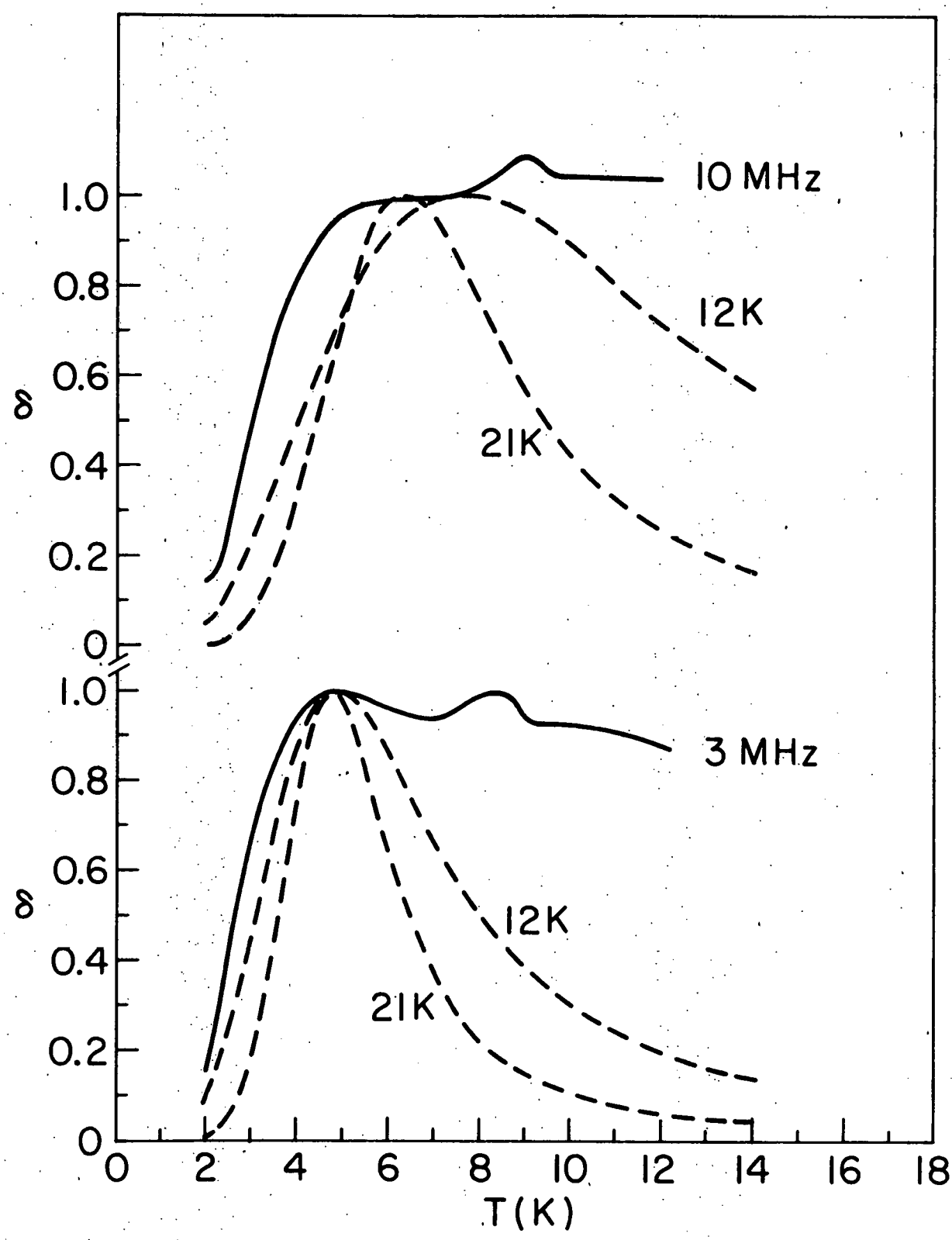
10 MHz
12K
21K
3 MHz
12K
21K
δ
δ
1.0
0.8
0.6
0.4
0.2
0
0
2
4
6
8
10
12
14
16
18
T(K)

The effect of the strain broadening will also contribute to the width of the decrement peak. Curve C of Figure 30 shows the relaxation time versus inverse temperature. Strain broadening will produce a distribution of curves with different slopes and preexponentials, which makes a band of curves in Figure 30 centered around curve C. A horizontal line at the measurement frequency determines the width of the peak by the temperature where it passes through the band of curves. Because the curves are plotted versus inverse temperature, a relaxation at a high temperature will have a wider decrement peak than a relaxation at a lower temperature, and any broadening on the high temperature side of the curve will produce a greater widening of the decrement peak than broadening on the low temperature side. Also, a curve which has a lower activation energy will produce a wider decrement peak than a curve with a higher activation energy for the same broadening. These are all reasons why the deuterium peaks are wider than the hydrogen peaks and remain elevated at high temperature.

6.0 The Heat Capacity Fit

The matrix method parameters in Table 5 can be used to predict the contribution of the hydrogen systems to the heat capacity. While these three parameters determine the main characteristics of the heat capacity, other parameters which were defined in Figure 26 are necessary to complete the calculation. The parameters ε_1 and ε_2 represent the bias strains experienced by the [110] and [100] rings, respectively, while $\delta\varepsilon$ represents the strain broadening around each strain. In addition, the parameters N_0, N_1, and N_2 represent the concentration of defects in the [111], [110] and [100] orientations, respectively.

The parameters ε, V_H and β were inserted as constants. The other parameters were varied to obtain the best qualitative fit. Because of the large number of parameters and the complexity of the numerical calculation, a least squares fit was not attempted. A fit to the experimental data is shown in Figure 35. The data points were obtained from Sellers (1975), and normalized. The data from several experiments are combined in the graph, which contributes to the scatter in the data points. The solid lines are the fit to the data, using the parameters listed in Table 6.

The parameter γ determines the activation energy from the ground state to the first excited state. For the hydrogen fit, this determines at what temperature the heat capacity will peak. The effect of the bias strains is to determine the specific temperature dependence of the heat capacity below the peak temperature. In the case of deuterium, the heat capacity fit is more difficult to analyze in terms of the parameters. The bias strains determine at which temperature the contribution from the various orientations will peak, while the strain broadening smooths the curve between peaks.

It is not alleged that these are the only values of the parameters which will fit the data. The fit is also relatively insensitive to some of the parameters. The contributions to the hydrogen heat capacity from the defects in the [111] and [110] orientations are almost identical, which means that the parameters N_{OH} and N_{1H} are not determined individually, but that the sum of the two should be about 20 ppm. Similarly, the parameters ε_1, ε_2 and $\delta\varepsilon$ are interdependent, and satisfactory fits to the data could be obtained for other combinations of these parameters.

The bias strains ε_1 and ε_2 are 0.16% and 0.05% respectively for α = 90 meV. These bias strains are smaller than expected for the elastic strains

Figure 35. The heat capacity fit of the delocalized bound hydrogen model. The parameters used in the fit are listed in Table 6. The data was derived from several experiments, and normalized to eliminate concentration effects. (Sellers 1975).

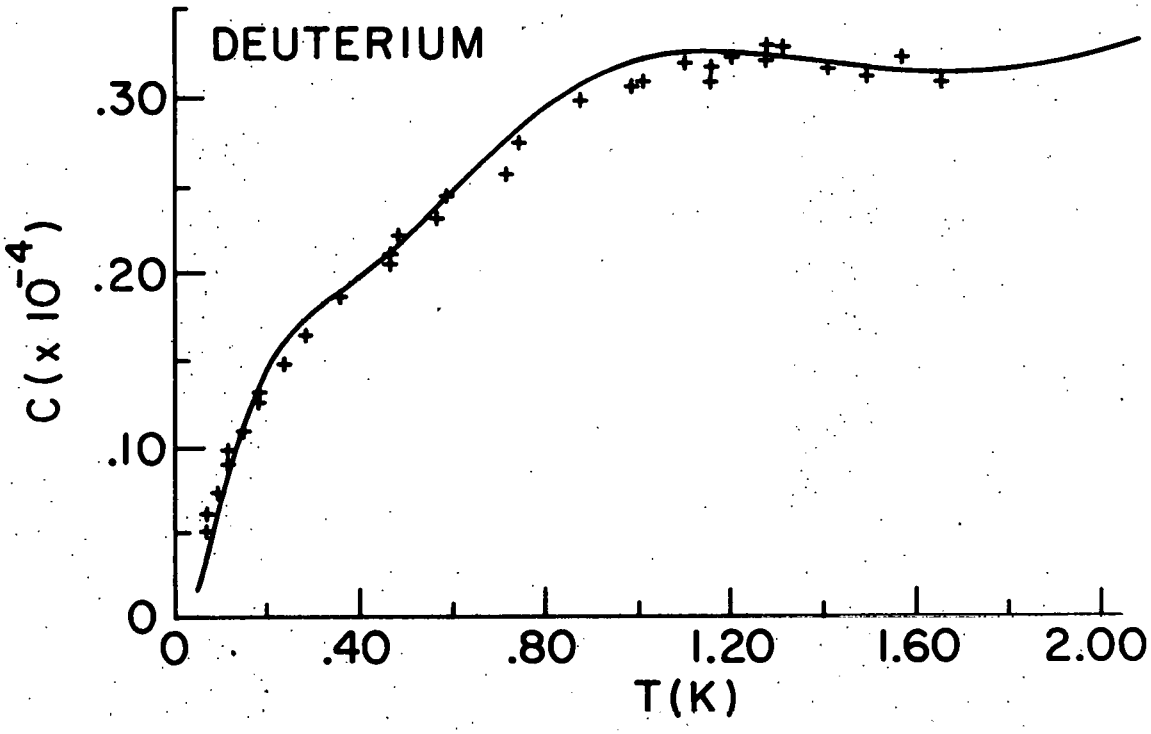
DEUTERIUM
.30
.20
.10
0
C(x 10^-4)
0
.40
.80
1.20
1.60
2.00
T(K)

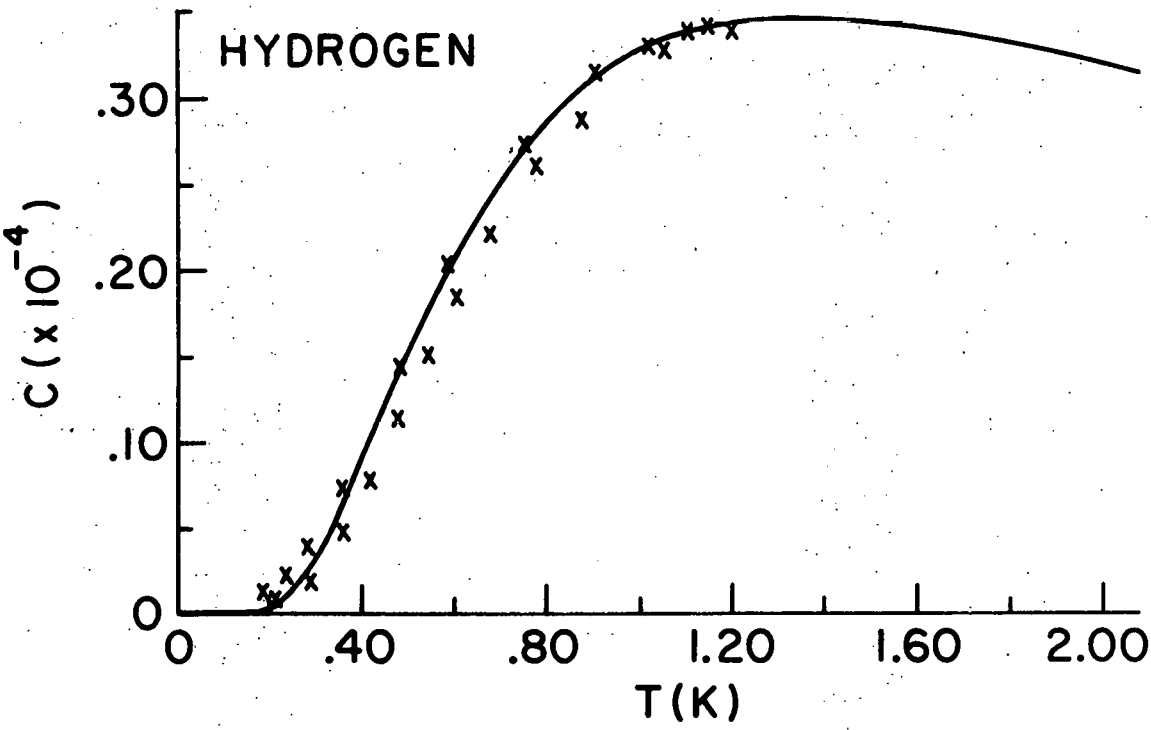
HYDROGEN
.30
.20
.10
0
C(x 10^-4)
0
.40
.80
1.20
1.60
2.00
T(K)

TABLE 6.

PARAMETERS OF THE HEAT CAPACITY FIT

V_H	0.5 meV	N_{0H}	10 ppm
β	15	N_{1H}	10 ppm
$\alpha\varepsilon_1$	0.05 meV	N_{2H}	33 ppm
$\alpha\varepsilon_2$	0.14 meV	N_{0D}	30 ppm
$\alpha\delta\varepsilon$	0.03 meV	N_{1D}	37 ppm
		N_{2D}	37 ppm

surrounding an oxygen interstitial. However, the value which is determined by the fit is $\alpha\varepsilon$, and since α has an uncertainty of 40%, the size of the bias strains could be 40% larger. The values of the concentrations in the various orientations are about what was expected. The total hydrogen concentration is about 50 ppm, which is the value that Sellers, Anderson and Birnbaum (1973, 1974) expected from their calculation of the entropy change. The total deuterium concentration is about 100 ppm, twice the hydrogen concentration. This would be expected, since deuterium diffuses more slowly than hydrogen (Matusiewicz and Birnbaum 1977) and so would precipitate less during cooling. The higher deuterium concentration is also consistent with the larger relaxation strength of the deuterium compared to hydrogen (Figures 17 and 20). The heat capacity results are also consistent with the trapping of hydrogen by another defect, since 3000 ppm of hydrogen was used in the heat capacity experiment, while only 50 ppm contributed to the heat capacity. The impurity analysis (Table 1) showed that as much as 200 ppm of trapping defects may be present in the niobium without previous charging.

This fit to the heat capacity depends upon the presence of the bias strains due to the trapping defects to split the lower degeneracy and force the first excited state close to the ground state, just as was done in the Birnbaum-Flynn calculation. However, because of the effectiveness of the bias strains in splitting the degeneracy, a large distribution of random strains due to other defects is not needed. Also, large values of β can be accommodated with excellent results.

7.0 Comparison of Theory with Hydrogen Velocity

The parameters used by the various models have been determined by the hydrogen ultrasonic decrement data. The hydrogen velocity data provides a check of the validity of the model, since the velocity can now be determined from the model with no new parameters. The relaxation frequency (Figure 30), the relaxation strength (Figures 29 and 31) and the decrement as a function of temperature are sufficient to predict the ultrasonic velocity data. As an example, the low concentration hydrogen data (Figure 11) will be considered. The velocity data is indicated in Figure 36, with the relatively small velocity contribution from the high temperature relaxation already subtracted. This data suffers slightly because the velocity and decrement were not measured for the same concentration of hydrogen. However, a distinct advantage is that the relaxation which appears around 5.5 K in the high concentration sample is almost absent in this data. This allows the frequency difference between the charged and uncharged samples to be determined more accurately, since the curves can be matched at high temperature. This matching of the curves at high temperatures does introduce a systematic error into the absolute value of the measurements. The matching is done by varying the origin of the vertical axis until the high temperature

Figure 36. The fit of the theoretical models to the frequency change of the C' mode with 160 ppm of hydrogen. Curve A represents the classical result expected for a relaxation which exhibits the observed decrement (Figure 11). Curve B represents the delocalized bound hydrogen result. There exists a systematic error in the data points indicated in the lower right corner due to uncertainty in determining the zero of the graph by fitting at high temperature.

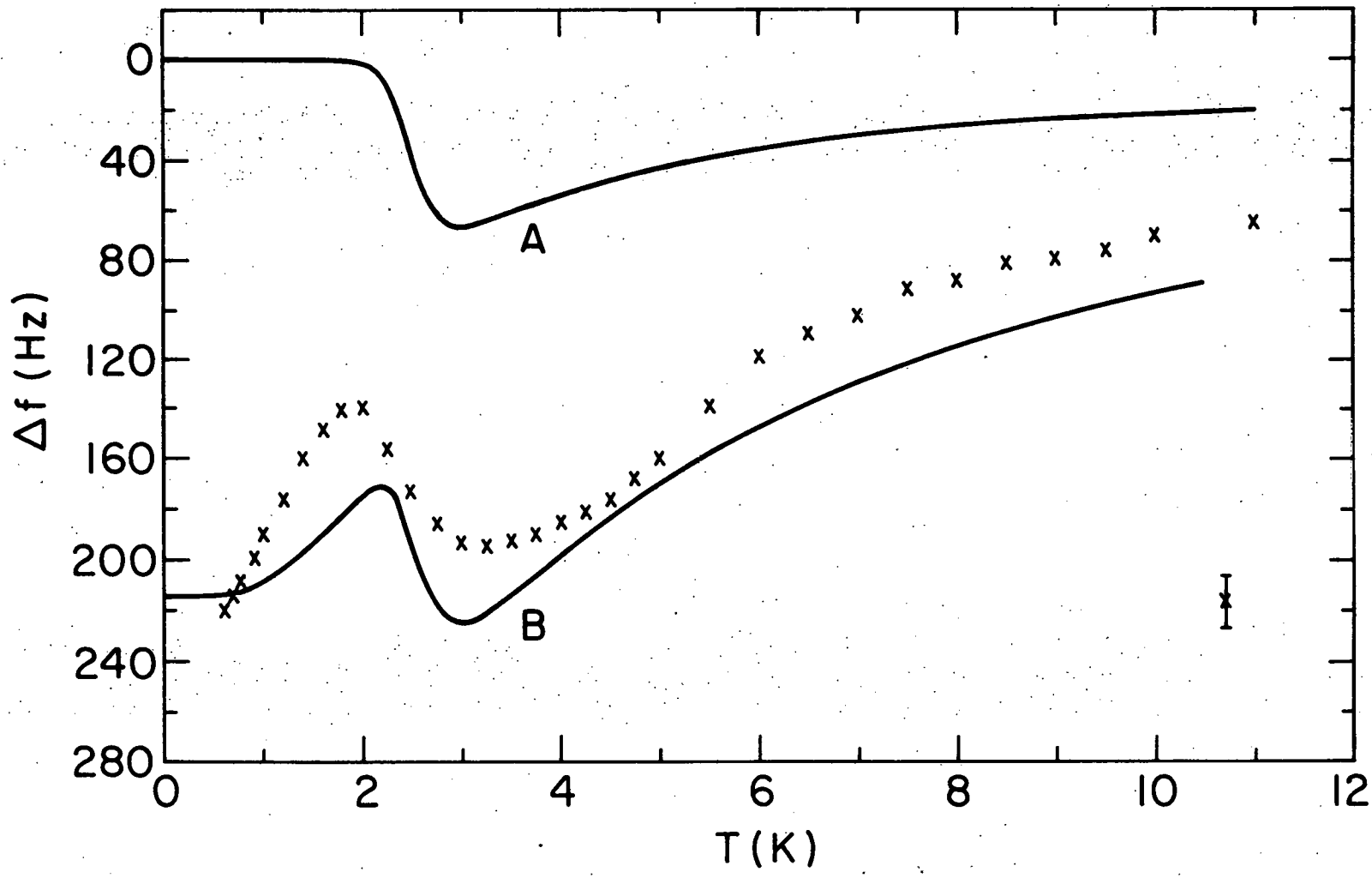
0
40
80
120
160
200
240
280
Δf (Hz)
A
B
0
2
4
6
8
10
12
T(K)

part of the curve follows a 1/T temperature dependence. The error in determining the origin of the curve is shown at the lower right of Figure 36. This error is approximately ± 15 Hz, which is larger than the relative error of the measurements, about 5 Hz.

The curve follows the data quite well at high temperatures, in view of the systematic error and the uncertainty in the concentration. At the dispersion, 2.5 K, the curve falls below the data and then increases too sharply before dropping again. The inclusion of the strain broadening will correct some of this, since the effect upon the dispersion will be to round off the maxima and minima in the curve, and to decrease the slope of the curve between those two points. Below the dispersion, the curve does not fall sharply enough to match the data, and approaches the vertical axis before the data. The strain broadening will also affect this, since the broadening will produce some systems which have smaller values of γ, and so will contribute to the velocity decrease to lower temperatures before becoming depopulated.

For comparison, the predictions of a classical model of the relaxation, such as the localized bound model, are shown by curve A. This curve is not adequate in describing the data, even considering the systematic error. The relaxation strength is at least a factor of 2 too small, and no provision for the decrease in velocity below 2 K has been allowed. At high temperatures, the 1/T decrease of the relaxation strength does not match the data.

This fit of the model to the velocity measurements is a very crucial test of the validity of the model. The curve does not contain any adjustable parameters, and still produces a reasonable fit to the experimental data. This test provides support for the delocalized bound model, and raises doubts about the validity of the classical model.

A similar procedure can be used to test the high concentration hydrogen results. However, this data requires the addition of a parameter which sets the origin of the vertical scale. The presence of the high temperature relaxation prevents matching the curves at low temperatures to obtain the absolute difference. Since the high temperature relaxation continues past the superconducting transition, the matching has to be done at high temperatures. However, the rapid decrease of the background frequency above the superconducting transition makes it difficult to subtract the curves accurately. Since the zero of the scale could not be obtained absolutely, the fit was made by moving the theoretical curve up and down with respect to the data until the best qualitative fit was made. This adjustment of the two scales represents the additional parameter which sets the origin of the experimental data. The vertical scale therefore corresponds to the theoretical fit. The data uses the same relative scale, with the origin determined as a parameter.

The decrement and velocity data were obtained from the same experiment, which eliminates any possible error due to the concentration changing between experiments. The decrement was obtained from the data of Figure 17. The corresponding velocity is shown in Figure 18 along with the prediction of the delocalized bound model, shown as the solid line.

The fit is good at temperatures below 2 K. Above 2 K, the curve falls below the data, then exceeds the data before approaching the data again at 6 K. This overshoot of the data will be greatly reduced if the effect of strain broadening is included. The broadening spreads out the dispersion in temperature. This decreases and rounds the maximum in the curve at 2 K and decreases the slope of the curve from 2 K to 3 K. Because the dispersions of the low and high temperature relaxations overlap due to the broadening,

the net effect is to cancel the undershoot at 3 K with the overshoot at 5 K, producing a curve which more closely follows the data. Above 6 K, the curve again exceeds the data points. This effect will be reduced by the broadening, which extends the relaxation up to the superconducting transition temperature, 9 K.

In these two cases it has been shown that the delocalized bound model can produce a fit to the velocity data by using the decrement data and without introducing any new parameters. The fit can be improved by considering the effects of strain broadening. The classical result does not fit the experimental data adequately.

CHAPTER 7.

SUMMARY AND CONCLUSION

Measurements were made of the velocity and attenuation of ultrasonic waves in niobium containing 1000 ppm oxygen with additional concentrations of hydrogen, to determine the properties of a relaxation of the hydrogen. Measurements were made as a function of temperature, frequency, polarization of the ultrasonic wave, hydrogen isotope, and concentration of hydrogen and oxygen.

A relaxation due to hydrogen was observed in the C' mode at 2.4 K at 10 MHz with an activation energy of 1.8 meV. The deuterium relaxation was also observed in the C' mode at 4.75 K at 3 MHz. A second relaxation was observed at higher temperatures in the C' mode due to defect pairs of both hydrogen and deuterium. No relaxations were observed in C_{44} or the bulk modulus.

Three unusual features of the relaxation are: (a) The relaxation strength due to hydrogen decreases at low temperatures below the expected 1/T result, (b) there is a decrease in the velocity below the relaxation without a corresponding effect in the attenuation, and (c) the deuterium decrement peaks are much broader in temperature than the hydrogen peaks.

The Birnbaum-Flynn model of hydrogen tunnelling is modified to take into account the trapping of hydrogen by interstitial impurities. Explicit relations between the energy eigenstates and bias strain are derived. An Orbach process is proposed for a relaxation between the degenerate first

excited states. Three parameters which are determined by the hydrogen ultrasonic attenuation data are sufficient to describe the properties of this model.

A hindered rotator calculation which uses the three parameters of this model predicts the behavior of the deuterium relaxation without introducing any new parameters. The calculation produces the wavefunctions for both hydrogen and deuterium, allowing the calculation of matrix elements which predict the isotope dependence of the relaxation. The model also correctly predicts the temperature dependence of the relaxation strength and low temperature velocity, which are not contained in a classical model of hydrogen motion over a potential energy barrier.

A reasonable fit to the velocity data for low concentration of hydrogen is made by the model with no adjustable parameters. The prediction of a classical model of hydrogen relaxation is compared, but does not produce an adequate fit. A fit to the velocity for high concentration is made by the model with one adjustable parameter. The effects of strain broadening upon the predictions are discussed.

A fit to the heat capacity results is presented. Additional parameters representing the magnitude of the bias strain effects of the oxygen trapping are used to fit the heat capacity. The fit depends upon the splitting of a low level degeneracy by the bias strain, which forces the first excited state toward the ground state, and provides for a low temperature contribution to the heat capacity.

In conclusion, a delocalized bound hydrogen wave model can account for the ultrasonic measurements using three parameters. The unusual features

of the relaxation are contained in the model without modification. These properties cannot be accounted for by a classical model of hydrogen motion by thermal activation over a potential energy barrier.

REFERENCES

B. Alefeld, K. W. Kehr, T. Springer, V. Lottner, A. Heim and N. Wakabayashi 1975, Fiz. Nizkikh Temp. 1, 638.

G. A. Alers 1966, in Physical Acoustics, edited by Warren P. Mason (Academic Press, New York, 1966), Vol. 4, Part A, p. 277.

D. P. Almond, M. J. Lea and E. R. Dobbs 1972, Phys. Rev. Lett. 29, 764.

A. C. Anderson 1972, in Temperature, Its Measurement and Control in Science and Industry (Instrument Society of America, Pittsburgh, 1972), Vol. 4, Part 2, p. 773.

A. C. Anderson, C. B. Satterthwaite and S. C. Smith 1971, Phys. Rev. B3, 3762.

C. Baker and H. K. Birnbaum 1973, Acta Metall. 21, 865.

G. Bauer and W. Schmatz 1975, Hydrogen Effects on Behavior of Materials (Proc. of Conf. at Jackson, Wyoming, Sept. 1975), A.I.M.E., New York, in press.

G. Bauer, E. Seitz, H. Horner and W. Schmatz 1975, Solid State Commun. 17, 161.

H. K. Birnbaum 1976, Scripta Metall. 10, 747.

H. K. Birnbaum and C. P. Flynn 1976, Phys. Rev. Lett. 37, 25.

H. K. Birnbaum, M. L. Grossbeck and M. Amano 1976, Journal of Less Common Metals 49, 357.

J. Buchholz, J. Völkl and G. Alefeld 1973, Phys. Rev. Lett. 30, 318.

J. R. Carlson and C. B. Satterthwaite 1970, Phys. Rev. Lett 24, 461.

H. D. Carstanjen and R. Sizmann 1972, Ber. Bunsenges. Phys. Chem. 76, 1223.

N. A. Chernoplekov, M. G. Zemlyanov, V. A. Somenkov and A. A. Chertkov 1970, Sov. Phys.-Sol. State 11, 2343.

P. Cotterill 1961, The Hydrogen Embrittlement of Metals, Progress in Materials Science, Vol. 9, No. 4, Pergamon Press, N.Y., N.Y.

K. Faber and H. Schultz 1972, Scripta Metall. 6, 1065.

B. E. F. Fender 1976 (results presented at Int. Conf. on Hydrogen in Metals, Birmingham, England, Jan. 1976).

C. P. Flynn and A. M. Stoneham 1970, Phys. Rev. B1, 3966.

E. M. Forgan and C. E. Gough 1973, J. Phys. F 3, 1596.

M. H. Frommer, J. Bostock, K. Agyeman, R. M. Rose and M. L. A. MacVicar 1973, Solid State Commun. 13, 1357.

W. Gissler, B. Jay, R. Rubin and L. A. Vinhas 1973, Phys. Lett. 43A, 279.

W. Gissler and H. Rother 1970, Physica 50, 380.

J. W. Hafstrom and M. L. A. MacVicar 1970, Phys. Rev. B2, 4511.

J. Holder 1970, Rev. Sci. Instrum. 41, 1355.

G. Kistner, R. Rubin and I. Sosnovska 1971, Phys. Rev. Lett. 27, 1576.

L. L. Lacy and A. C. Daniel 1971, Phys. Rev. Lett. 27, 1128.

W. F. Lankford, H. K. Birnbaum, A. T. Fiory, R. P. Minnich, K. G. Lynn, C. E. Stronach, L. H. Bieman, W. J. Kossler and J. Lindemuth 1978, Hyperfine Interactions 4, 833.

A. Magerl, N. Stump, H. Wipf and G. Alefeld 1977, J. Phys. Chem. Solids 38, 683.

R. F. Mattas and H. K. Birnbaum 1975, Acta Metall. 23, 973.

G. Matusiewicz and H. K. Birnbaum 1977, J. Phys. F 7, 2285.

C. Morkel, H. Wipf and K. Neumaier 1978, Phys. Rev. Lett. 40, 947.

A. S. Nowick and B. S. Berry 1972, Anelastic Relaxation in Crystalline Solids (Academic Press, New York, 1972).

A. S. Nowick and W. R. Heller 1963, Adv. Phys. 12, 251.

A. S. Nowick and W. R. Heller 1965, Adv. Phys. 14, 101.

T. Ochs 1968, J. Phys. E 1, 1122.

S. G. O'Hara, G. J. Sellers and A. C. Anderson 1974, Phys. Rev. B10, 2777.

R. Orbach 1961, Proc. R. Soc. A 264, 458.

S. S. Pan, M. L. Yeater and W. E. Moore 1969, Proc. Symp. Molecular Dynamics and Structure of Solids, p. 315, Washington, MBS 301.

V. F. Petrunin, V. A. Somenkov, S. Sh. Shil'shteyn, A. A. Chertkov and A. S. Borovik 1970, Phys. Metals Metallogr. 29, 83.

G. Pfeiffer and H. Wipf 1976, J. Phys. F 6, 167.

G. Schaumann, J. Volkl and G. Alefeld 1970, Phys. Status Sol. 42, 401.

T. Schober, M. A. Pick and H. Wenzl 1973, Phys. Status Sol. A 18, 175.

F. Seitz 1940, The Modern Theory of Solids (McGraw-Hill Book Company, New York, 1940), p. 470.

G. J. Sellers 1975, Ph.D. Thesis, University of Illinois, unpublished.

G. J. Sellers, A. C. Anderson, and H. K. Birnbaum 1973, Phys. Lett. 44A, 173.

G. J. Sellers, A. C. Anderson, and H. K. Birnbaum 1974, Phys. Rev. B10, 2771.

L. Y. L. Shen, N. M. Senozan and N. E. Phillips 1965, Phys. Rev. Lett. 14, 1025.

N. A. Skakun, P. P. Matyash, N. P. Dikii and P. A. Svetashov 1975, Zh. Tekh. Fiz. [Sov. Phys.-Tech. Phys.] 20, 432.

V. A. Somenkov, A. V. Gurskaya, M. G. Zemlyanov, M. E. Kost, N. A. Chernoplekov and A. A. Chertkov 1968, Sov. Phys.-Solid State 10, 1076.

A. M. Stoneham 1975, Collective Phenomena 2, 9.

N. Stump, W. Gissler and R. Rubin 1972, Phys. Status Sol. B 54, 295.

H. Suhl, B. T. Matthias and L. R. Walker 1959, Phys. Rev. Lett. 3, 552.

C. C. Sung and L. Y. L. Shen 1965, Phys. Lett. 19, 101.

J. A. Sussmann 1964, Phys. Kondens. Mater. 2, 146.

J. A. Sussmann and Y. Weissman 1972, Phys. Status Solidi B 53, 419.

R. Truell, C. Elbaum and B. Chick 1969, in Ultrasonic Methods in Solid State Physics (Academic Press, New York, 1969), p. 58.

B. J. C. van der Hoeven, Jr., and P. H. Keesom 1964, Phys. Rev. 134, A1320.

N. Wakabayashi, B. Alefeld, K. W. Kehr and T. Springer 1974, Solid State Commun. 15, 503.

D. G. Westlake and S. T. Ockers 1975, Met. Trans. 6A, 399, edited by K. D. Timmerhaus, W. J. O'Sullivan and E. F. Hammel (Plenum Press, New York, 1974), Vol. 3, p. 372.

J. L. Whitton, J. B. Mitchell, T. Schober and H. Wenzl 1975, Scripta Metall. 9, 851.

APPENDIX

The matrix elements which couple the eigenstates due to strain interactions can be calculated from the wavefunctions derived by the hindered rotator calculation. These wavefunctions have the form:

$$\Psi_N = \sum_{m=-\infty}^{\infty} A_m^N \exp(im\phi) \quad .$$

The strain interaction terms V have the forms:

$$V_{\varepsilon'} = \alpha' \cos 2\phi \quad , \qquad V_{\varepsilon_{44}} = \alpha_{44} \sin 2\phi$$

which can be rewritten as

$$V_{\varepsilon'} = \frac{\alpha'}{2}\left(e^{i2\phi} + e^{-i2\phi}\right) \quad , \quad V_{\varepsilon_{44}} = \frac{\alpha_{44}}{2i}\left(e^{i2\phi} - e^{-i2\phi}\right) \quad .$$

The matrix elements are then calculated as

$$\langle I|V_{\varepsilon'}|J\rangle = \frac{\alpha'}{2} \sum_{n=-\infty}^{\infty} A_n^J\left(A_{n+2}^I + A_{n-2}^I\right)$$

$$\langle I|V_{\varepsilon_{44}}|J\rangle = \frac{\alpha_{44}}{2i} \sum_{n=-\infty}^{\infty} A_n^J\left(A_{n+2}^I - A_{n-2}^I\right) \quad .$$

These sums are indicated by the elements in the following two matrices. Where the matrix elements are non-zero, the upper element represents the result for hydrogen, while the lower element is the deuterium result. The matrix

elements can be obtained by multiplying these entries by $\alpha'/2$ for the C' results, and $\alpha_{44}/2$ for the C_{44} results.

C'

	1	2	3	4	5	6	7	8
1	0	0	0	1.55 1.96	0	0	0	0
2		0	1.32 1.96	0	0	0.46 0.06	0.46 0.06	0
3			0	0	0	0.46 0.06	0.46 0.06	0
4				0	0	0	0	1.19 0.17
5					0	0	0	0
6						0	0.64 0.01	0
7							0	0
8								0

C_{44}

	1	2	3	4	5	6	7	8
1	0	0	0	0	1.20 0.17	0	0	0
2		0	0.64 0.01	0	0	0.46 0.06	0.46 0.06	0
3			0	0	0	0.46 0.06	0.46 0.06	0
4				0	0	0	0	0
5					0	0	0	1.54 1.96
6						0	1.31 1.96	0
7							0	0
8								0

VITA

David Brian Poker was born on [redacted].

He received his secondary education at Oswego Community High School, Oswego, Illinois. He received a Bachelor of Science in Physics in June 1973 and a Master of Science in Physics in June 1974 from the University of Illinois, Urbana, Illinois. He is a member of Phi Beta Kappa and the American Physical Society, and received University Fellowships in 1973 and 1975. He is married to Leslie Bogda Poker and has a son.